The effect of scaffolds with a negative, zero, or positive Poisson's ratio on pre-osteoblastic (MC3T3-E1) cell response

Denise Peeters
November 2020

TUDelft

The effect of scaffolds with a negative, zero, or positive Poisson's ratio on pre-osteoblastic (MC3T3-E1) cell response

By

D. Peeters
4701461

In partial fulfillment of the requirements for the degree of

Master of Science
In Biomedical Engineering

at the Delft University of Technology,
to be defended publicly on 30 November at 10:00.

Daily Supervisors:	H.M.A. Kolken MSc.
	M. Nouri Goushki MSc.
	Ing. M. Minneboo
Thesis committee:	Dr.Ir. E.L. Fratila-Apachitei
	Dr. M. Mirzaali Mazandarani
	Prof. Dr. Ir. A.A. Zadpoor
External committee member:	Dr. A.C. Akyildiz

Mechanical, Maritime, and Materials Engineering (3ME)
Biomedical Engineering
Musculoskeletal Biomechanics

November 2020

Abstract

Bone tissue engineering (BTE) researches the characteristics which are needed to create the ultimate bone scaffold which enhances cell response. Limited research has been done regarding the effect of the Poisson's ratio on the scaffold-cell interaction. In this graduation project we therefore explore the cell response on scaffolds with a different value of the Poisson's ratio. Various meta-biomaterials were designed, manufactured, mechanically tested and the response on pre-osteoblasts (MC3T3-E1) was explored. The first experiment was performed at mesoscale. The meta-biomaterials, with cells, were evaluated with SEM imaging, presto blue and ARS staining. The second experiment was performed at micro-scale. The results of this experiment were evaluated with SEM imaging, actin staining and Runx2 staining. It was concluded that the auxetic meta-biomaterial, with negative Poisson's ratio, high porosity and high stiffness, showed an enhancement of the cell response. However, this could not be confirmed by the 2D SEM images. A potential application for the meta-biomaterial that enhances the cell response is implementing this meta-biomaterial in a design for the surface of an implant to generate fast bone ingrowth.

Table of contents

1. Introduction

Every year, over two million bone grafting procedures are performed worldwide[1]. These bone grafts help to heal defects that exceed 2 to 2.5 times the diameter of the affecting bone (i.e. large bone defects)[2]. Small bone defects can heal by itself as human bone is continuously remodeling and developing. Osteoclasts resorb old and damaged bone, followed by the osteoblasts which produce new bone[3]. The bone remodeling cycles are similar, for both trabecular and cortical bone, but cortical bone remodeling proceeds in tunnels and trabecular bone remodeling proceeds at the surface (figure 1)[4, 5]. Besides healing small damages, bone is also adjusting its architecture to the mechanical forces it is subjected to[6]. If large bone defects are left untreated, they will only self-heal for 10 percent[7]. Therefore, a bone scaffold can contribute to completely restore both structure and function of the affected bones[8, 9].
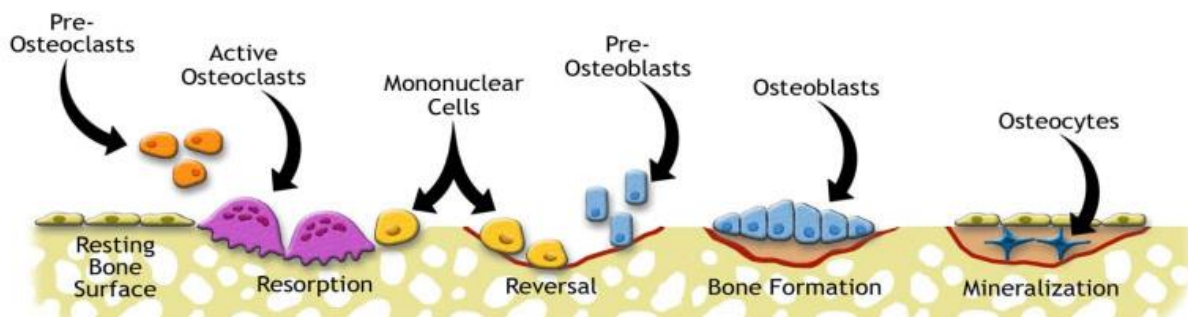
Figure 1. Trabecular bone remodeling cycle. Pre-osteoclasts become osteoclasts and resorb bone. The mononuclear cells prepare the surface for the osteoblasts. Then pre-osteoblasts become osteoblast and will produce bone. These osteoblasts become osteocytes and will mineralize to finish the bone formation[3].

Within the field of Bone Tissue Engineering (BTE), research is being done to find the ultimate bone scaffold that can be used to heal large bone defects. During the last few years, BTE has gained much attention[10]. BTE focuses on the use of scaffold biomaterials that interact with bone cells and growth factors. The aim is to engage an appropriate cellular response which is allowing skeletal regeneration to heal a large bone defect. A bone scaffold that mimics trabecular properties will easily blend into the surrounding trabecular bone and will therefore form a good basis for a bone scaffold[5].

Bone scaffolds can be built out of mechanical meta-biomaterials. Biomaterials include materials which are able to interact with elements of a living system[11]. Mechanical meta-biomaterials are biomaterials in which the small-scale architecture determines their macro-scale mechanical properties[12, 13]. These meta-biomaterials can be divided into two categories regarding their Poisson's ratio; conventional and auxetic meta-biomaterials. Conventional (i.e., non-auxetic) meta-biomaterials have a positive Poisson's ratio and react to axial compression with a lateral expansion. Auxetic meta-biomaterials have a negative Poisson's ratio and exhibit a lateral contraction in response to axial compression[14]. These mechanical meta-biomaterials can also be combined forming a hybrid meta-biomaterial[15].

The mechanical meta-biomaterial should mimic trabecular bone that has a complex structure and is reported to have some auxetic behavior[16]. The research on auxetic scaffold cell interaction is limited. So far, Choi et al. (2016) looked into the cell proliferation of MG-63 osteoblast-like cells on auxetic materials under compression[17]. It showed that the auxetic designs had significant beneficial differences in cell proliferation after 1 and 3 days of cell culturing, but after 5 days, the differences were no longer significant. Another study that researched the scaffold cell interaction of auxetic materials is from Zhang et al. (2013)[18]. This research explored the cellular proliferation of 10T1/2 cells on auxetic materials by producing a time-lapse. The scaffolds were solely exposed to the forces applied by the differentiating cells. The results of this study showed an unusual cell division, which could lead to genetic instability. Both studies showed inconclusive results and more research is needed in this

area of interest. In this graduation project, we will address this gap in the literature and research the behavior of bone cells on bone scaffolds with different values of Poisson's ratio. Scaffolds with a positive Poisson's ratio will be built out of a conventional meta-biomaterial, whereas negative Poisson's ratio scaffolds will be built of an auxetic meta-biomaterial. We also decided to combine the two to create a hybrid scaffold.

In this graduation project, we will design, manufacture and mechanically test several bone scaffolds, with different values of Poisson's ratio. Next, we will seed them with bone cells to acquire insight into their ability to regenerate bone. With different kinds of staining procedures and imaging techniques, the cell response will be evaluated.

The research of the cellular behavior of pre-osteoblasts (MC3T3-E1) on the different bone scaffolds is based on two experiments. The first experiment is performed with meta-biomaterials created according to the morphological and mechanical properties of trabecular bone at mesoscale (i.e. bone-mimicking scaffolds). We used conventional, auxetic and hybrid unit cells with different Poisson's ratio, but identical porosity. The mechanical properties of the meta-biomaterials were retrieved using a mechanical compression test and a finite element model. The second experiment is executed with micro-scale meta-biomaterials, that are ten times smaller than the meta-biomaterials of the first experiment (i.e. micro-scale scaffolds). Due to their small size, the bone cells will almost be identical in size. Therefore, this experiment explores whether the pre-osteoblasts are able to recognize the meta-biomaterial to which they are exposed, and more specifically its Poisson's ratio. On top of the aforementioned meta-biomaterials, a conventional and auxetic scaffold were added with a similar stiffness as the hybrid meta-biomaterial. As a control group, an additional meta-biomaterial was built with cuboid unit cells that have a zero Poisson's ratio.

The aim of this graduation project is to expand the knowledge regarding scaffold cell interaction, on scaffolds with a negative, zero or positive Poisson's ratio. This will hopefully lead to a new focal point to further improve BTE. This report will also show whether a specific Poisson's ratio can enhance the MC3T3-E1 pre-osteoblastic cell response.

2. Methods & Materials

To be able to research the scaffold cell interaction, different meta-biomaterials that act as scaffolds had to be designed. The first part of the section 'methods and materials' explores the designs of the different meta-biomaterials. Next, the fabrication of the meta-biomaterials and their morphological and mechanical characterization are described. The final part involves the biological characterization of the meta-biomaterials with the MC3T3-E1 pre-osteoblastic cells and the statistical analysis.

2.1 Design of the meta-biomaterials

The designs of the bone-mimicking scaffolds used in this research will be based on the morphological and mechanical properties of trabecular bone. Morphological properties give insight into the design of the structure and the mechanical properties include stiffness and strength of trabecular bone. Even though they describe different things, morphological and mechanical properties are highly dependent on each other.

Important morphological properties are porosity, pore size and trabecular spacing. The porosity describes the void space of a structure as a percentage of the total volume. Bone with a porosity between 50% and 90% is considered to be trabecular bone[19]. The void spaces in trabecular bone allow vascularization and bone ingrowth[20]. Osteoblasts generate new bone and need a trabecular-like porosity and a pore size of at least 300 μm to survive[19, 21]. New bone is created according to Wolff's law, this law states that bone will remodel in response to external loading, which differs according to the anatomical location[22]. At places where small mechanical forces are absorbed, bone will create an open rod-like structure which has a low density, and at places where high mechanical forces are absorbed, bone will create a closed plate-like structure which has a high density (figure 2)[23]. The void spaces that are created by these remodeling cycles can be characterized by the trabecular spacing. This trabecular spacing was explored by several imaging techniques; magnetic resonance imaging (MRI), micro-computed tomography (micro-CT) and ultrasound[5, 24-26]. The study of Rabiatul et al. (2014)[27] reviewed these results and showed that the trabecular spacing varies between 360 μm and 1470 μm[28].
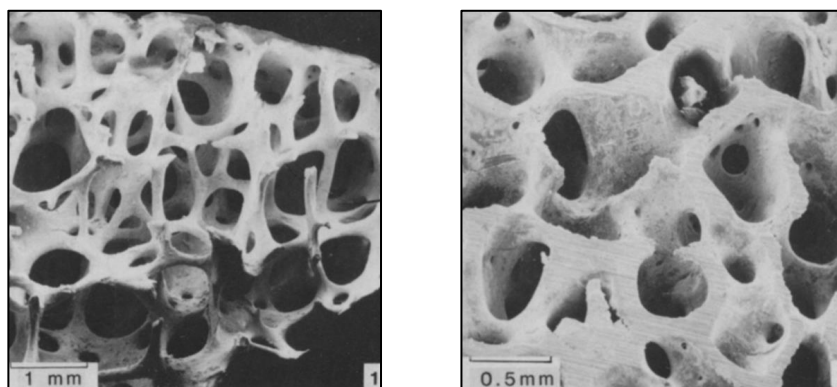
Figure 2. Morphology of trabecular bone from femoral head taken by a scanning electron microscope (SEM). 1) Asymmetric open rod-like, low density structure. 2) Asymmetric closed plate-like, high density structure[23].

The mechanical properties include stiffness and strength of trabecular bone, but also the Poisson's ratio. An important mechanical parameter is bone mineral density (BMD). The BMD is positively correlated with the stiffness and strength of bone[29]. Trabecular bone has a BMD that varies between 140 kg/m^3 and 200 kg/m^3, with an average of 185 kg/m^3. This variety is caused by the different forces that are acting on the bone according to its anatomical location. As BMD is related to the stiffness of the bone, the stiffness also depends on the anatomical location. The stiffness shows to what extent

the structure resists deformation in the direction of the acting load and is dependent on its geometry and the Young's modulus of the bulk material. The stiffness of trabecular bone varies between 0.2 GPa and 14.8 GPa[30-32]. According to Boal et al. (1993) 'the Poisson's ratio is a measure of the strain in a transverse direction which results from a stress applied longitudinally'[33]. The average Poisson's ratio, despite some auxetic behavior, was assumed by Ulrich et al. (1999), Kowalczyk et al. (2003), Müller et al. (1995), Pothuaud et al. (2002) and Rho et al. (1997) to be ± 0.3[5, 34-37]. This value can have a standard deviation of 0.1, as it only results in an 8% change of the Young's modulus[37].

The morphological and mechanical parameters describe the properties of trabecular bone. The designs of the bone-mimicking scaffolds that are used in this research will, within defined ranges of the parameters (table 1), mimic the trabecular behavior. Except, for the Poisson's ratio, which should vary from negative over zero to positive according to our research set up.

Table 1. Morphological and mechanical parameters of trabecular bone.

Porosity	Pore size	Trabecular spacing	Density	Young's modulus	Poisson's ratio
50 – 90%	>300 µm	360 - 1470 µm	140 - 200 kg/m^3	0.2 – 14.8 GPa	0.3 ± 0.1

2.1.1 Bone-mimicking scaffolds

The designs of the bone-mimicking scaffolds were made from conventional, auxetic and hybrid unit cells that were patterned to create a specimen with the characteristics of a meta-biomaterial. The dimensions of the designs for the first experiment were based on the morphological and mechanical properties of trabecular bone. Mandal et al. (2009) showed that a higher porosity leads to higher cell proliferation[38]. To exclude this parameter from influencing the results, it was chosen to design each specimen with the same porosity (meta-p-biomaterial).

2.1.1.1 Conventional meta-biomaterial

Conventional meta-biomaterials generally have a positive Poisson's ratio[14]. A honeycomb structure is present in many natural materials and contributes to a light and stiff structure and was therefore used for the design[39, 40]. A cross-section of a conventional honeycomb structure is shown in figure 3. The geometrical dimensions and the mechanical properties of the honeycomb structure are dependent on the angle θ and the cell rib length ratio h/l[41]. Jiang et al. (2019) showed that the bigger the angle θ, the higher the critical strain[42]. Therefore, 45^0, the biggest angle that was used in this study, gave the best results and was used in the design. The studies of Gibson et al. (1982), Kolken et al. (2017) and Jiang et al. (2019) showed that the bigger the cell rib length ratio h/l, the higher the critical strain[39, 41, 42]. To get the exact dimensions of the cell ribs, we looked at the morphological properties of trabecular bone. It was mentioned that osteoblasts need a pore size of at least 300 µm to survive[19, 43].
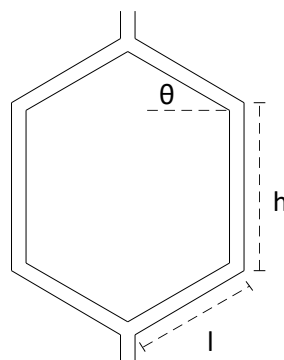
Figure 3. Cross-section view of a honeycomb structure.

In the end, all specimens used in this experiment should have the same dimensions. This means that every design was based on a unit cell with the same width and height values. Using these geometrical parameters, h and l were determined and the specimen was built in SolidWorks (Dassault Systèmes, Vélizy-Villacoublay, France). The strut thickness of the unit cell was calculated to retrieve a porosity of 75%, resulting in a strut thickness (t) of 65.1 µm (equations 1-4; absolute density = 290 $^{kg}/_{m^3}$). The exact dimensions of the unit cell can be found in figure 4A and table 2. The conventional bone-mimicking scaffold (C_p) was made of a 6x6x3 cell array (figure 4B).

$$Volume\ solid\ specimen\quad = length * width * heigth \quad\quad [1]$$

$$Volume\ unit\ cell\quad = \pi \left(\frac{t}{2}\right)^2 * (3h + 8l) \quad\quad [2]$$

$$Volume\ specimen\quad = Volume\ unit\ cell * 6 * 6 * 3 \quad\quad [3]$$

$$Porosity\quad = 100\% - \frac{Volume\ solid\ specimen}{Volume\ specimen} \quad\quad [4]$$
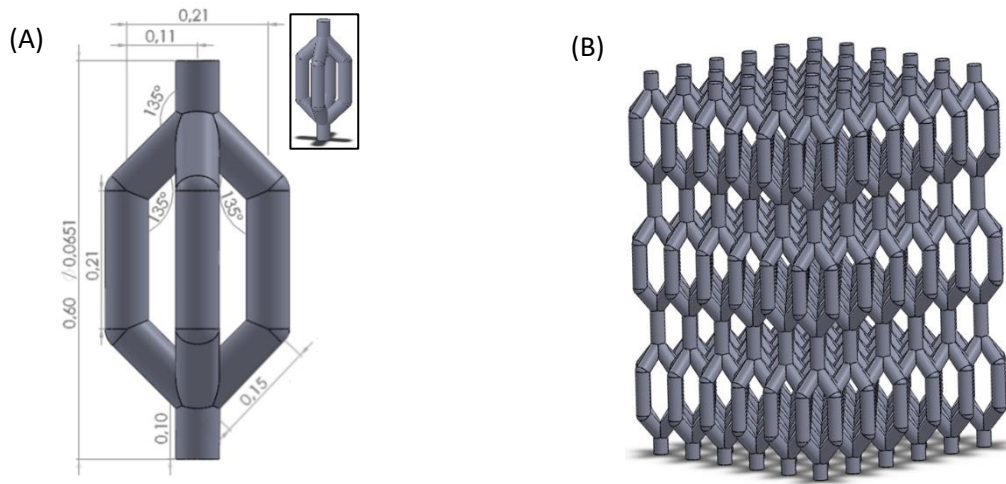
Figure 4. (A) Design of the conventional unit cell with its dimensions in mm. (B) Design of C_p, which is made of a 6x6x3 cell array. C_p measures 1.272x1.272x1.8 mm.

2.1.1.2 Auxetic meta-biomaterial

Auxetic meta-biomaterials have a negative Poisson's ratio, and a well-known auxetic unit cell is the re-entrant hexagonal honeycomb[14]. Typical for a re-entrant hexagonal honeycomb structure is that the ribs are directed inwards (figure 5)[41, 44, 45]. Its mechanical properties are dependent on the angle θ and the cell rib length ratio h/l.
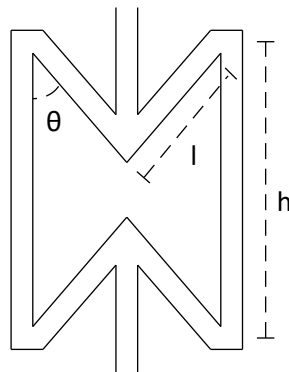
Figure 5. Cross-section view of re-entrant hexagonal honeycomb unit cell.

With the parameters h, l and θ (table 2), the specimen was built in SolidWorks. The required porosity of 75% led to a strut thickness of 42.37 μm which can be found in figure 6A including all dimensions of the unit cell. The auxetic bone-mimicking scaffold (A_p) was made from a 6x6x3 cell array and is shown in figure 6B.
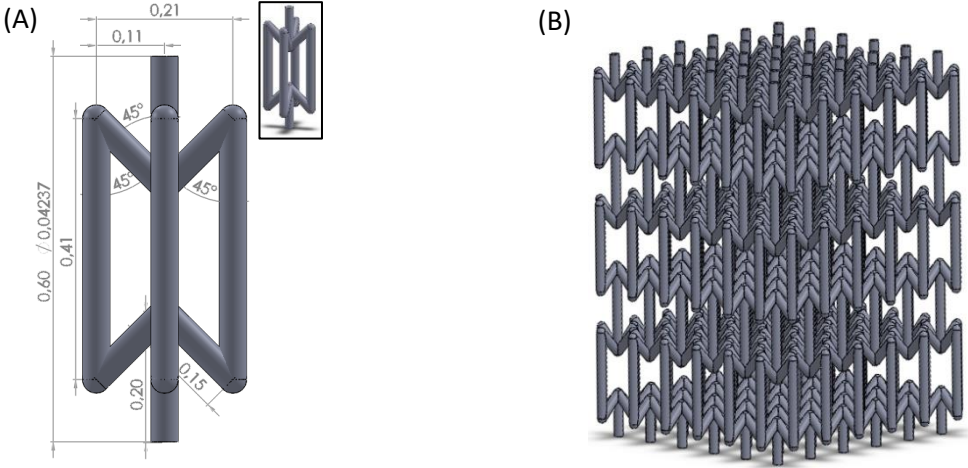
Figure 6. (A) Design of the auxetic unit cell with its dimensions in mm. (B) Design of A_p, which is made of a 6x6x3 cell array. This A_p measures 1.272x1.272x1.8 mm.

2.1.1.3 Hybrid meta-biomaterial

The hybrid meta-biomaterial is a combination of the aforementioned conventional and auxetic unit cells. The cross-sectional view of this combination is shown in figure 7 and was also dependent on the angle θ and the cell rib length ratio h/l.

With the parameters h, l and θ (table 2), the unit cell and specimen were built in SolidWorks. With a strut thickness of 43.67 μm, a porosity of 75% could be achieved and is shown in figure 8A. The hybrid bone-miming scaffold (H_p) was made of 6x3x3 array and can be found in figure 8B.
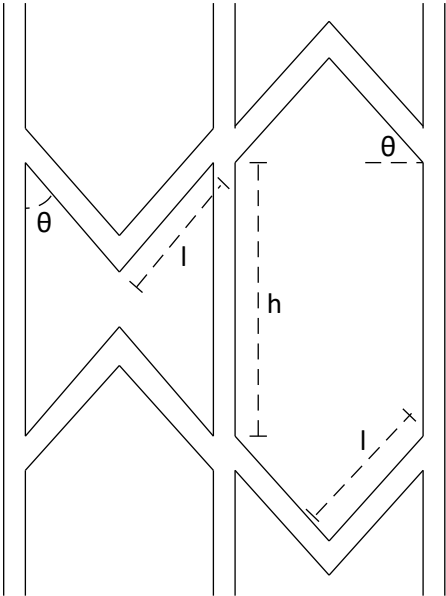
Figure 7. Cross-section view from the hybrid unit cell.
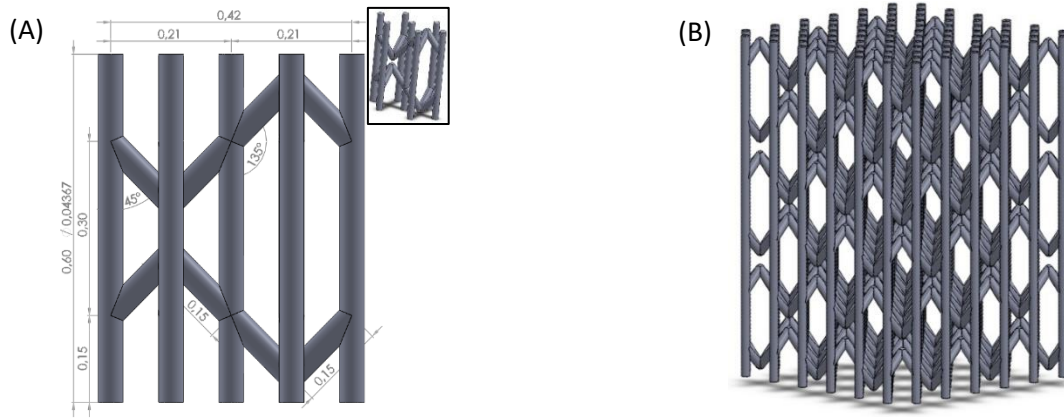
Figure 8. (A) Design of the hybrid unit cell with its dimensions in mm. (B) Design of H_p, which is made of a 6x3x3 cell array. This H_p measures 1.272x1.272x1.8 mm.

Table 2 gives an overview of all dimensions of the abovementioned unit cells.

Table 2. Dimensions of the conventional, auxetic and hybrid unit cells.

Unit cell	Conventional	Auxetic	Hybrid
Total height (μm)	600	600	600
Porosity (%)	75	75	75
Absolute density ($^{kg}/_{m^3}$)	290	290	290
θ (^{0})	45	45	45
h/l	1.4	2.7	2
h (μm)	210	410	300
l (μm)	150	150	150
Strut thickness (μm)	65.1	42.37	43.67

2.1.2 Micro-scale scaffolds

A second experiment is included to explore whether the MC3T3-E1 pre-osteoblastic cells are able to recognize the specimen to which they are exposed. This experiment included six different specimens at micro-scale. The dimensions of all specimens were identical (127.2x127.2x180 μm), being ten times smaller than the specimens used in the previous experiment. The specimens were again designed in SolidWorks and manufactured at micro-scale, consequently, these micro-scale scaffolds have almost the same size as the MC3T3-E1 pre-osteoblastic cells[8].

Three of the designs were similar to the designs used in the first experiment but smaller. The mechanical properties of the aforementioned hybrid unit cell formed the basis for the following designs. A conventional and an auxetic unit cell were created, making sure their specimens will eventually mimic the stiffness of the hybrid meta-biomaterial (meta-s-biomaterial). Their stiffness was calculated in a finite element (FE) model, and their strut thickness was determined. The unit cells, shown in figure 9, were again repeated to form a 6x6x3 cell array. The porosity of the specimens were defined as the ratio of the volume of each specimen to the theoretical volume of a corresponding solid specimen (equations 1-4) and resulted in 78.1% porosity for the conventional meta-s-biomaterial (C_s) and 64.1% porosity for the auxetic meta-s-biomaterial (A_s).
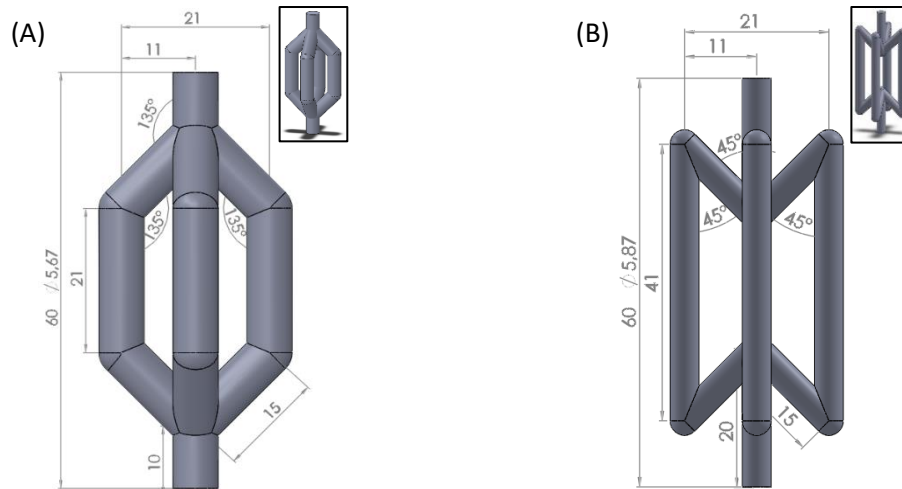
Figure 9. (A) Design of the conventional unit cell with a strut thickness of 5.67 µm. (B) Design of the auxetic unit cell with a strut thickness of 5.87 µm. The dimensions in the figure are in µm.

The final design has a zero Poisson's ratio and will function as a control group. This control group was required since it may be difficult for osteoblasts to attach to the small specimens and we want to know whether this is due to the Poisson's ratio. To obtain a zero Poisson's ratio, this specimen was made of cuboid unit cells (figure 10) and repeated to form a 6x6x3 cell array. The porosity was calculated with equations 1-4 and resulted in 89% porosity for the cuboid meta-s-biomaterial (CB_s).
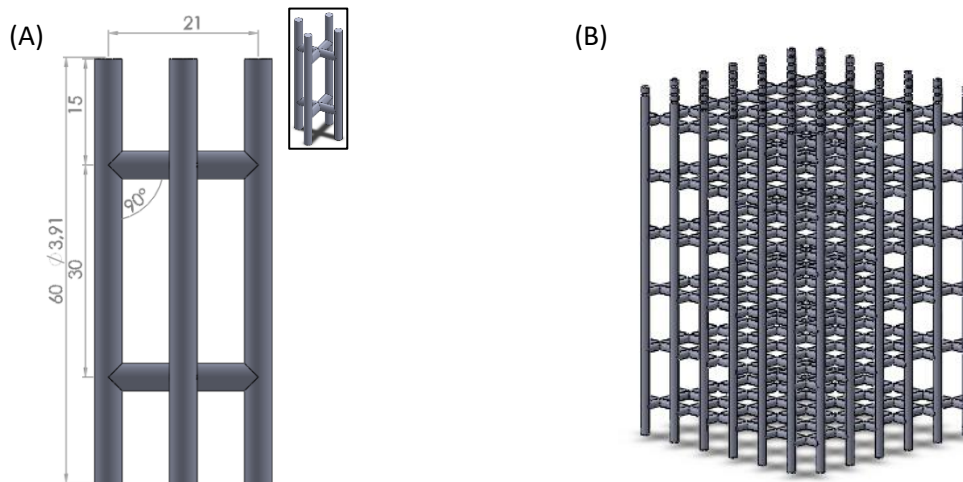
Figure 10. (A) Design of the cuboid unit cell with a strut thickness of 3.91 µm. The dimensions in this figure are in µm. (B) Design of CB_s, which is made of a 6x6x3 cell array. This CB_s measures 127.2x127.2x180 µm.

The micro-scale scaffolds are divided into two categories. The first category contains specimens with the same porosity (micro-p-scale scaffold) and will include the downscaled specimens from the first experiment: C_p, A_p and H_p. The second category contains specimens with the same stiffness (micro-s-scale scaffolds) and will include: C_s, A_s, H_s and CB_s, where H_s is the same specimen as H_p but is compared solely to micro-s-scale scaffolds. An overview of all the dimensions of the abovementioned unit cells of the micro-scale scaffolds is shown in table 3.

Table 3. Dimensions of the micro-scale unit cells.

Unit cell	Micro-p-scale			Micro-s-scale		
	Conventional	Auxetic	Hybrid	Conventional	Auxetic	Cuboid
Total height (μm)	60	60	60	60	60	60
Porosity (%)	75.0	75.0	75.0	78.1	64.1	89.0
Absolute density ($^{kg}/_{m^3}$)	290	290	290	260	420	200
θ (⁰)	45	45	45	45	45	0
h/l	1.4	2.7	2.0	1.4	2.7	2.9
h (μm)	21	41	30	21	41	30
l (μm)	15	15	15	15	15	10.5
Strut thickness (μm)	6.51	4.24	4.37	5.67	5.87	3.91

2.2 Fabrication

All designs of the specimens were fabricated with an additive manufacturing (AM) technique called direct laser writing. Due to the small-scale designs of the specimens, the Photonic Professional GT machine (Nanoscribe, Germany) was used. It uses a two-photon polymerization (2PP) technique where two photons are absorbed by a photosensitive material (photoresist), which leads to photopolymerization. The photopolymerization starts at the substrate where the bottom of the specimen is formed. Once a single layer is completed, the microscopic Z-drive for the mesoscale structures, and the piezo stage for the micro-scale structures, lowers while the photopolymerization still occurs at its original Z-position. This continues until the specimen is formed[46].

Each CAD design was imported into the printing preparation software Describe (Nanoscribe, Germany), in which the print job could be prepared by slicing (bone-mimicking scaffold: 2; micro-scale scaffold: 1) and hatching (both: 0.5) the specimen. The resulting job file was imported in the Photonic Professional GT machine (Nanoscribe, Germany) and the machine and material were prepared.

The microscope objective 25x (numerical aperture [NA] = 0.8) is recommended for mesoscale structures. This microscope objective requires a droplet of photoresist (IP-S, Nanoscribe, Germany) and an ITO-coated glass substrate (Nanoscribe, Germany) in a DiLL writing mode to print (figure 11)[47, 48]. The micro-scale scaffolds were also built using this combination to enable the comparison of the results (table 4). Next, the specimen has to be developed by immersing the specimen in propylene glycol monomethyl ether acetate (PGMEA, Sigma-Aldrich, Germany) for 25 minutes, followed by 5 minutes of rinsing with isopropyl alcohol (IPA, Sigma-Aldrich, Germany) in an air safety cabinet[49].
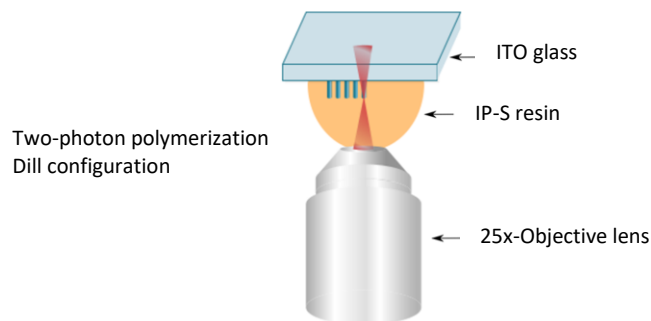
Figure 11. Two-photon polymerization process with ITO glass, IP-S resin and 25x-objective lens in DiLL configuration of the Photonic Professional GT machine (Nanoscribe, Germany)[50].

Table 4. Printer settings used to fabricate the specimens of both experiments.

	Bone-mimicking scaffolds	Micro-scale scaffolds
Scan speed ($^{\mu m}/_s$)	50000	50000
Laser power (%)	50	70
Interface position (μm)	1	1

2.3 Morphological characterization

The morphological parameters of the manufactured specimens were characterized using the VHX-6000 microscope (Keyence, Osaka, Japan). The strut thickness of each specimen was measured at ten different places and the mean was taken. With equations 1-4, described in the part 'design', the mean manufactured porosity of all specimens was calculated.

2.4 Mechanical characterization

The mechanical properties of the specimens are dependent on their small-scale architecture and the bulk material [46, 51]. The material properties were retrieved with a mechanical compression test. The results of this mechanical compression test were used in a FE model to obtain the proper bulk material properties. Thereafter, these material properties were used to calculate the mechanical parameters for all specimens used in this study.

2.4.1 Mechanical testing

The mechanical compression test was performed with four hybrid bone-mimicking scaffolds based on ISO 13314:2011[52, 53]. Each specimen was placed between the compression plates of the mechanical compression testing machine LLOYD LR5K (Lloyd Instruments, United Kingdom) (figure 12). Comparable to test parameters used in the studies of Linde et al. (1991) and Keaveny et al. (1994) (constant deformation rate of 0.05 mm/s for a 5x5x5 mm specimen; constant deformation rate of 0.04 mm/s for a specimen with a diameter of 6 mm and a length of 8 mm, respectively) the mechanical compression test was performed with a constant deformation rate of 0.025 mm/s for a 1.272x1.272x1.8 mm specimen until ± 40% strain was reached[54, 55]. The samples were tested with a 5N load cell, and the displacement and force were registered.
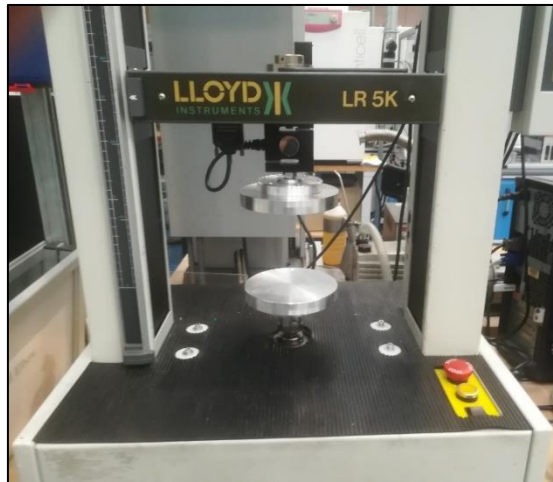
Figure 12. The LLOYD LR5K testing machine. The specimen was placed between the compression plates. The top plate compressed the specimen until a 40% strain was measured.

With the results of the mechanical compression test, a stress-strain curve could be made. This curve showed when the first layer of the structure failed and a peak force was reached. The strain (ε) was calculated using the displacement and the initial height of the specimen (equation 5), the stress (σ)

was calculated using the force and the area on which this force was applied (equation 6), and the Young's modulus (i.e. stiffness; E) of the meta-biomaterial could then be calculated using the slope of the linear region of the stress-strain curve (equation 7)[56]. The stiffness of the specimen was used to calculate the bulk material properties in a finite element (FE) model.

$$\varepsilon = \frac{Compression\ (mm)}{Initial\ height\ (mm)} \qquad [5]$$

$$\sigma\ (MPa) = \frac{Maximal\ force\ (N)}{Area\ structure\ (mm^2)} \qquad [6]$$

$$E\ (MPa) = \frac{\sigma\ (MPa)}{\varepsilon} \qquad [7]$$

2.4.2 Finite Element Modeling

To translate the results of the mechanical compression test to the material properties, a FE model was used. This FE model is a computational model, that simulates the compression test. The Young's modulus of the bulk material was adjusted until the stiffness of the specimen in the FE model mimicked the stiffness of the specimen measured in the mechanical compression tests.

The computational model was made in Abaqus (Dassault Systèmes, Vélizy-Villacoublay, France). To mimic the physical test, the geometry of the specimen was imported from SolidWorks. The specimen was assumed to behave as an isotropic elastic material with a Poisson's ratio of 0.35 and a Young's modulus yet to be determined[46]. The specimen was meshed in 411980 quadratic tetrahedral elements of type C3D10 with an approximate global size of 0.1. Due to the complexity of the specimen, a bigger mesh was not possible. Two reference points (RPs) were added, one above and one below the specimen (figure 13). The top of the specimen was connected to the top RP, and the bottom of the specimen was connected to the lower RP, both by a coupling constraint. A job with the static general step including the displacement/rotation boundary conditions of both RPs until 16.7% strain was reached (table 5) was submitted. With the resulting reaction force and the accompanying displacement, the stiffness of the specimen was calculated. By systematically changing the Young's modulus of the bulk material, and calculating the stiffness of the specimen, the actual Young's modulus of the bulk material could be determined. This could then be implemented in a FE model to determine the stiffness and Poisson's ratio for all specimens.
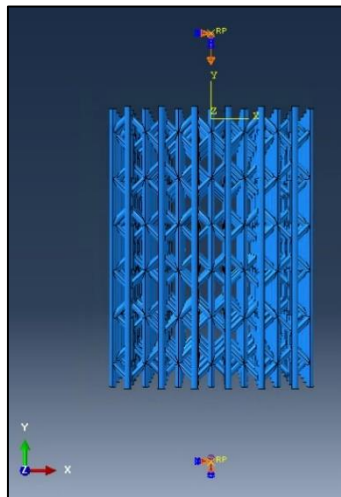
Figure 13. Overview of the FE model with H_p/H_s. The boundary conditions of the compression test are shown at the RPs.

Table 5. Displacement/rotation boundary conditions of the RPs for the compression test until 16.7% strain.

	RP top	**RP bottom**
U1	0	0
U2	-0.2	0
U3	0	0
UR1	0	0
UR2	0	0
UR3	0	0

Besides the RPs, a set of nodes was composed to measure the width of the specimen (red dots in figure 14). Before the job was submitted, the width of the specimen was identified by the distance between the red dots (initial width). Together with the width of the specimen after compression, the Poisson's ratio (v) was calculated using equations 8 and 9[57].
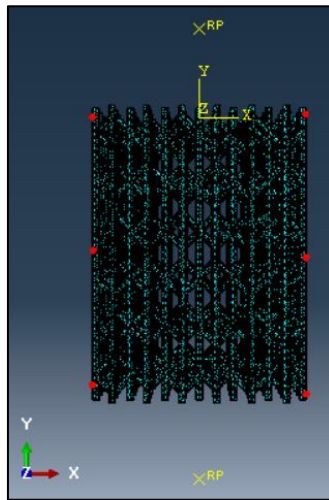
Figure 14. Overview of the FE model of H_p/H_s including the mesh. The red dots show the measurement points.

$$\varepsilon_{lateral} = \frac{(Initial\ width - Width\ after\ compression)\ (mm)}{Initial\ width\ (mm)} \quad\quad [8]$$

$$v = -\frac{\varepsilon_{lateral}}{\varepsilon} \quad\quad [9]$$

This FE model was also used to determine the lateral Poisson's ratio. The RPs and attachment of the coupling constraints were relocated to each side of the specimen, whereas the measurement points were relocated to the top and bottom of the specimen. At last, the displacement/rotation boundary condition was altered to a displacement in the x-direction. Using equations 8 and 9, by altering the width to height values, the lateral Poisson's ratio was calculated.

2.5 Biological characterization

After manufacturing the specimens and obtaining their mechanical and morphological parameters, the scaffold cell interaction and cell function can be explored by several staining and imaging techniques (table 6).

Before the start of the experiments, all specimens were sterilized with the classic autoclave machine (Prestige Medical, New York, United States) to make sure they were not contaminated[58]. The cells were cultured in a mixture of alpha minimal essential medium, 1% penicillin-streptomycin and 10% fetal bovine serum (αMEM) (Thermo Fisher)[59]. All specimens were exposed to a cell culture of pre-osteoblasts (MC3T3-E1). This cell line is used because the pre-osteoblasts differentiate to

osteoblasts after adding the growth factors ascorbic acid (1:1000) and beta-glycerol phosphate (1:500) (Sigma-Aldrich)[60]. Osteoblasts are the cells that contribute to bone formation and we are interested to see how these cells respond on specimens with negative, zero or positive Poisson's ratio.

Table 6. Overview of the performed imaging and staining techniques at each evaluation day.

Bone-mimicking scaffolds						
Day	1	3	7	11	14	21
SEM		x			x	x
Presto Blue *Metabolic activity*	x	x	x	x	x	
Alizarin Red S *Mineralization*						x
Micro-scale scaffolds						
Day		3			7	
SEM		x			x	
Actin *Cell cytoskeleton*		x			x	
Runx2 *Cell differentiation*					x	

2.4.1 Bone-mimicking scaffolds
The experiment using the bone-mimicking scaffolds included the staining and imaging techniques shown in table 6 and was performed twice, at different time points, to ensure the reliability of the results. For each experiment, six bone-mimicking scaffolds of each design were detached from their substrate, sterilized and placed into a 24-well plate. The bone-mimicking scaffolds were cultured in 500 µl αMEM with 450.000 MC3T3-E1 cells for a total of 21 days. A control group of 20.000 MC3T3-E1 cells with only αMEM was included to show how the cells respond without a specimen. The well plate was then incubated (37 °C, 5% CO_2) to imitate the temperature of the human body. Every two days, the medium was refreshed with 500 µl differentiation medium (αMEM mixed with ascorbic acid and beta-glycerol-phosphate). To evaluate the results, the cell interaction and cell function were explored.

2.4.1.1 Cell interaction
The morphology of the cells on the surface of the bone-mimicking scaffolds was imaged with the scanning electron microscope (SEM) (JSM-IT100LA, JEOL, Tokyo, Japan). SEM imaging requires preparation of fixing the cells by washing the cells twice with PBS (Thermo Fisher), fixing for 15 minutes with 4% formaldehyde (Sigma-Aldrich) and washing twice with PBS, the samples were dried by washing two times for 5 minutes with distilled water, 15 minutes with 50% ethanol, 20 minutes with 70% ethanol and 20 minutes with 96% ethanol, followed by two hours air dry. The specimens were gold-sputtered (Auto Fine Coater, JEOL JFC-1300, Japan) and observed with the SEM at an accelerating voltage of 15 kV. Images were taken on days 3, 14 and day 21 from the top and with a 30° angle view.

The cell interaction can also be visualized by actin staining. This staining procedure is described in the part micro-scale scaffolds, as for now, it is only performed to explore its added value towards SEM imaging.

To gain insight into the cell interaction, the metabolic activity of the viable cells were evaluated on days 1, 3, 7, 11 and 14[61]. The specimens were transferred to a new 24-well plate to make sure that only the metabolic activity of the cells that were attached to the specimen was measured and not the metabolic activity of cells that were on the bottom of the well plate or the ones that were floating around. A 500 µl mixture of αMEM and Presto Blue (10%) (Thermo Fisher) was pipetted in two empty wells and added to the specimens, followed by a one-hour incubation at 37°C. After one hour, 100 µl of the medium of each well was pipetted into a 96-well plate, while the remaining medium was refreshed and the 24-well plate, including the specimens, was put back in the incubator. The fluorescence (530-595 nm) of the 96-well plate was measured with a Viktor X3 microplate reader

(PerkinElmer, Groningen, Netherlands)[59]. The results of the fluorescence of the medium with the cells were reduced by the mean results of the fluorescence of the medium without the cells. Finally, to enable the comparison of the results, all results were normalized over the surface area of each specimen.

2.4.1.2 Cell function

The cell function of mineralization was measured with an alizarin red S (ARS) staining (Sigma-Aldrich) which highlights the formed calcium on the specimens[62]. Since calcium is only produced by osteoblasts that are at least 12 days old, the mineralization was measured on day 21[63]. After fixing the cells, the staining was performed by adding a 2% ARS solution (pH = 4.1), incubating in the dark at room temperature for 30 minutes, and washing eight times with distilled water[64]. This procedure gave the calcium a red color and images of the top and bottom were made with the VHX-6000 microscope with a magnification of 300.

2.4.1.2.1 Image analysis

The images of the ARS staining from each specimen (n=4) were quantified with ImageJ (open-source image analysis software, http://rsb.info.nih.gov/ij/index.html)[50]. The mean grey value was measured and normalized over the surface area of each specimen. Finally, a bar graph was made from these results.

2.4.2 Micro-scale scaffolds

The second experiment was designed for the micro-scale scaffolds and should mimic the experiment of the bone-mimicking scaffolds. However, the fact that the size of the micro-scale scaffolds is almost identical to the size of the pre-osteoblasts ensures that the cells will cover this micro-scale scaffold faster than the bone-mimicking scaffold. Consequently, the cell culture will last for only 7 days and we cannot perform the exact same procedures. We performed SEM imaging on day 3 and on the last day of the experiment, day 7. The fact that the micro-scale scaffolds are attached to their substrate makes that the metabolic activity of the cells cannot be measured accurately, we either measure too many cells or we destroy the material. So, instead of measuring the cell interaction by the metabolic activity with presto blue, we chose to measure the cell interaction by the spreading and morphology of the cells with an actin staining. This actin staining shows the cytoskeleton and nucleus of the cells and is measured at different points in time. Finally, the cell function of mineralization with ARS staining can also not be applied on these scaffolds, since the duration of this experiment (7 days) is too short for mineralization to occur[63]. Another test that can show the cell function is the Runx2 staining which identifies the cells that are differentiated from pre-osteoblasts to osteoblasts[65].

The experiment for the micro-scale scaffolds, including the staining and imaging techniques which are shown in table 6, was performed three times, at different time points to ensure the reliability of the results. For each experiment, four specimens of each micro-scale scaffold were sterilized and placed into four 6-well plates. The specimens were cultured in 2 ml αMEM with 50.000 MC3T3-E1 cells for a total of 7 days. The well plate was then incubated (37 °C, 5% CO_2) to imitate the temperature of the human body. Every 2 days, the medium was refreshed with 500 µl differentiation medium (αMEM mixed with ascorbic acid and beta-glycerol-phosphate).

2.4.2.1. Cell interaction

To show the morphology of the cells on the surface of the micro-scale scaffolds, SEM images were taken on days 3 and 7. The specimens were prepared according to the procedure mentioned above and images were taken from the top and a 45° angle view.

An actin staining will, with a fluorescence microscope, highlight the cytoskeleton and nucleus of a cell. By evaluating the cytoskeleton on days 3 and 7, the attachment and spreading of the osteoblasts on the specimens will be obtained, and by evaluating the nucleus on days 3 and 7, unusual cell division could be obtained[66]. The actin staining requires preparation of fixing the cells, followed with staining by permeabilizing the cells with 0.5% Triton/PBS (Sigma-Aldrich) for 5 minutes at 4°C, followed by 5 minutes in 1% BSA/PBS at 37°C, one hour at 37°C in a mixture of 1% BSA/PBS and Rhodomine-

Phalloidine (1:100) to highlight the cytoskeleton, followed by washing three times for 5 minutes at room temperature with 0.5% Tween/PBS (Sigma-Aldrich), one hour at room temperature in a mixture of 1% BSA/PBS and DAPI (1:1000) to highlight the nucleus, and washing three times for 5 minutes at room temperature with 0.5% Tween/PBS. The staining was captured using the ZOE Fluorescent Cell Imager (Bio-Rad, Hercules, CA). The images were taken from the top layer of each specimen and were analyzed as described in 'Image analysis'. The bar graph showed that the higher the red intensity of the actin staining, the lower the grey value.

2.4.2.2. Cell function

At last, the function of the cells was evaluated by a Runx2 staining on day 7 that identifies the differentiation of the cells[67]. Therefore, the cells were fixed and the staining was performed by permeabilizing the cells with 0.5% Triton/PBS for 5 minutes at 4°C, followed by 5 minutes in 1% BSA/PBS at 37°C, one hour at 37°C in a mixture of 1% BSA/PBS and Runx2 primary polyclonal antibody (1:250), washing three times for 5 minutes at room temperature with 0.5% Tween/PBS, one hour at 37°C in a mixture of 1% BSA/PBS and secondary antibody Alexa Fluor 488 (1:200) and washing three times for 5 minutes at room temperature with 0.5% Tween/PBS. The staining was captured at the top layer of each specimen using the ZOE Fluorescent Cell Imager.

2.6 Statistical analysis

The first statistical analysis was performed to test the reliability of the experiment. Each experiment was performed multiple times, from which the results were evaluated to identify significant differences between the results measured at different time points. Ideally, no differences are found and all results of the same experiment can be combined. The statistical analysis was performed using SPSS (IBM Statistics, New York, United States), with the independent variable the time point of the measurement, and the dependent variable the grey value or metabolic activity. At first, a Shapiro-Wilk's test was performed to check if the data was normally distributed ($p > 0.05$), followed by Levene's test to check if the homogeneity of variance could be assumed ($p > 0.05$). If both tests succeeded, an independent t-test for the bone-mimicking scaffolds, and the one-way ANOVA test for the micro-scale scaffolds was performed. If one of these assumptions was not met, we referred to Jaccard (1998)[68]. According to this study, an independent t-test or one-way ANOVA can still be performed if the sample sizes are equal and the ratio of the largest group variance to the smallest group variance is less than three[68]. A significant difference was obtained by $p < 0.05$. When the data did not meet the assumptions nor the rules by Jaccard (1998), the non-parametric Mann-Whitney test instead of the independent t-test, and the Kruskal-Wallis test instead of the one-way ANOVA test, was performed[68].

All quantitative results were evaluated to identify significant differences between the specimens. The statistical analysis was performed for three different bone-mimicking scaffolds, three different micro-p-scale scaffolds and four different micro-s-scale scaffolds. Each evaluation day was tested separately, the independent variable was the design of specimen and the dependent variable was the grey value or metabolic activity. The data was tested on normal distribution and homogeneity of variance, if both tests succeeded, a one-way ANOVA test was performed. If one of these assumptions was not met, we referred again to Jaccard (1998)[68]. A significant difference was obtained by $p < 0.05$. If a significant difference was obtained, a Bonferroni post hoc test was executed to explain the differences. When the data did not meet the assumptions nor the rules by Jaccard (1998), the non-parametric Kruskal-Wallis test was performed[68]. Significance was again assumed at $p < 0.05$. If a significant difference was obtained, a Mann-Whitney test with Bonferroni post hoc test was executed to show which designs differed from one another.

Besides the one-way ANOVA or non-parametric Kruskal-Wallis test, a regression analysis was performed for the micro-scale scaffolds that were normally distributed and showed homogeneity of variance[69]. The dependent variable was the grey value and as independent variables, we used the parameters Poisson's ratio, stiffness and porosity. This analysis showed how much of the variance of the results could be explained by the variance of the parameters. It also tells us which parameter influences the results the most.

3. Results

The research was performed according to the aforementioned methods and materials. At first, all results regarding the bone-mimicking scaffolds are described, followed by all results regarding the micro-scale scaffolds.

3.1 Bone-mimicking scaffolds

3.1.1 Morphological characterization

The manufactured bone-mimicking scaffolds are shown in figure 15 and appendix 7.1. The method used to print these specimens influences the morphological properties. The manufactured morphological properties of the specimens are shown in table 7. The manufactured porosity of the specimens is lower than the designed porosity (75%). Nevertheless, the porosity is still within the limits of 50-90% required for the bone to be trabecular.
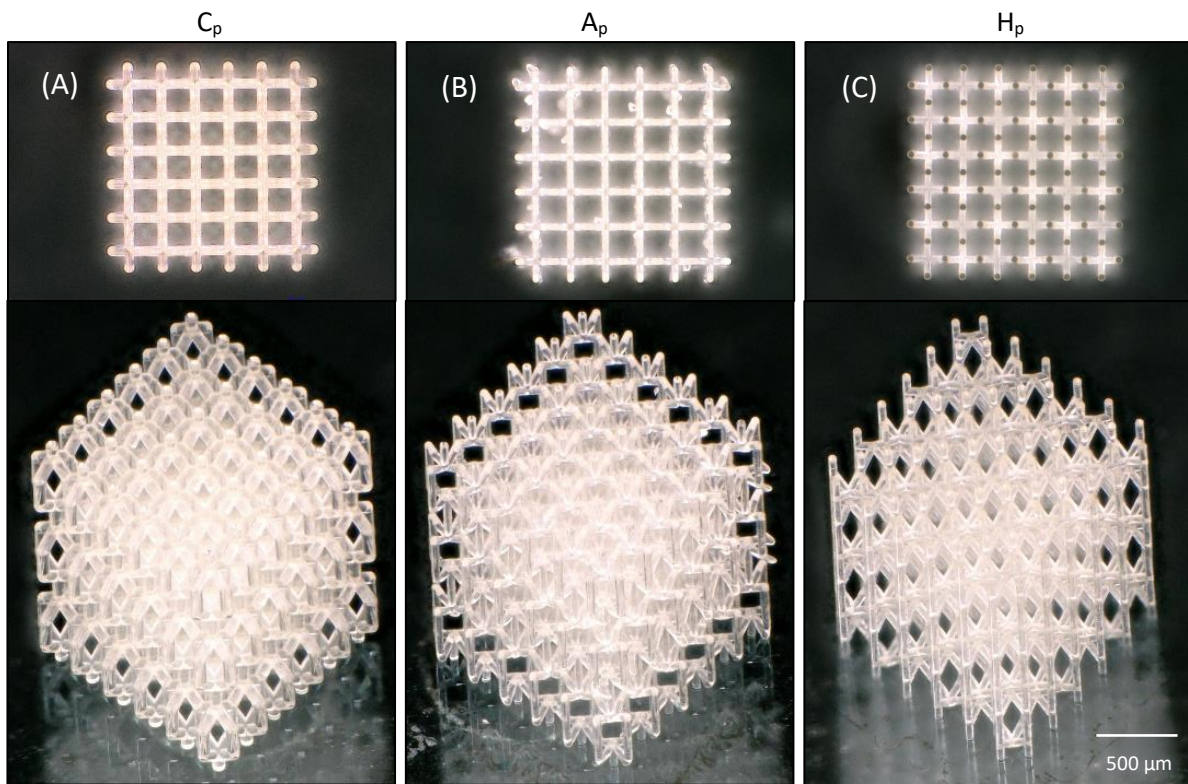
Figure 15. Printed bone-mimicking scaffolds where (A) shows C_p, (B) shows A_p and (C) shows H_p.

Table 7. Porosity (%) of the bone-mimicking scaffolds with their standard deviation (std).

Specimen		Designed porosity	Mean manufactured porosity	Manufactured porosity std.
C_p		75	74.1	1.0
A_p		75	73.3	2.6
H_p		75	71.9	2.9

3.1.2 Mechanical characterization

The material properties were obtained by a mechanical test of H_p, from which the test results were used to create a stress-strain curve. This curve showed where the first layer of the structure failed

(appendix 7.2) and the peak force of 4N, with a stress of 2.54 MPa and a strain of 2.98 % was reached (figure 16). The resulting stiffness (E) of H_p was calculated to be 119.76 ± 7.43 MPa.
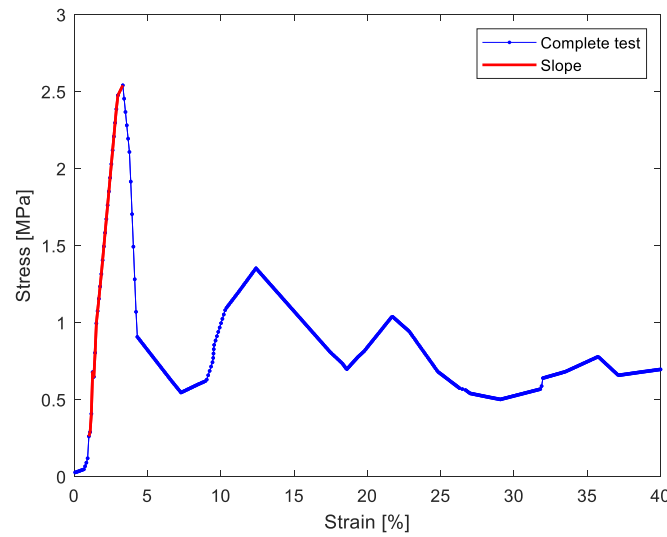
Figure 16. Stress-strain curve of the mechanical test of a hybrid bone-mimicking scaffold.

The bulk material of the FE model was set to have a Young's modulus of 1887.36 MPa to match the stiffness of H_p that was found in the experiment. Table 8 shows the material properties of all specimens that were obtained with the FE model.

Table 8. Mechanical properties of the bone-mimicking scaffolds.

Specimen		Designed porosity (%)	E (MPa)	v	v_{lat}
C_p		75	168.8	0.88	0.17
A_p		75	44.8	-0.55	-0.24
H_p		75	119.8	0.15	0.07

3.1.3 Biological characterization
The results of the biological characterization are divided into cell interaction and cell function. The cell interaction is visualized with SEM imaging, which show the morphology and spreading of the cells, and the metabolic activity is shown by presto blue. The actin staining is not included in this experiment as the results do not show added value towards SEM imaging (appendix 7.3). At last, the cell function is visualized with ARS staining that shows the cell mineralization.

3.1.3.1 Cell interaction
The cell interaction, visualized with SEM imaging, is shown in figures 17-19 and appendix 7.4. The images show that after 3 days only a few cells are attached to the specimens. Most of these cells are attached at the vertices of the specimens. After 14 days, the cells are spread over the entire specimens. This continued until day 21, where even more cells are attached to the specimens. On C_p and A_p it can be identified that, after 3 days, the cells are only attached to the top of the specimens, whereas on H_p the cells are also attached to the outside of the specimen. After 14 days it is shown that the vertical pillars from A_p and H_p are bend and the struts at the top view of H_p are bend towards each other (blue arrows in figures 18 and 19).
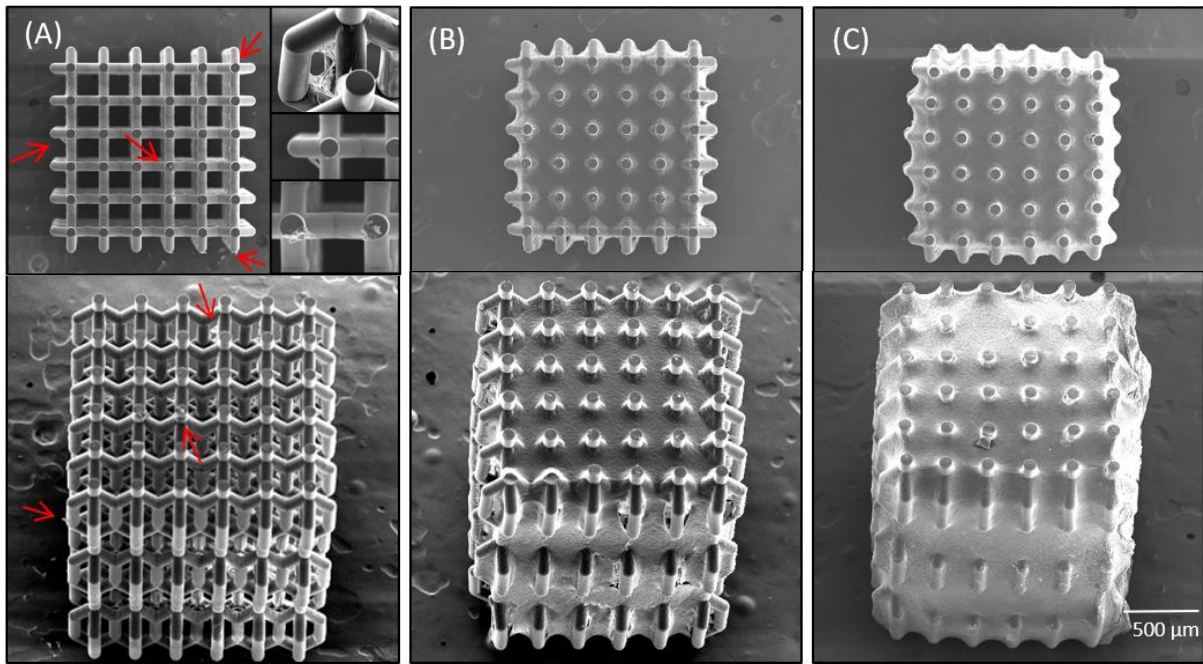
Figure 17. SEM images of C_p, top view and 30^0 angle view. Images show morphology of the cells on the surface after (A) 3 days (cells highlighted with red arrows), (B) 14 days and (C) 21 days.
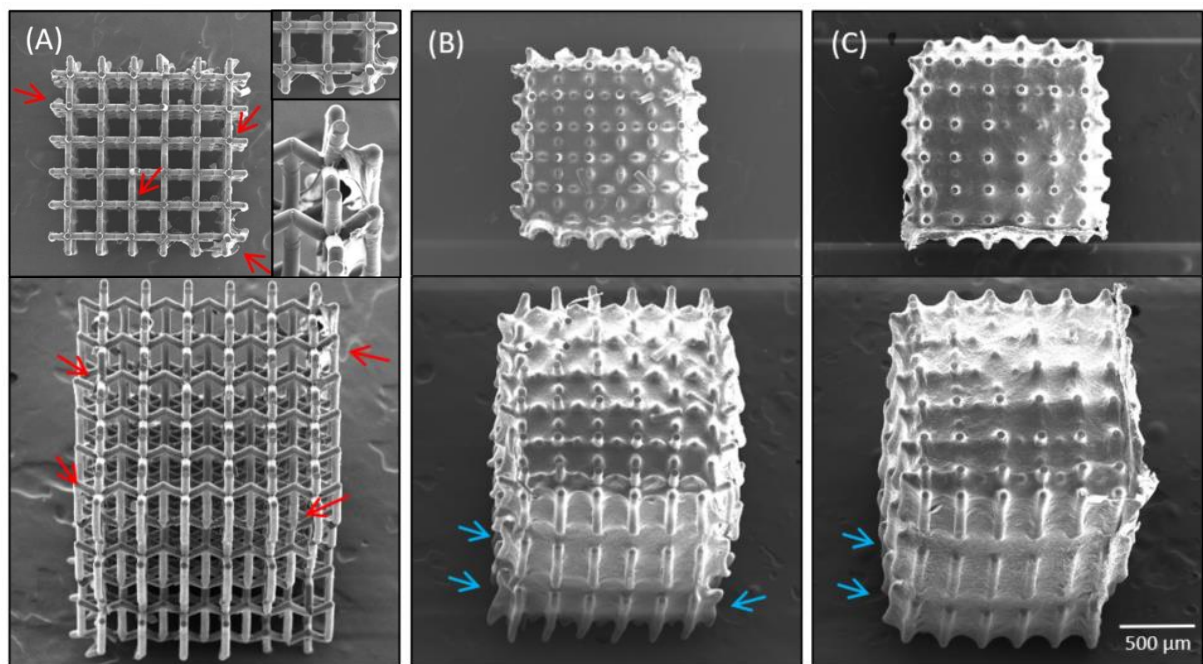
Figure 18. SEM images of A_p, top view and 30^0 angle view. Images show morphology of the cells on the surface after (A) 3 days (cells highlighted with red arrows), (B) 14 days and (C) 21 days. The blue arrows indicate bending of the struts.
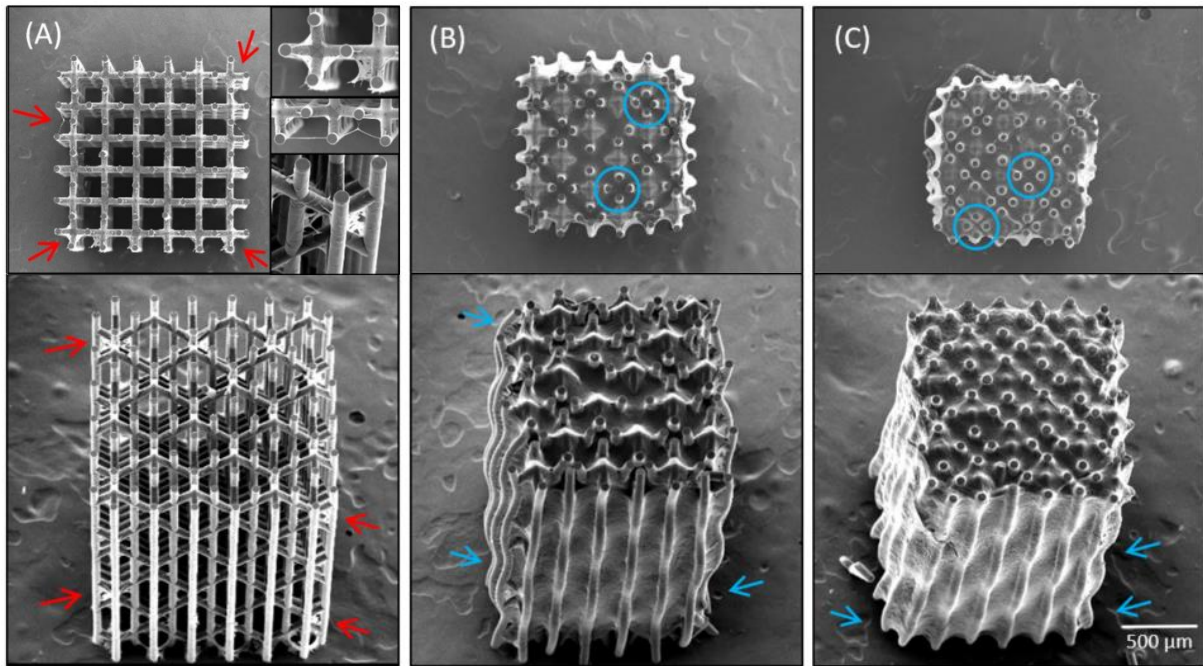
Figure 19. SEM images of H_p, top view and 30^0 angle view. Images show morphology of the cells on the surface after (A) 3 days (cells highlighted with red arrows), (B) 14 days and (C) 21 days. The blue arrows indicate bending of the struts.

The results of the metabolic activity, shown with presto blue, were identified as reliable, as the results at different time points did not show significant differences (appendix 7.5). Therefore, the results of the metabolic activity at different time points were combined.

The total results are shown in figure 20, where the significant differences between the specimens at every evaluating day is shown in the graph by '*' (appendix 7.6). On every evaluation day, the control group showed significant differences compared to all specimens. The significant differences between C_p and A_p were indicated on days 1 and 3 and a significant difference between A_p and H_p was indicated on day 14.
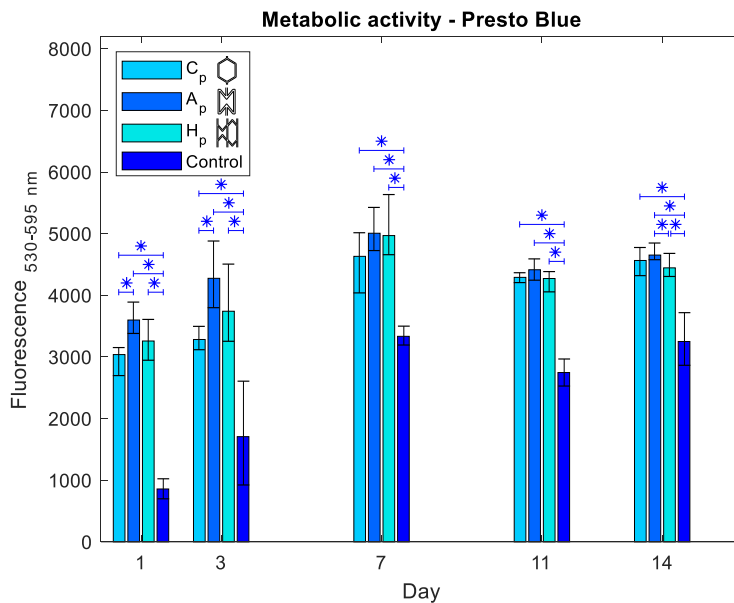
Figure 20. The results of the metabolic activity of the cells on the bone-mimicking scaffolds and control group (i.e. no specimen). Data is expressed as mean and error bars show the standard deviation. Significant differences ($p < 0.05$) are shown by *.

3.1.3.2. Cell function

The results of the ARS staining, to identify the mineralization of the cells, are shown in figure 21 and appendix 7.7. Figure 21 shows that the ARS staining on C_p only showed mineralization at the bottom of the image despite that the specimen is completely covered with cells. A_p and H_p show, with the ARS staining, that the entire top of the specimens are mineralized. It is shown that most mineralization occurred around the struts of the specimens.

The image analysis quantified the results of the ARS staining, which were identified as reliable, so we decided to combine the results of the ARS staining from different time points (appendix 7.8). The total results are shown in figure 22, where the significant differences between the specimens are shown in the graph by '*' (appendix 7.9). After 21 days, significant differences in mineralization were indicated between C_p and A_p and H_p (figure 22).
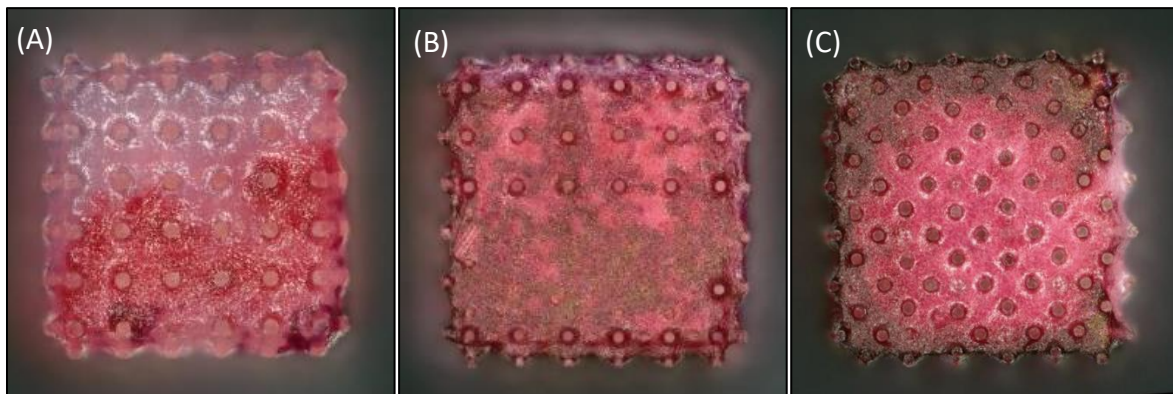
Figure 21. ARS staining to measure mineralization. (A) C_p, (B) A_p and (C) H_p.
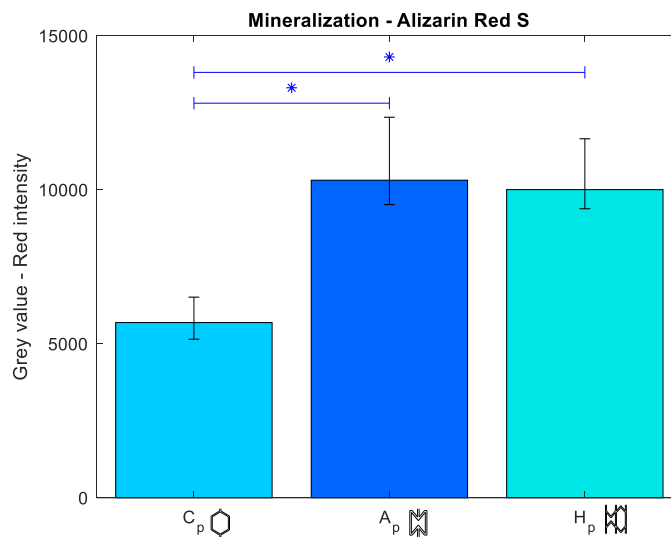
Figure 22. The results of the mineralization of the cells on the bone-mimicking scaffolds by ARS staining at day 21. Data is expressed as mean and error bars show the standard deviation. Significant differences (p < 0.05) are shown by *.

3.2 Micro-scale scaffolds

The fabricated specimens, with a default laser power of 50%, were inspected with the VHX-6000 microscope on surface smoothness and printing errors (figure 23). These results were used to fine-tune the printer settings. The specimen with the best surface smoothness and least printing errors was printed with 70% laser power.
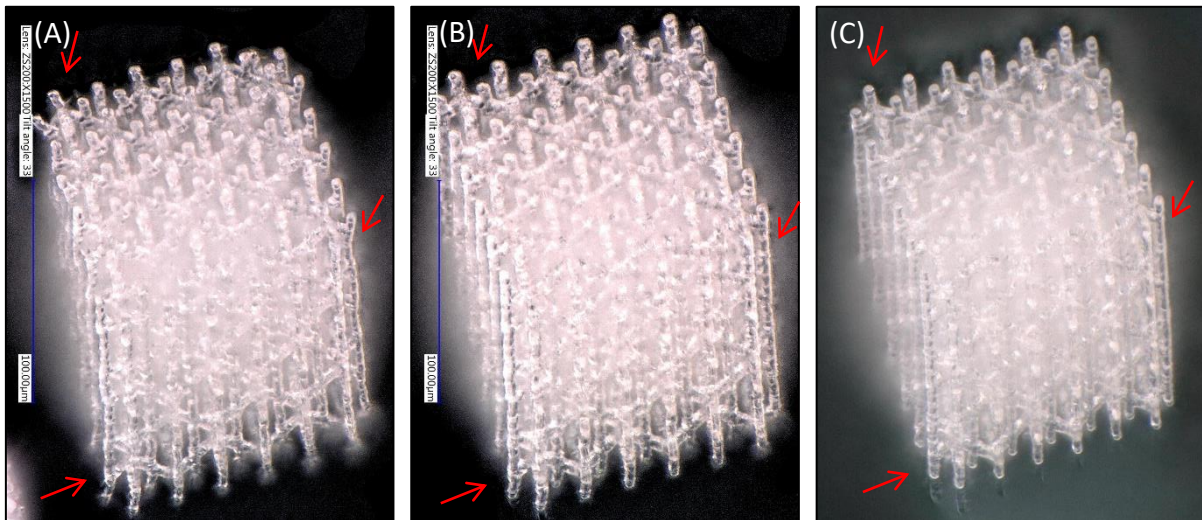
Figure 23. Fabricated H_p/H_s micro-scale scaffolds with different laser powers; (A) 40%, (B) 60%, (C) 70%. Red arrows indicate differences of the specimens.

3.2.1 Morphological characterization

The manufactured micro-scale scaffolds are shown in figure 24 and appendix 7.10. The method used to print these specimens influences the morphological properties. The actual morphological properties of the specimens are shown in table 9. The porosities were determined by measuring the actual strut thickness of each specimen. It showed that the porosity of the manufactured specimens is <5% lower than the designed porosities. Nevertheless, the porosity is still within the limits of trabecular bone, 50-90% porosity.

Table 9. Designed and manufactured porosity (%) of the micro-scale scaffolds.

Specimen		Designed porosity	Mean manufactured porosity	Manufactured porosity std.
C_p		75.0	72.9	5.7
A_p		75.0	71.9	5.6
H_p/H_s		75.0	70.5	2.4
C_s		78.1	77.0	2.2
A_s		64.1	61.2	3.8
CB_s		89.0	84.4	2.9
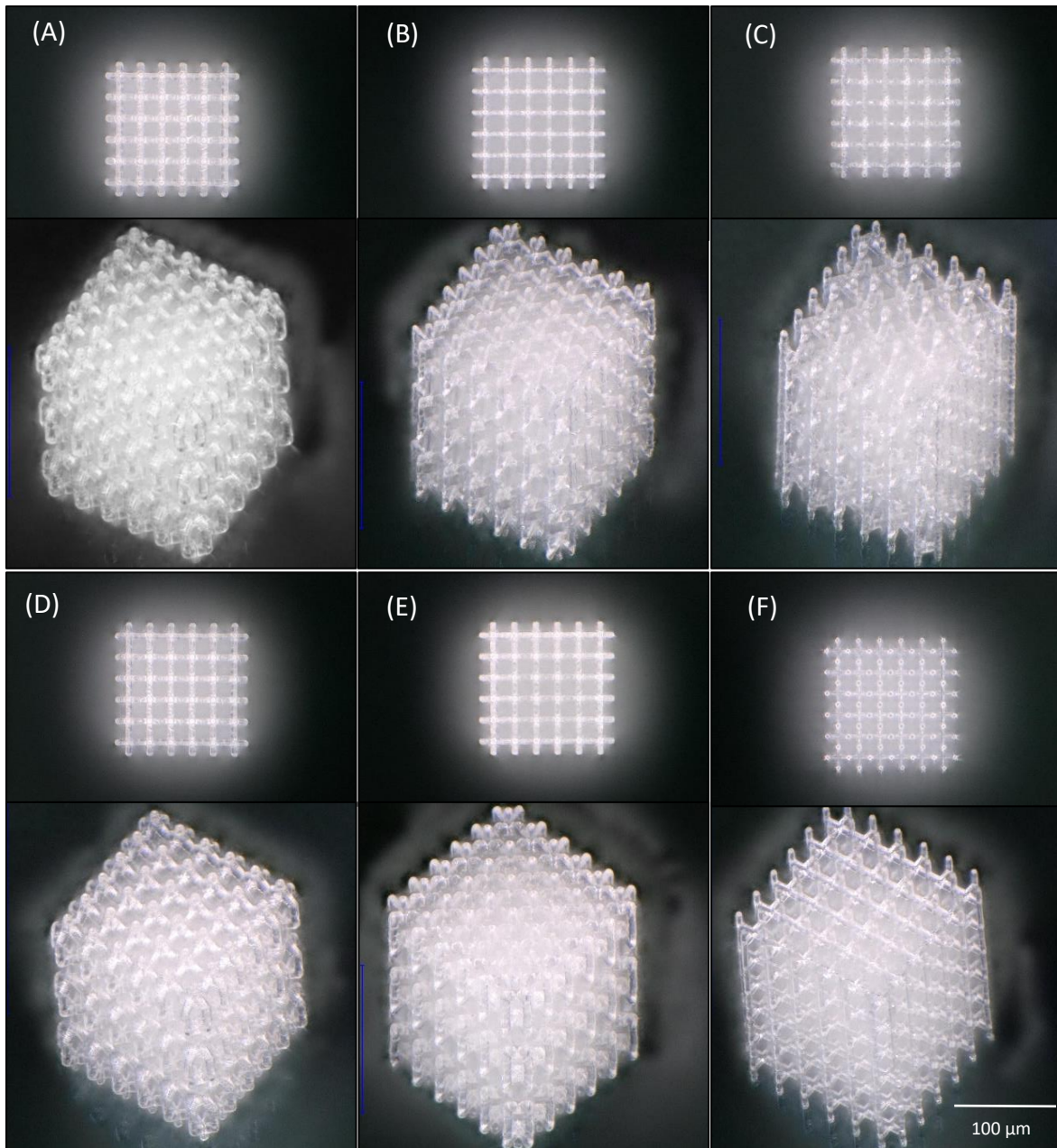
Figure 24. Printed micro-scale scaffolds where the images show (A) C_p, (B) A_p, (C) H_p/H_s, (D) C_s, (E) A_s and (F) CB_s.

3.2.2 Mechanical characterization

The mechanical properties are based on the material properties as calculated in 3.1. As the bone-mimicking and micro-scale scaffolds were printed with the same material, the Young's modulus of the bulk material is identical. The mechanical properties of the micro-scale scaffolds, obtained with the FE model, are shown in table 10.

Table 10. Mechanical properties of the micro-scale scaffolds.

Specimen		Designed porosity (%)	E (MPa)	v	v_{lat}
C_p		75.0	168.8	0.88	0.17
A_p		75.0	44.8	-0.55	-0.24
H_p/H_s		75.0	119.8	0.15	0.07
C_s		78.1	119.9	1.07	0.19
A_s		64.1	119.7	-0.24	-0.14
CB_s		89.0	120.0	0	0

3.2.3 Biological characterization

The results of the biological characterization are divided into cell interaction and cell function. The cell interaction is visualized with SEM imaging and actin staining that shows the morphology and spreading of the cells. The cell function is visualized with Runx2 staining that shows cell differentiation.

3.2.3.1 Cell interaction

The SEM imaging shows the morphology of the cells on the surface and the actin staining shows the morphology and spreading of the cytoskeletons of the cells. In figures 25-27, appendices 7.11 and 7.12 SEM images and the results of the actin staining are shown. After 3 days, the SEM images show that the cells are solely attached to the top part of the specimens on A_p, C_s and CB_s, whereas on C_p, H_p/H_s and A_s the cells are also attached to the outside of the specimens. The actin staining lights up the cytoskeleton of the cell and gives a similar result as the morphology shown with the SEM imaging. However, the spreading of the cytoskeleton is shown throughout the entire specimens with the actin staining and has therefore more cytoskeleton highlighted than shown with SEM imaging. After 7 days, all specimens show that the cells have divided and are climbing the specimens (SEM). The results of the actin staining show that the specimens are completely covered, and surrounded, by cytoskeleton. The SEM images show that A_p, H_p/H_s and CB_s have their vertical struts bend after 7 days of cell culture (blue arrows in figures 25-27).
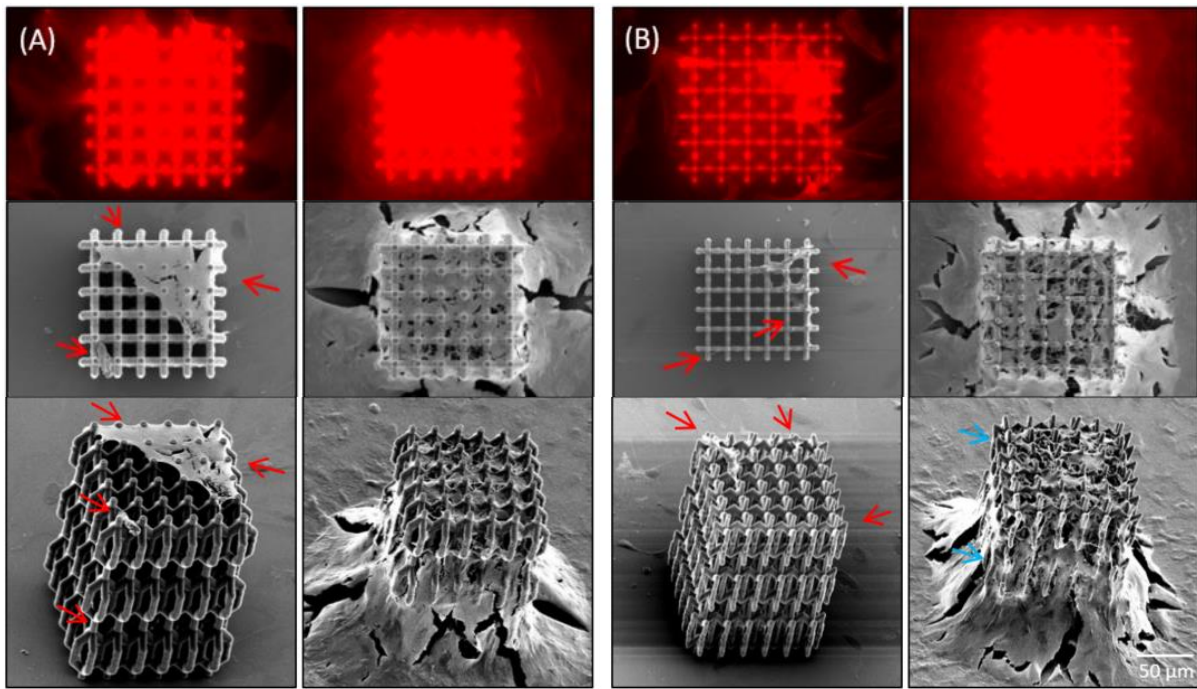
Figure 25. Images of actin staining and SEM images of (A) C_p and (B) A_p, top view and 45^0 angle view. Images show morphology of the cells on the surface after 3 days (cells highlighted with red arrows) and 7 days. The blue arrows indicate bending of the struts.
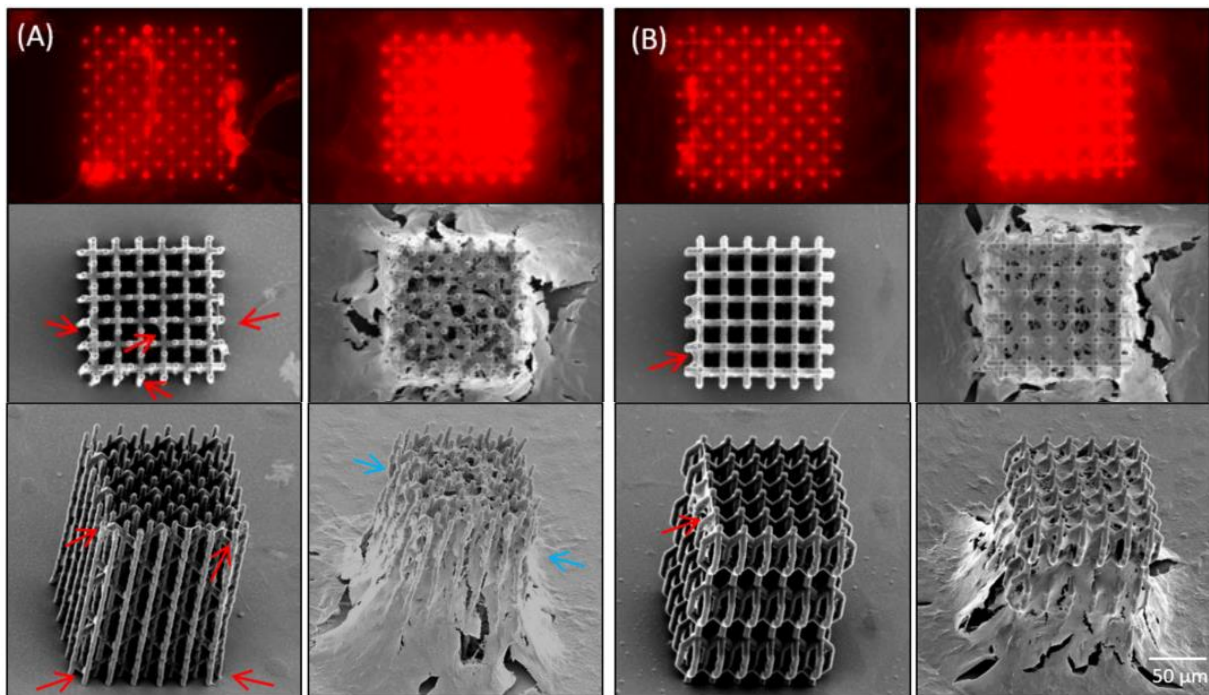
Figure 26. Images of actin staining and SEM images of (A) H_p/H_s and (B) C_s, top view and 45^0 angle view. Images show morphology of the cells on the surface after 3 days (cells highlighted with red arrows) and 7 days. The blue arrows indicate bending of the struts.
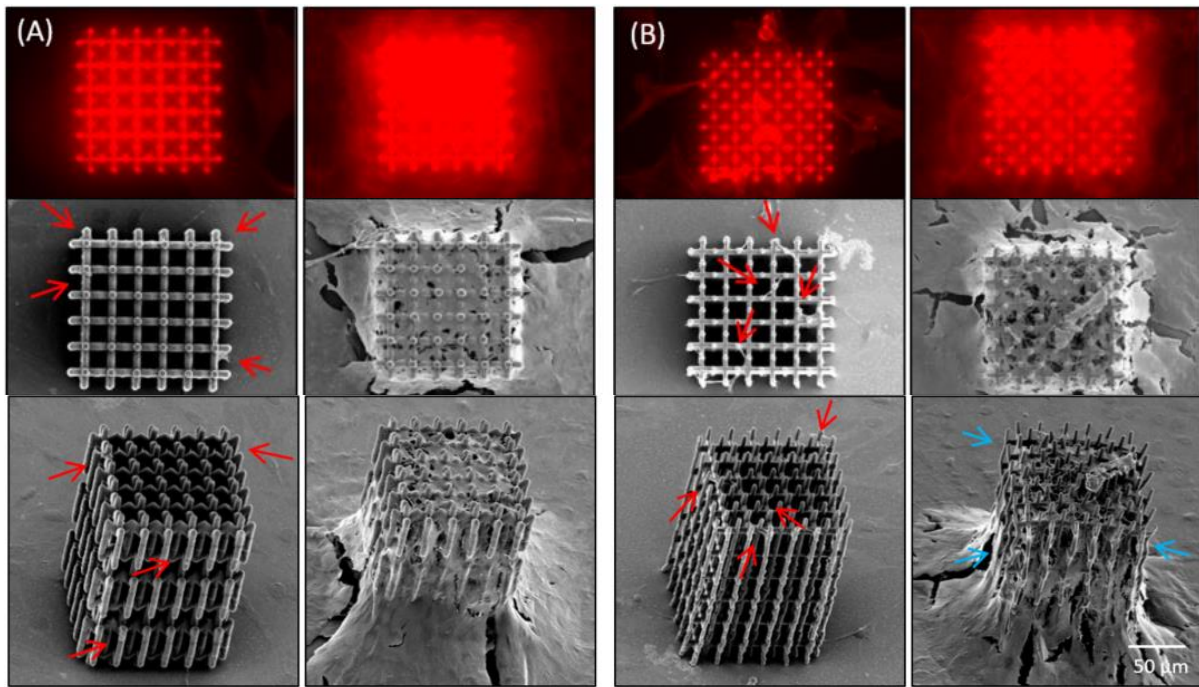
Figure 27. Images of actin staining and SEM images of (A) A_s and (B) CB_s, top view and 45^0 angle view. Images show morphology of the cells on the surface after 3 days (cells highlighted with red arrows) and 7 days. The blue arrows indicate bending of the struts.

The results of the actin staining after 3 days, to identify the morphology and spreading of the cells, were quantified, identified as reliable, and combined for further analysis (appendix 7.12). The total results are shown in figure 28, where the significant differences between the specimens is shown in the graph by '*' (appendix 7.14). Figure 28 shows that, for the micro-p-scale scaffolds, C_p has significantly more cytoskeletons attached than H_p and that H_p has significantly more cytoskeletons attached than A_p. For the micro-s-scale scaffolds, most cells attached to A_s and C_s, less to H_s and the least to the control group CB_s. A linear regression analysis showed that 40.2% of the variance in the data could be explained by the variance of the Poisson's ratio, porosity and stiffness, respectively (appendix 7.14).

The results of the actin staining of day 7 are not quantified by image analysis. The surrounding cytoskeleton of the specimens is coloring the entire image red, which makes the quantification unreliable.
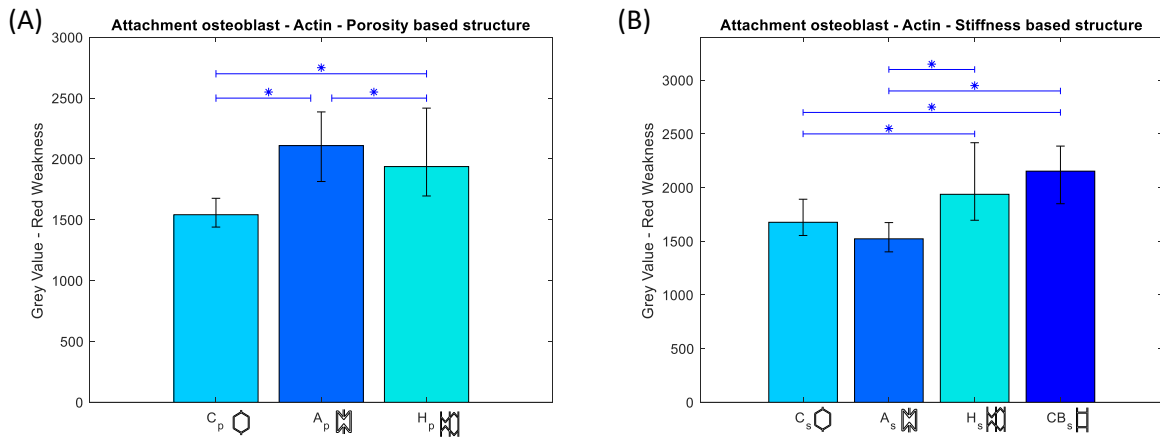
Figure 28. The results of the attachment of the cells after 3 days on the, (A) micro-p-scale and (B) micro-s-scale scaffolds (control: CB_s), visualized by actin staining. The lowest bar shows the highest intensity of red. Data is expressed as mean and error bars show the standard deviation. Significant differences ($p < 0.05$) are shown by *.

3.2.3.2 Cell function

The results of the cell function are shown in figures 29, 30 and appendix 7.15 with the Runx2 staining. The images show that the cells on C_p of the micro-p-scale scaffolds show most differentiation, followed by H_p, and least by A_p. The micro-s-scale scaffolds show the most differentiation on C_s and A_s and less differentiation on H_s and CB_s, that both have a Poisson's ratio close to zero.
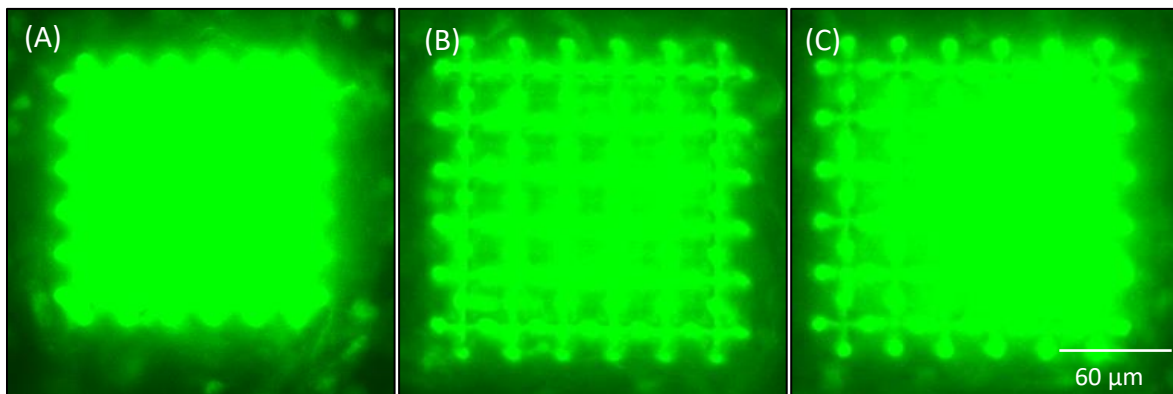
Figure 29. Images of the Runx2 staining of the micro-p-scale scaffolds, performed on day 7. This staining shows the differentiation of the cells. (A) C_p, (B) A_p, (C) H_p.
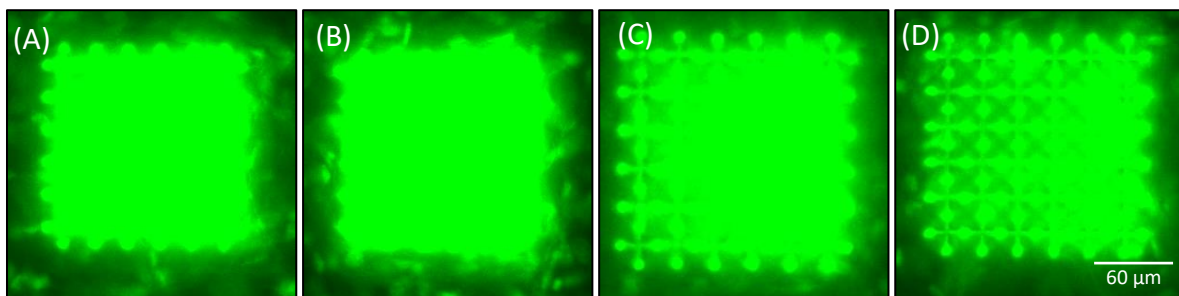
Figure 30. Images of the Runx2 staining of the micro-s-scale scaffolds, performed on day 7. This staining shows the differentiation of the cells. (A) C_s, (B) A_s (C) H_s, and (D) CB_s (control).

4. Discussion

In this graduation project, we have explored the behavior of bone cells on scaffolds with negative, zero and positive Poisson's ratio. Two different experiments were performed to determine the MC3T3-E1 pre-osteoblastic cell response on different meta-biomaterials. The first experiment included three bone-mimicking scaffolds and the second experiment included six micro-scale scaffolds. All meta-biomaterials were exposed to a cell culture of MC3T3-E1 pre-osteoblastic cells. This cell culture was exposed to different staining procedures and imaging techniques to acquire insight into cell interaction and function. The results will be discussed in detail in the following paragraphs, together with the challenges and limitations of this research. Finally, some recommendations for future work will be presented.

4.1 Bone-mimicking scaffolds
The porosity of the specimens was determined using the strut thickness (table 7). It appeared that the manufactured porosity was within 5% lower than the designed porosity and, consequently, the manufactured specimens contained more material than the designed specimens. A potential explanation can be that each specimen was built in parts. The Nanoscribe has a building range which is smaller than the designed specimens. Therefore, each specimen is split into smaller parts that were printed on top of each other. The repolymerization at these welding points can result in a lower porosity of the manufactured specimens[47].

The experiment for the bone-mimicking scaffolds explored the cell interaction with SEM imaging and presto blue and the cell function with ARS staining. Besides these tests, literature also mentions an actin staining to observe cell interaction[70-72]. Therefore, the actin staining, which highlights the cytoskeleton and nucleus of the cells, was performed and analyzed on its added value to the results of this experiment. The results of the actin staining did solely highlight the cytoskeleton of the cells without its nucleus. A potential explanation can be that the second antibody, DAPI, which should highlight the nucleus, had lost its function. Therefore, it was not able to explore if the cell division was unusual. The results of the actin staining were compared with the results of the SEM imaging. The SEM imaging clearly identified where the cells were attached to the specimens, whereas the actin staining was less conclusive (appendix 7.3). The actin staining highlighted both the specimen, as well as the cytoskeletons of the attached cells, and given the small size of the attached cells, they were too small to be distinguished. Therefore, it was decided to not include the actin staining in this experiment. In the previous studies, the structures were not highlighted by the actin staining and the actin staining and SEM imaging showed different results[70-72].

After 3 days, the differences in cell morphology between the specimens were shown with SEM imaging (figures 17-19). These differences can be explained by cell seeding. Each specimen was placed in a 24-well plate and seeded with drops of a solution of αMEM and MC3T3-E1 pre-osteoblastic cells. While seeding, some cells were directly pipetted on the specimen while other cells were floating in the solution and attached to the bottom of the well plate. Consequently, there can be a big difference in the number of attached cells to the specimens, primarily after 1-3 days, which is not based on the type of specimen used. On days 1, 3, 7, 11 and 14 the specimens and their attached cells were transferred to a new well plate leaving the remaining cells on the bottom of the well plate. This way the metabolic activity of the cells on the specimens was observed without the interference from the surrounding cells. After 14 days of cell culture, the cells completely covered the specimens. A_p and H_p showed that their vertical struts were bent. The strut thickness of C_p ensures that this specimen is not affected by these forces (table 2). After 21 days of cell culture, the bending of the struts decreased. According to Zhang et al. (2013), an explanation for the initial bending could be the forces of the cells that are acting on the struts. This study explained the decrease of this bending by the differentiating cells on the inside of the specimen that pushed the struts back to their original position[18].

The presto blue is used to identify the metabolic activity of the cells. The measurements that included false data, data where the specimen was not completely covered by the presto blue, were excluded from the results. On day 1, the specimen with a positive Poisson's ratio, C_p, had a significantly lower metabolic activity rate than the specimens with a negative, and almost zero Poisson's ratio, A_p and H_p, respectively. The fact that C_p was floating on the αMEM, while the other specimens were completely covered by αMEM (figure 31), could be the reason. Cells may have had difficulty attaching to the inside of the C_p specimen. There was intensively searched for a potential explanation of the floating C_p. The buoyant forces of the αMEM and the densities of the αMEM and C_p could not explain the floating as the buoyant forces of the αMEM were higher than the weight of C_p and the density of C_p was higher than the density of αMEM[73, 74]. The surface tension of C_p was higher than the surface tension of αMEM (equation 10) which trapped the air within the specimen and that could be a potential explanation why C_p was floating[75-77]. After 7 days of cell culture, the C_p specimen has sunk and was completely covered by αMEM. From now on, cells were able to reach the inside of the specimen. On day 7, the plateau of the cells was reached, meaning all the specimens were completely filled with cells. After 14 days, there was a significant difference between A_p and H_p. A possible explanation could be that the reached plateau of the cells showed a varying metabolic activity rate. If H_p is varying low and A_p is varying high, this could explain the differences.

$$\gamma = \frac{F}{l} \qquad [10]$$
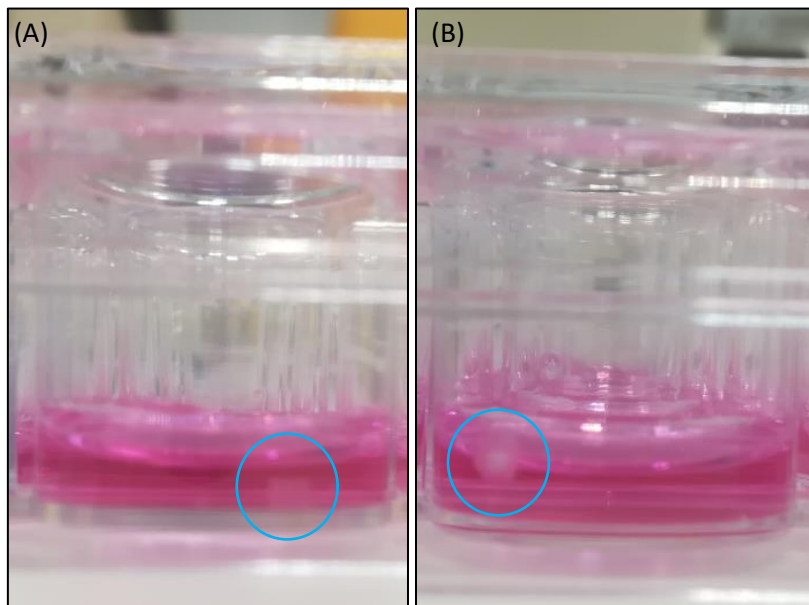
Figure 31. Side view of 24-well plate where (A) shows that A_p is on the bottom of the well plate and is completely covered by αMEM and (B) shows that C_p is floating and that air is trapped inside the specimen.

During the entire experiment, it was shown that the results of each specimen was significantly different from the results of the control group, so we can state that our specimens contributed to the cell response. A previous study by Kim et al. (2017) tested the cell proliferation of MG-63 osteoblast-like cells on PLGA specimens[78]. The results showed that the cell proliferation of the auxetic specimen (negative Poisson's ratio) after 1 and 3 days of cell culture had beneficial differences towards the conventional specimen (positive Poisson's ratio), but after 5 days of cell culture, there were no significant differences anymore. The results after 1 and 3 days of this study are not supported by the results from this graduation project because the evaluated differences were explained by the floating C_p. In contrast, the results after 5 days of cell culture were supported by this graduation project as no significant differences were shown.

The ARS staining is used to identify the mineralization which tells us where calcium was formed on the specimens. The results showed a large standard deviation that might be caused by the measured area; the bottom of the specimens showed less mineralization than the top. Furthermore, the results showed that the cells attached to C_p formed significantly less mineralization than the cells attached to A_p and H_p. A potential explanation can be found in the research of Maharjan et al. (2020), which showed that specimens with a higher stiffness had a higher mineralization rate on day 21[79]. This is in contrast to the results of this graduation project, which were also measured on day 21. The specimen with positive Poisson's ratio C_p had the highest stiffness of the bone-mimicking scaffolds and showed the lowest mineralization rate, whereas the specimen with the negative Poisson's ratio A_p had the lowest stiffness and showed the highest mineralization rate.

4.2 Micro-scale scaffolds

The porosity of the specimens after manufacturing was also within 5% lower than the designed porosity (table 9). In contrast to the bone-mimicking scaffolds, the micro-scale scaffolds were printed as one part which makes that the difference in porosity cannot be explained by the printing procedure. However, an explanation could be in the fact that the micro-scale scaffold was printed with the same parameters as the bone-mimicking scaffolds. The larger the microscope objective, the bigger the meta-biomaterial that can be printed. If a larger microscope objective is used for a smaller print, the meta-biomaterial is printed less smooth despite improvements made from altering the laser power. This could explain the difference in the designed and manufactured porosity. An alternative is to use a finer microscope objective, however, this would also require the use of a different material/photoresist and substrate[47]. The comparison between the bone-mimicking scaffolds and the micro-scale scaffolds would therefore be more difficult.

The mechanical properties of the micro-scale scaffolds were based on the mechanical tests that were performed on the bone-mimicking scaffolds. Based on these test results, the Young's modulus of the bulk material was calculated and used in a FE model to determine the mechanical parameters of the specimens. Unfortunately, our micro-scale scaffolds had a rough surface, caused by the big microscope objective, which could affect the stiffness of the material. To check the mechanical parameters of the specimens, another mechanical test would be required.

During the sterilization procedure, several specimens separated from their substrate and got lost, this led to a difference in the sample sizes of the experiments.

The SEM images were taken on day 3 and day 7. After 3 days, most of the cells were attached to different places at the top, and some cells were attached to the side of the specimens. A potential explanation that most cells attached to the top can be that the specimens were attached to the substrate while seeding. The cells attached to the side of the specimens did not divide according to the designed Poisson's ratio of the specimen because the lateral Poisson's ratio is different from the top. According to the SEM images, C_p had the most cells attached, followed by CB_s, C_s and A_p and the least cells were attached to H_p/H_s and A_s. A potential explanation for this difference can be the specimen/cell ratio. As mentioned before, each specimen has about the same size as the MC3T3-E1 pre-osteoblastic cells and, therefore, it is harder for the cells to find the specimen. This difference is not based on the differences in design, but on the fact that the cells did or did not find the specimen. The specimens were attached to the substrate during this experiment and it was shown that after 7 days the cells were climbing onto the specimens. Therefore, the cell response was influenced by the cells attached to the substrate and the specimen. However, only the cell response of the cells attached to the specimen was desired. The SEM imaging showed that the vertical struts of A_p, H_p/H_s and CB_s were bent. We noticed this bending after 7 days, at the end of the experiment. We were therefore unable to see whether they would bend back at some point, similar to the bone-mimicking scaffolds.

In contrast to the first experiment, the size of the MC3T3-E1 pre-osteoblastic cells are now almost identical to the size of the specimens and are clearly highlighted with the actin staining. The results of the actin staining, after 3 days, was quantified by ImageJ. The meta-p-biomaterials showed that the

specimen with the positive Poisson's ratio, C_p, had the most attached cytoskeletons, followed by the specimen with a Poisson's ratio close to zero, H_p, and the specimen with a negative Poisson's ratio, A_p, showed the least cytoskeleton attachment. The meta-s-biomaterials showed that the specimens with the positive and negative Poisson's ratio, C_s and A_s, respectively, had the most cytoskeleton attachment, followed by the specimens with a Poisson's ratio close to zero, H_s, and CB_s. A regression analysis of the results after 3 days showed that 40.2% of the variance of the actin staining results (meta-s-biomaterials) could be explained by the variance of the Poisson's ratio. The actin staining performed after 7 days showed that the cells have spread, and are climbing, over the entire specimens. Therefore, the boundary of the specimens is not clear and no image analysis can be performed. Summarizing, for the meta-p-biomaterials, C_p indicated an enhancement in cell response. In contrast, the auxetic and conventional micro-s-scale scaffold with negative and positive Poisson's ratio, respectively, indicated an enhanced cell response.

The Runx2 staining highlighted the cells that were differentiated from pre-osteoblasts to osteoblasts. The results of the Runx2 staining showed that, for the meta-p-biomaterials, most differentiated cells were attached to C_p (positive Poisson's ratio), which had the highest stiffness. For the meta-s-biomaterials, A_s (negative Poisson's ratio) and C_s (positive Poisson's ratio) showed the best results and H_s and CB_s showed the least differentiation (Poisson's ratio close to zero). Both results of the actin and the Runx2 staining indicated that for the micro-p-scale scaffolds, C_p (positive Poisson's ratio, high stiffness, 75% porosity), and for the micro-s-scale scaffolds, A_s (negative Poisson's ratio, 120 MPa, 64% porosity) and C_s (positive Poisson's ratio, 120 MPa, 78% porosity) enhances the response of the cells at an early stage, which was also found by Uchida et al. (2014)[80]. The micro-s-scale scaffolds are different in porosity and Poisson's ratio, therefore these parameters could influence the results. Mandal et al. (2009) showed that a higher porosity leads to higher cell proliferation[38]. However, the regression analysis of the results of the actin staining showed that the variance in Poisson's ratio influenced the variance in results the most. Together with the fact that the auxetic specimen has a 64% porosity and the conventional specimen has a 78% porosity, results that a negative Poisson's ratio in combination with high porosity and high stiffness should lead to the best cell response.

The SEM images showed that all specimens were completely covered by cells. Comparing this to the results of the staining procedures, the differences in results of the staining procedures could not be explained by the results of the SEM images. An explanation for this difference could be that the SEM only captures the outside of the specimens, whereas the staining procedures are imaged with the ZOE Fluorescent Cell Imager that captures the staining of the one layer, but also captures the illuminated staining of the lower layers. Therefore, the differences in staining results should be explained by the cells that are attached to the inside of the specimen.

4.3 Length-scale comparison

The results of the bone-mimicking and micro-p-scale scaffolds were conflicting as the bone-mimicking scaffolds showed the least cell response on the C_p specimen, whereas the micro-p-scale scaffolds showed the most cell response on C_p. This contradiction could again be explained by the floating specimen of the bone-mimicking scaffolds. Furthermore, A_p showed the most cell response of the bone-mimicking scaffolds, unfortunately they were non-significant. However, A_p showed the least promising results of the micro-p-scale scaffolds. Therefore, the results of the specimens based on the same porosity in meso- and micro-scale remain inconclusive.

The results of the specimens based on the same stiffness were only performed on the micro-scale scaffolds. The results showed that the auxetic and conventional micro-s-scale scaffold, with negative (A_s) and positive (C_s) Poisson's ratio showed an enhancement of the cell response in cell interaction and function. It was shown that the specimens with a Poisson's ratio close to zero showed the least cell response. As described before, a negative Poisson's ratio in combination with high porosity and high stiffness should lead to the best cell response. There is no conclusive result that this combination is able to enhance the cell response at mesoscale.

4.4 Challenges and limitations

The first experiment tested three different meta-p-biomaterials, varying in Poisson's ratio and stiffness, at mesoscale. As prior research showed that the porosity enhanced cell proliferation, we removed the influence of the porosity[38, 81, 82]. Therefore, the results of the bone-mimicking scaffolds could be based on the variance of the Poisson's ratio or the variance of the stiffness. To research the influence of the Poisson's ratio on cell response in more detail, it would be an improvement to include the meta-s-biomaterials in the first experiment, whereas the specimens used in the experiment was varying in porosity and stiffness.

Both experiments included morphological and mechanical characterization, a cell culture, staining procedures and SEM imaging. The first experiment measured the metabolic activity with presto blue and mineralization with ARS staining and the second experiment performed an actin and Runx2 staining. The procedures used for all of these tests have been broadly used in the literature[52, 61, 62, 66, 67]. However, the morphological characterization of all the meta-biomaterials was based on equations 1-4. We performed the morphological characterization in exactly the same way as the calculation for the initial porosity. To check the morphological characterization, weighing of the printed specimens could be used[83, 84]. Unfortunately, it was not possible to perform this weighing afterward, as all the specimens were used in the cell culture. Therefore, next time, the printed specimens should be weighted before the cell culture starts.

The significant differences in the results of the staining were not all explained by the SEM images. Including 3D imaging, to visualize not only the exterior of the specimens but also the interior, would be an improvement and also enable the comparison of the imaging results to the results of the staining procedures. A couple of specimens were sent to an external company to be imaged with a high-end confocal microscope (ZEISS LSM 980 Airyscan 2, OberKochen, Germany). This was done after the SEM imaging, and since the specimens were gold-sputtered, it was no longer possible for the high-end confocal microscope to image them.

Another limitation of the study considers the presto blue reagent. During this test, the specimens were detached from their substrate and placed in a 24-well plate together with the αMEM. The specimens were floating around in the αMEM and thus not standing straight. At first, we placed the specimens upright, but while moving the well plate, the specimens fell over. The cells were then seeded on the lateral position of each specimen that fell over. As mentioned before, the lateral Poisson's ratio is different from the Poisson's ratio from the top. Therefore, the to be determined Poisson's ratio influence of the specimens could not be investigated completely. An improvement would be to fix the specimens upright to the well plate while enabling the transfer of the specimens to measure the metabolic activity with presto blue.

A limitation of the first experiment was the floating of C_p at the start of the experiment. It was shown that after 7 days of cell culture, the specimen has sunk. A measurement of the metabolic activity on day 5 should have given a better insight into when the C_p specimen sank and could help to explain the results of this specimen.

The actin and Runx2 staining were imaged with the ZOE Fluorescent Cell Imager. This microscope can only focus on and measure one layer. In this graduation project, the results are based on measurements of the top layer of the specimens which includes the illumination of lower layers. It would be an improvement to measure the staining over the entire specimens using pictures from a 3D microscope for fluorescence.

4.5 Potential applications and future work

This graduation project was designed to gain knowledge in the behavior of bone cells on scaffolds with negative, zero and positive Poisson's ratio. Besides the use of a scaffold as a bone graft, other applications in which bone growth is an important factor that could potentially benefit from these scaffolds. A hip-implant, for example, also requires bone ingrowth and the sooner this happens, the sooner the patient will be able to fully use his/her new hip. The results of this study could for instance contribute to the design of the surface of these implants. The specimen with a negative Poisson's ratio

in combination with high porosity and high stiffness should enhance the cell response and could also be implemented on the surface of other applications to speed up the bone ingrowth process.

To extend the results found in this study, different focus points are elaborated. In the study of Zhang et al. (2013) an unusual cell division was found on an auxetic scaffold[18]. This unusual cell division could be identified with an actin staining. The first antibody of the actin staining highlights the cytoskeleton of the cells while the second antibody of actin staining, DAPI, highlights the nucleus of the cells, which could identify an unusual cell division[85]. Unfortunately, the second antibody did not highlight the nucleus during our experiment. Therefore, the unusual cell division could not be investigated in this graduation project, but should definitely be considered in future work.

The study of Choi et al. (2016) showed that the cell proliferation of MG-63 osteoblast-like cells enhanced under compression[17]. Compression is the most frequent loading type in the human body, so it is important to see how the specimens react to this loading type[86]. In this study, the tests were performed without any compression. To apply compression on the specimens, it is a possibility to perform the cell culture in a well plate with a designed height. This height is smaller than the height of the specimen so it is applying pressure. By altering the height of the well plate, the amount of compression can be variated.

Future research could also include, as mentioned before, the meta-s-biomaterials on mesoscale. The results can then be compared to the results of this graduation project to see whether a negative Poisson's ratio in combination with high porosity and high stiffness indeed enhances the cell response at multiple length scales.

5. Conclusion

The aim of this graduation project was to expand the knowledge on scaffold cell interaction, using scaffolds with negative, zero and positive Poisson's ratios. Conventional, auxetic and hybrid meta-biomaterials were tested on their ability to enhance the cell response at different length scales. The morphological and mechanical properties were determined, and the MC3T3-E1 pre-osteoblastic cell response was explored using different staining procedures and SEM imaging. The results of the staining procedures on the bone-mimicking scaffolds showed only minor, non-significant differences. The results of the micro-scale scaffolds based on the same porosity showed an enhancement in cell interaction and function of the conventional meta-biomaterial (positive Poisson's ratio). The results of the micro-scale scaffolds based on the same stiffness showed that most cytoskeletons were attached to the conventional and auxetic (positive and negative Poisson's ratio, respectively) scaffolds and that these scaffolds also contained the highest number of differentiated cells. It was concluded that a meta-biomaterial with a negative Poisson's ratio in combination with high porosity and high Young's modulus seems to enhance the cell response of the MC3T3-E1 pre-osteoblastic cells at micro-scale. Future work will be needed to explore whether the auxetic meta-biomaterial with negative Poisson's ratio in combination with high porosity and high stiffness will also enhance the cell response of the MC3T3-E1 pre-osteoblastic cells at mesoscale.

6. Bibliography

1. Wang W, Yeung KWK. Bone grafts and biomaterials substitutes for bone defect repair: A review. Bioactive Materials. 2017;2(4):224-47.
2. Gugala Z, Lindsey RW, Gogolewski S. New Approaches in the Treatment of Critical-Size Segmental Defects in Long Bones. Macromolecular Symposia. 2007;253(1):147-61.
3. Clerkship O. Describe the process of bone remodeling. In: Cycle BR, editor. OrthopaedicsOne: The Orthopaedic Knowledge Network; 2011.
4. Eriksen EF. Cellular mechanisms of bone remodeling. Reviews in Endocrine and Metabolic Disorders. 2010;11(4):219-27.
5. Ulrich D, Van Rietbergen B, Laib A, ŘUegsegger P. The ability of three-dimensional structural indices to reflect mechanical aspects of trabecular bone. Bone. 1999;25(1):55-60.
6. Hadjidakis DJ, Androulakis II. Bone Remodeling. Annals of the New York Academy of Sciences. 2006;1092(1):385-96.
7. Reichert JC, Saifzadeh S, Wullschleger ME, Epari DR, Schütz MA, Duda GN, et al. The challenge of establishing preclinical models for segmental bone defect research. Biomaterials. 2009;30(12):2149-63.
8. Qiu Z-Y, Cui Y, Wang X-M. Natural Bone Tissue and Its Biomimetic. Elsevier; 2019. p. 1-22.
9. Laurencin C, Khan Y, El-Amin SF. Bone graft substitutes. Expert Review of Medical Devices. 2006;3(1):49-57.
10. Jayakumar P, Di Silvio L. Osteoblasts in bone tissue engineering. Proceedings of the Institution of Mechanical Engineers, Part H: Journal of Engineering in Medicine. 2010;224(12):1415-40.
11. Detsch R, Will J, Hum J, Roether JA, Boccaccini AR. Biomaterials. In: Kasper C, Charwat V, Lavrentieva A, editors. Cell Culture Technology. Cham: Springer International Publishing; 2018. p. 91-105.
12. Nicolaou ZG, Motter AE. Mechanical metamaterials with negative compressibility transitions. Nature Materials. 2012;11(7):608-13.
13. Zadpoor AA. Mechanical meta-materials. Materials Horizons. 2016;3(5):371-81.
14. De Jonge C, Kolken H, Zadpoor A. Non-Auxetic Mechanical Metamaterials. Materials. 2019;12(4):635.
15. Kolken HMA, Janbaz S, Leeflang SMA, Lietaert K, Weinans HH, Zadpoor AA. Rationally designed meta-implants: a combination of auxetic and conventional meta-biomaterials. Materials Horizons. 2018;5(1):28-35.
16. Williams JL, Lewis JL. Properties and an anisotropic model of cancellous bone from the proximal tibial epiphysis. J Biomech Eng. 1982;104(1):50-6.
17. Choi HJ, Lee JJ, Park YJ, Shin JW, Sung HJ, Shin JW, et al. MG-63 osteoblast-like cell proliferation on auxetic PLGA scaffold with mechanical stimulation for bone tissue regeneration. Biomater Res. 2016;20:33.
18. Zhang W, Soman P, Meggs K, Qu X, Chen S. Tuning the Poisson's Ratio of Biomaterials for Investigating Cellular Response. Advanced Functional Materials. 2013;23(25):3226-32.
19. Karageorgiou V, Kaplan D. Porosity of 3D biomaterial scaffolds and osteogenesis. Biomaterials. 2005;26(27):5474-91.
20. Prot M, Saletti D, Pattofatto S, Bousson V, Laporte S. Links between mechanical behavior of cancellous bone and its microstructural properties under dynamic loading. Journal of Biomechanics. 2015;48(3):498-503.
21. Holtorf HL, Datta N, Jansen JA, Mikos AG. Scaffold mesh size affects the osteoblastic differentiation of seeded marrow stromal cells cultured in a flow perfusion bioreactor. Journal of Biomedical Materials Research Part A. 2005;74A(2):171-80.
22. Frost HM. A 2003 Update of Bone Physiology and Wolff's Law for Clinicians. The Angle Orthodontist. 2004;74(1):3-15.

23. Gibson LJ. The mechanical behaviour of cancellous bone. Journal of Biomechanics. 1985;18(5):317-28.
24. Majumdar S, Kothari M, Augat P, Newitt DC, Link TM, Lin JC, et al. High-Resolution Magnetic Resonance Imaging: Three-Dimensional Trabecular Bone Architecture and Biomechanical Properties. 1998;22(5):445-54.
25. Morgan EF, Bayraktar HH, Yeh OC, Majumdar S, Burghardt A, Keaveny TM. Contribution of inter-site variations in architecture to trabecular bone apparent yield strains. Journal of Biomechanics. 2004;37(9):1413-20.
26. Hildebrand T, Rüegsegger P. A new method for the model-independent assessment of thickness in three-dimensional images. Journal of Microscopy. 1997;185(1):67-75.
27. Rabiatul AAR, Fatihhi SJ, Harun MN, Kadir MRA, Ardiyansyah S. A Narrative Review of Morphology of Cancellous Bone at Different Human Anatomy - Methods and Parameters. Applied Mechanics and Materials. 2014;695:567-71.
28. Rho JY, Hobatho MC, Ashman RB. Relations of mechanical properties to density and CT numbers in human bone. Medical Engineering & Physics. 1995;17(5):347-55.
29. Fazzalari NL, Forwood MR, Smith K, Manthey BA, Herreen P. Assessment of Cancellous Bone Quality in Severe Osteoarthrosis: Bone Mineral Density, Mechanics, and Microdamage. Bone. 1998;22(4):381-8.
30. Wu D, Isaksson P, Ferguson SJ, Persson C. Young's modulus of trabecular bone at the tissue level: A review. Acta Biomaterialia. 2018;78:1-12.
31. Zhang X-Y, Fang G, Zhou J. Additively Manufactured Scaffolds for Bone Tissue Engineering and the Prediction of their Mechanical Behavior: A Review. Materials. 2017;10(1):50.
32. Rho JY, Ashman RB, Turner CH. Young's modulus of trabecular and cortical bone material: ultrasonic and microtensile measurements. J Biomech. 1993;26(2):111-9.
33. Boal DH, Seifert U, Shillcock JC. Negative Poisson ratio in two-dimensional networks under tension. Physical Review E. 1993;48(6):4274-83.
34. Kowalczyk P. Elastic properties of cancellous bone derived from finite element models of parameterized microstructure cells. 2003;36(7):961-72.
35. Müller R, Rüegsegger P. Three-dimensional finite element modelling of non-invasively assessed trabecular bone structures. 1995;17(2):126-33.
36. Pothuaud L, Van Rietbergen B, Mosekilde L, Beuf O, Levitz P, Benhamou CL, et al. Combination of topological parameters and bone volume fraction better predicts the mechanical properties of trabecular bone. 2002;35(8):1091-9.
37. Rho J-Y, Tsui TY, Pharr GM. Elastic properties of human cortical and trabecular lamellar bone measured by nanoindentation. 1997;18(20):1325-30.
38. Mandal BB, Kundu SC. Cell proliferation and migration in silk fibroin 3D scaffolds. Biomaterials. 2009;30(15):2956-65.
39. Gibson LJ, Ashby MF, Schajer GS, Robertson CI. The Mechanics of Two-Dimensional Cellular Materials. Proceedings of the Royal Society A: Mathematical, Physical and Engineering Sciences. 1982;382(1782):25-42.
40. Babaee S, Jahromi BH, Ajdari A, Nayeb-Hashemi H, Vaziri A. Mechanical properties of open-cell rhombic dodecahedron cellular structures. Acta Materialia. 2012;60(6-7):2873-85.
41. Kolken HMA, Zadpoor AA. Auxetic mechanical metamaterials. RSC Advances. 2017;7(9):5111-29.
42. Jiang Y, Rudra B, Shim J, Li Y. Limiting strain for auxeticity under large compressive Deformation: Chiral vs. re-entrant cellular solids. International Journal of Solids and Structures. 2019;162:87-95.
43. Wang MO, Vorwald CE, Dreher ML, Mott EJ, Cheng MH, Cinar A, et al. Evaluating 3D-printed biomaterials as scaffolds for vascularized bone tissue engineering. Adv Mater. 2015;27(1):138-44.
44. Hou X, Silberschmidt V. Metamaterials with Negative Poisson's Ratio: A Review of Mechanical Properties and Deformation Mechanisms. 2015. p. 155-79.
45. Wang K, Chang Y-H, Chen Y, Zhang C, Wang B. Designable dual-material auxetic metamaterials using three-dimensional printing. Materials & Design. 2015;67:159-64.

46. Liu Y, Campbell J, Stein O, Jiang L, Hund J, Lu Y. Deformation Behavior of Foam Laser Targets Fabricated by Two-Photon Polymerization. Nanomaterials. 2018;8(7):498.

47. Pittsburgh Uo. Nanoscribe Photonic Professional (GT). University of Pittsburgh; 2018.

48. Pisarenko AV, Zvagelsky RD, Kolymagin DA, Katanchiev BV, Vitukhnovsky AG, Chubich DA. DLW-printed optical fiber micro-connector kit for effective light coupling in optical prototyping. Optik. 2020;201:163350.

49. Nouri-Goushki M, Mirzaali MJ, Angeloni L, Fan D, Minneboo M, Ghatkesar MK, et al. 3D Printing of Large Areas of Highly Ordered Submicron Patterns for Modulating Cell Behavior. ACS Applied Materials & Interfaces. 2019.

50. Nouri-Goushki M, Sharma A, Sasso L, Zhang S, Van Der Eerden BCJ, Staufer U, et al. Submicron Patterns-on-a-Chip: Fabrication of a Microfluidic Device Incorporating 3D Printed Surface Ornaments. ACS Biomaterials Science & Engineering. 2019.

51. Arnaud L, Gourlay E. Experimental study of parameters influencing mechanical properties of hemp concretes. 2012;28(1):50-6.

52. ISO. 13314:2011 Mechanical Testing of Metals-Ductility Testing-Compression Test for Porous and Cellular Metals. 2011.

53. Moser B, Wasmer K, Barbieri L, Michler J. Strength and fracture of Si micropillars: A new scanning electron microscopy-based micro-compression test. Journal of Materials Research. 2007;22(4):1004-11.

54. Linde F, Norgaard P, Hvid I, Odgaard A, Soballe K. Mechanical properties of trabecular bone. Dependency on strain rate. J Biomech. 1991;24(9):803-9.

55. Keaveny TM, Wachtel EF, Ford CM, Hayes WC. Differences between the tensile and compressive strengths of bovine tibial trabecular bone depend on modulus. 1994;27(9):1137-46.

56. Sasaki N, Odajima S. Stress-strain curve and young's modulus of a collagen molecule as determined by the X-ray diffraction technique. Journal of Biomechanics. 1996;29(5):655-8.

57. Caddock B. Negative Poisson ratios and strain-dependent mechanical properties in arterial prostheses. Biomaterials. 1995;16(14):1109-15.

58. Pendegrass CJ, Middleton CA, Blunn GW. Fibronectin Functionalized Hydroxyapatite Coatings: Improving Dermal Fibroblast Adhesion In Vitro and In Vivo. Advanced Engineering Materials. 2010;12(8):B365-B73.

59. Van Hengel IAJ, Gelderman FSA, Athanasiadis S, Minneboo M, Weinans H, Fluit AC, et al. Functionality-packed additively manufactured porous titanium implants. Materials Today Bio. 2020;7:100060.

60. Shu R, McMullen R, Baumann MJ, McCabe LR. Hydroxyapatite accelerates differentiation and suppresses growth of MC3T3-E1 osteoblasts. Journal of Biomedical Materials Research. 2003;67A(4):1196-204.

61. Sonnaert M, Papantoniou I, Luyten FP, Schrooten J. Quantitative Validation of the Presto Blue™ Metabolic Assay for Online Monitoring of Cell Proliferation in a 3D Perfusion Bioreactor System. 2015;21(6):519-29.

62. Bensimon-Brito A, Cardeira J, Dionísio G, Huysseune A, Cancela ML, Witten PE. Revisiting in vivo staining with alizarin red S - a valuable approach to analyse zebrafish skeletal mineralization during development and regeneration. BMC Developmental Biology. 2016;16(1).

63. zur Nieden NI, Kempka G, Ahr HJ. In vitro differentiation of embryonic stem cells into mineralized osteoblasts. Differentiation. 2003;71(1):18-27.

64. Hadjicharalambous C, Kozlova D, Sokolova V, Epple M, Chatzinikolaidou M. Calcium phosphate nanoparticles carrying BMP-7 plasmid DNA induce an osteogenic response in MC3T3-E1 pre-osteoblasts. Journal of Biomedical Materials Research Part A. 2015;103(12):3834-42.

65. Liu Z, Yao X, Yan G, Xu Y, Yan J, Zou W, et al. Mediator MED23 cooperates with RUNX2 to drive osteoblast differentiation and bone development. Nature Communications. 2016;7(1):11149.

66. Barak LS, Yocum RR, Nothnagel EA, Webb WW. Fluorescence staining of the actin cytoskeleton in living cells with 7-nitrobenz-2-oxa-1,3-diazole-phallacidin. Proceedings of the National Academy of Sciences. 1980;77(2):980-4.

67. Akech J, Wixted JJ, Bedard K, Van Der Deen M, Hussain S, Guise TA, et al. Runx2 association with progression of prostate cancer in patients: mechanisms mediating bone osteolysis and osteoblastic metastatic lesions. Oncogene. 2010;29(6):811-21.
68. Blanca M, Alarcón R, Arnau J, Bono R, Bendayan R. Non-normal data: Is ANOVA still a valid option? Psicothema. 2017;29:552-7.
69. Statistics L. Multiple regression analysis using statistics: Leard Statistics; 2018 [
70. Hindié M, Degat M-C, Gaudière F, Gallet O, Van Tassel PR, Pauthe E. Pre-osteoblasts on poly(l-lactic acid) and silicon oxide: Influence of fibronectin and albumin adsorption. Acta Biomaterialia. 2011;7(1):387-94.
71. Faghihi S, Azari F, Zhilyaev AP, Szpunar JA, Vali H, Tabrizian M. Cellular and molecular interactions between MC3T3-E1 pre-osteoblasts and nanostructured titanium produced by high-pressure torsion. Biomaterials. 2007;28(27):3887-95.
72. Chen X, Fu X, Shi J-g, Wang H. Regulation of the osteogenesis of pre-osteoblasts by spatial arrangement of electrospun nanofibers in two- and three-dimensional environments. Nanomedicine: Nanotechnology, Biology and Medicine. 2013;9(8):1283-92.
73. Liu J-L, Feng X-Q, Wang G-F. Buoyant force and sinking conditions of a hydrophobic thin rod floating on water. Physical Review E. 2007;76(6):066103.
74. Treesinchai S, Puttipipatkhachorn S, Pitaksuteepong T, Sungthongjeen S. Development of curcumin floating tablets based on low density foam powder. Asian Journal of Pharmaceutical Sciences. 2016;11(1):130-1.
75. Biowest. Safety data sheet. 2006.
76. 3rd DPG, Samsel RW, Solway J. Effect of surface tension and viscosity on airway reopening. Journal of applied Physiology. 1990;69(1):74-85.
77. Streubel A, Siepmann J, Bodmeier R. Floating microparticles based on low density foam powder. International Journal of Pharmaceutics. 2002;241(2):279-92.
78. Kim MJ, Choi HJ, Cho J, Lee JB, Sung H-J, Kim JK. MG-63 Cell Proliferation with Static or Dynamic Compressive Stimulation on an Auxetic PLGA Scaffold. 2017;2017:1-6.
79. Maharjan B, Park J, Kaliannagounder VK, Awasthi GP, Joshi MK, Park CH, et al. Regenerated cellulose nanofiber reinforced chitosan hydrogel scaffolds for bone tissue engineering. Carbohydrate Polymers. 2021;251:117023.
80. Uchida R, Bhawal UK, Kiba H, Arai K, Tanimoto Y, Kuboyama N, et al. Effect of plasma-irradiated silk fibroin in bone regeneration. Journal of Bioscience and Bioengineering. 2014;118(3):333-40.
81. Kim HJ, Kim U-J, Vunjak-Novakovic G, Min B-H, Kaplan DL. Influence of macroporous protein scaffolds on bone tissue engineering from bone marrow stem cells. Biomaterials. 2005;26(21):4442-52.
82. Mygind T, Stiehler M, Baatrup A, Li H, Zou X, Flyvbjerg A, et al. Mesenchymal stem cell ingrowth and differentiation on coralline hydroxyapatite scaffolds. Biomaterials. 2007;28(6):1036-47.
83. Wang Y, Shi X, Ren L, Wang C, Wang D-A. Porous poly (lactic-co-glycolide) microsphere sintered scaffolds for tissue repair applications. Materials Science and Engineering: C. 2009;29(8):2502-7.
84. Zeng S, Liu L, Shi Y, Qiu J, Fang W, Rong M, et al. Characterization of Silk Fibroin/Chitosan 3D Porous Scaffold and In Vitro Cytology. 2015;10(6):e0128658.
85. Balasubramanian MK, Helfman DM, Hemmingsen SM. A new tropomyosin essential for cytokinesis in the fission yeast S. pombe. Nature. 1992;360(6399):84-7.
86. Silva M, Shepherd EF, Jackson WO, Dorey FJ, Schmalzried TP. Average patient walking activity approaches 2 million cycles per year: pedometers under-record walking activity. J Arthroplasty. 2002;17(6):693-7.

7. Appendix

7.1 VHX-6000 – Bone-mimicking scaffolds
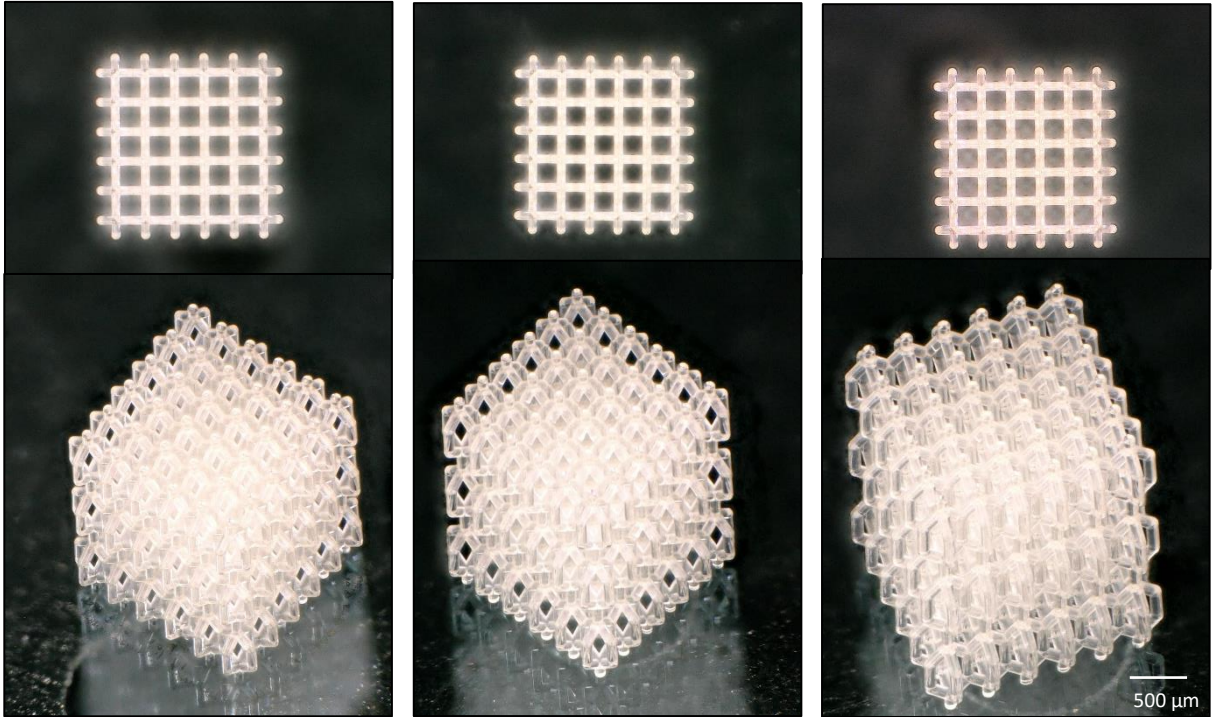
Figure 32. Manufactured C_p.
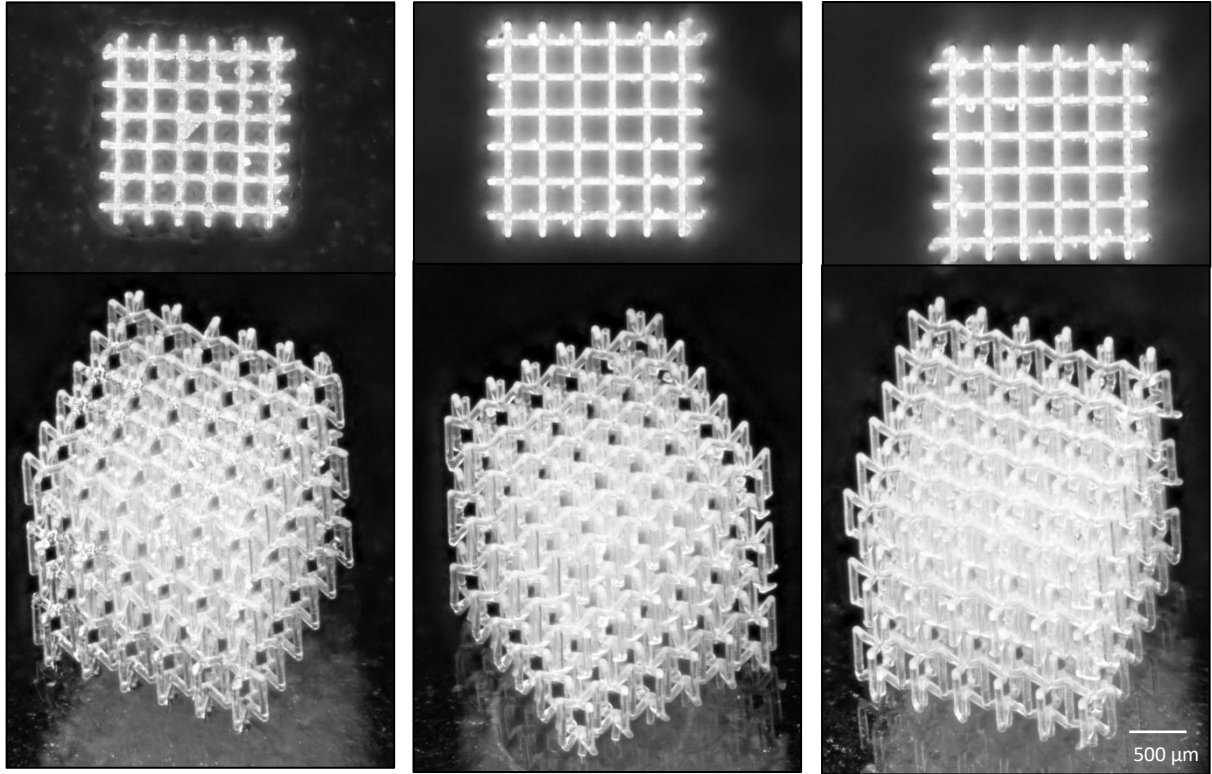
Figure 33. Manufactured A_p.
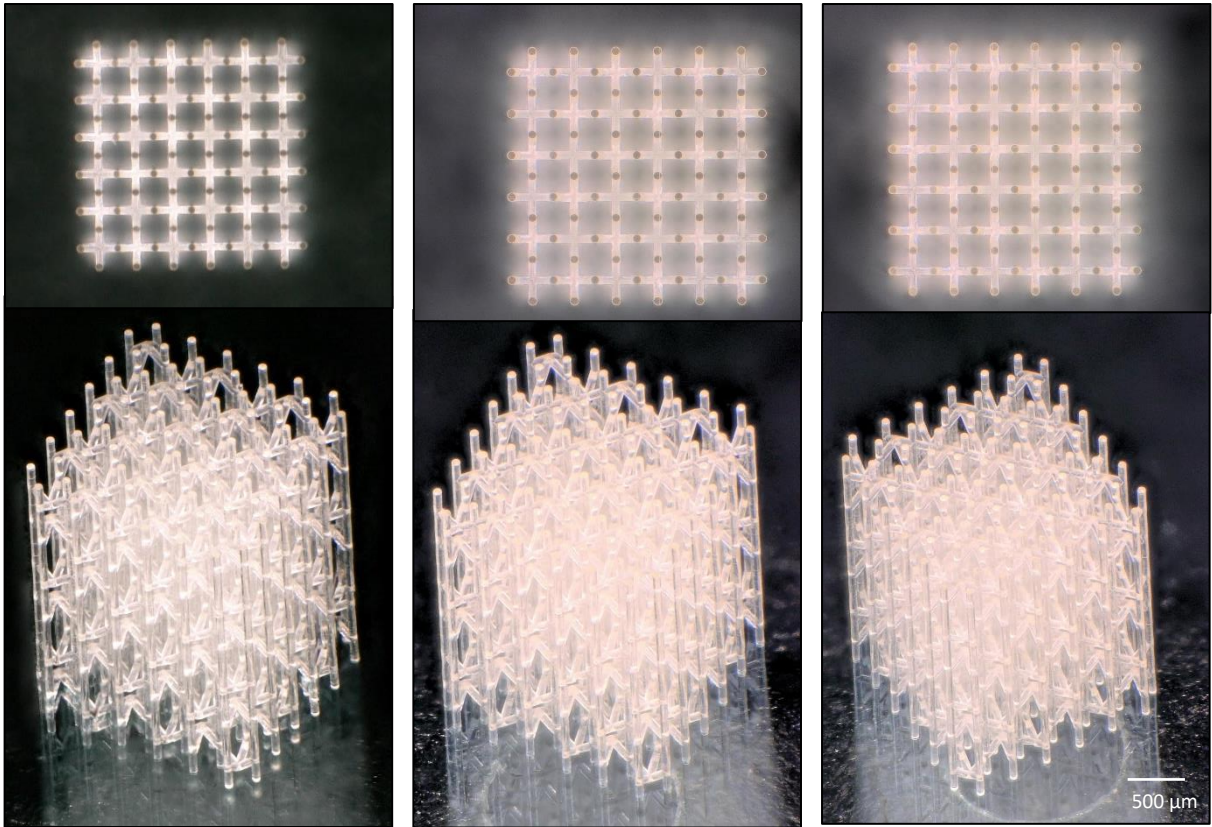
Figure 34. Manufactured H_p.

7.2 Structures after mechanical testing
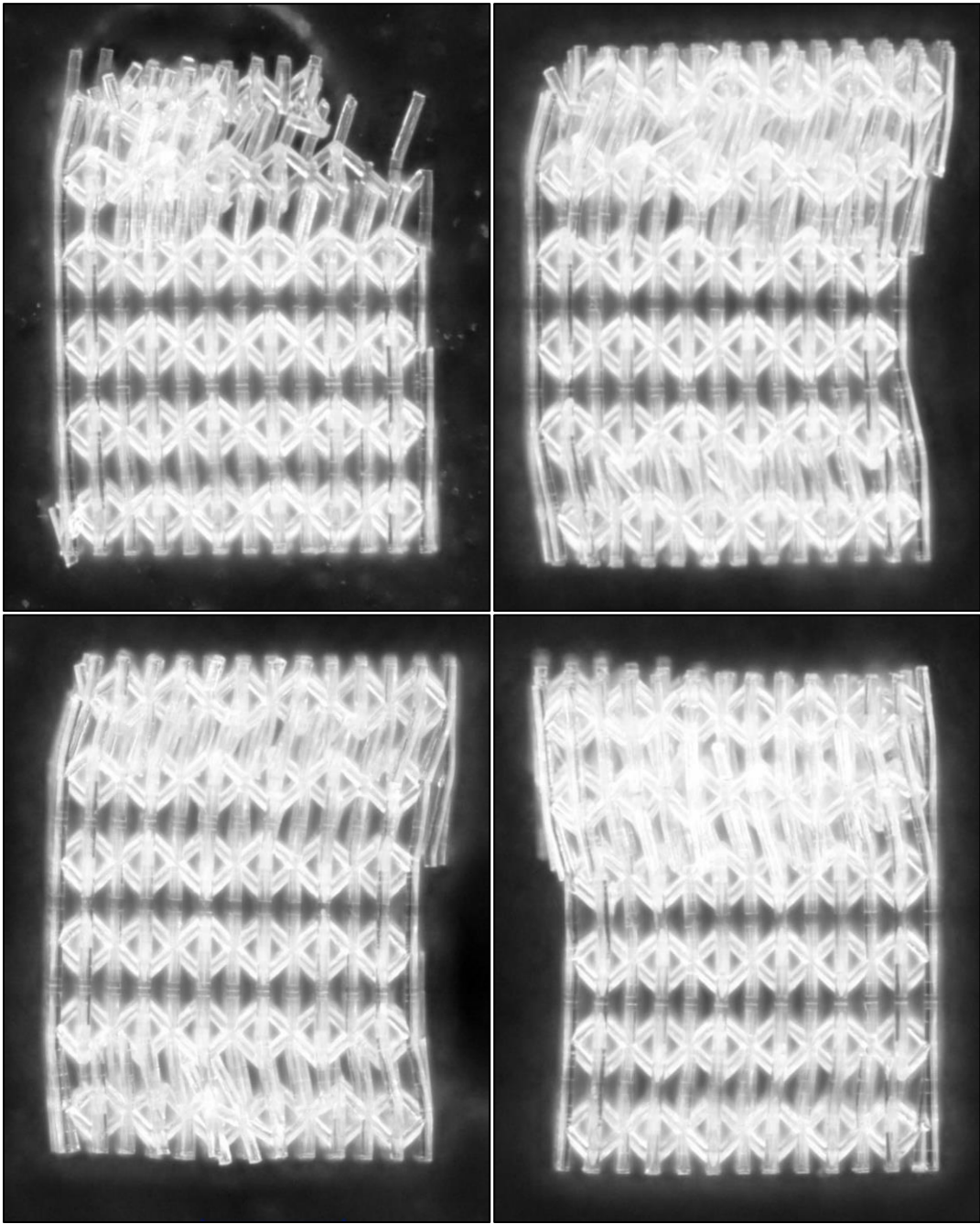
Figure 35. Hybrid bone-mimicking scaffolds after mechanical compression.

7.3 Actin staining vs SEM images bone-mimicking scaffolds
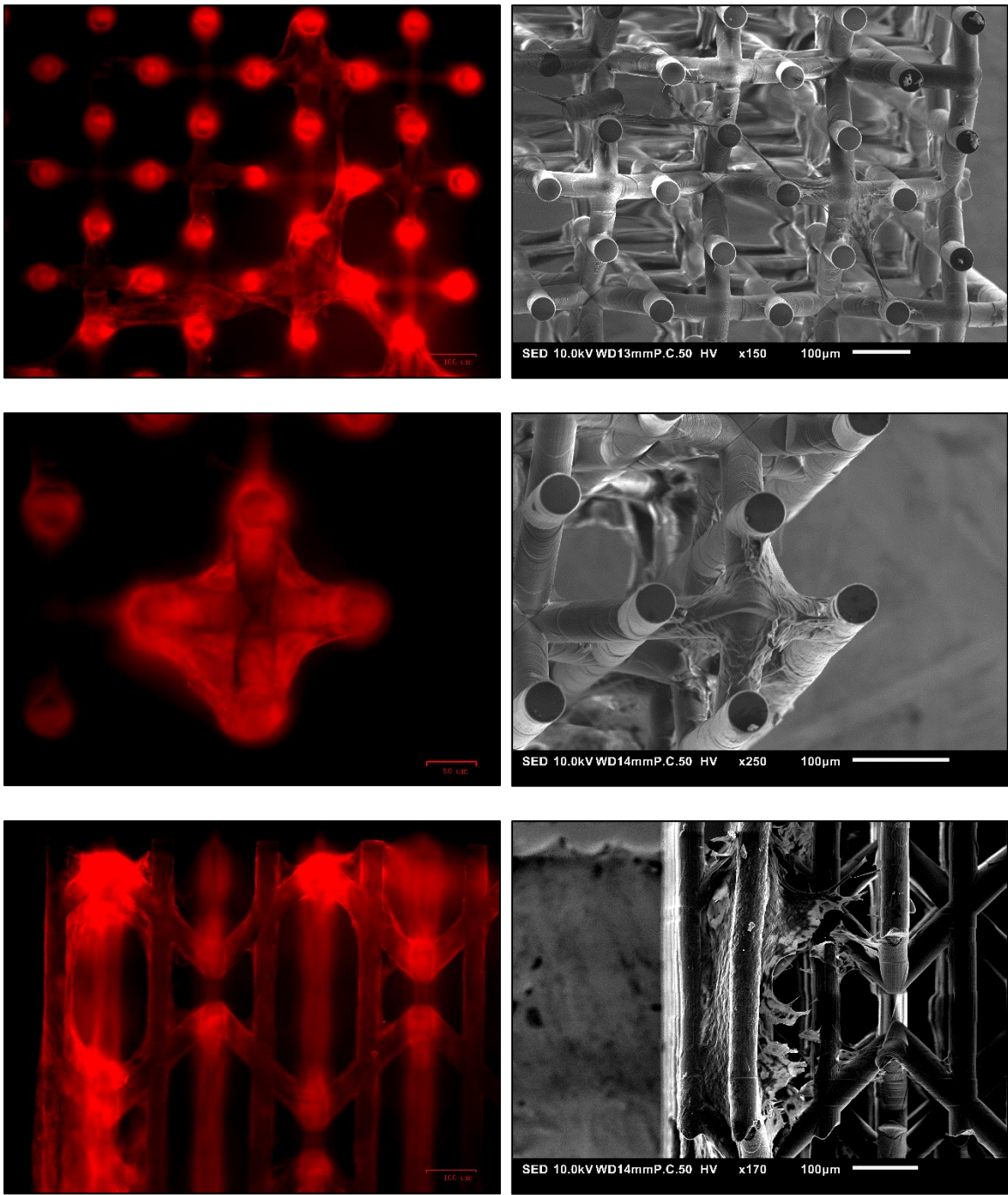
Figure 36. Images on the left show the results of the actin staining and the results on the right show the corresponding SEM images.

7.4 SEM - Bone-mimicking scaffolds
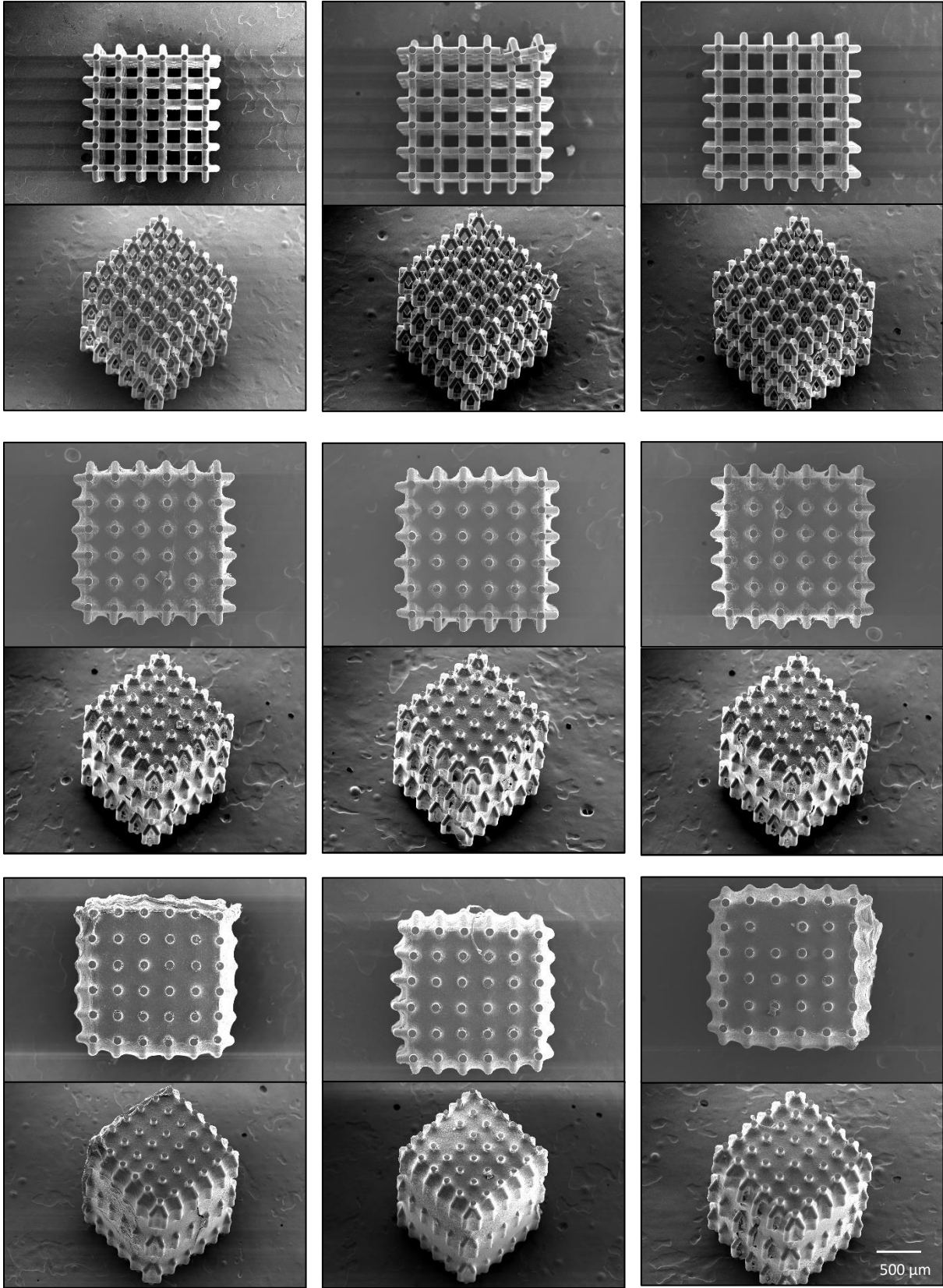
Figure 37. C_P after 3, 14 and 21 days of cell culture.
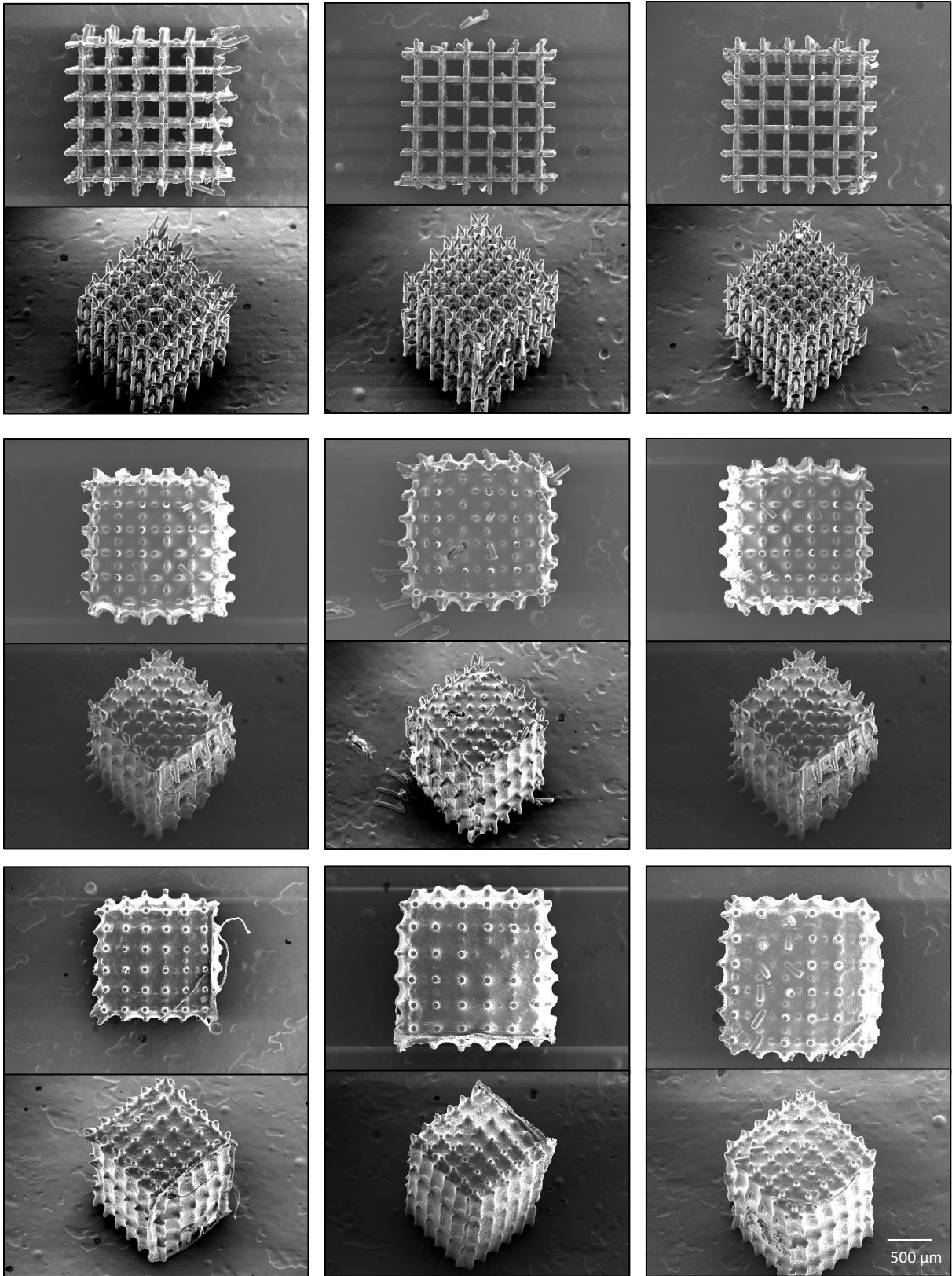
Figure 38. A_p after 3, 14 and 21 days of cell culture.
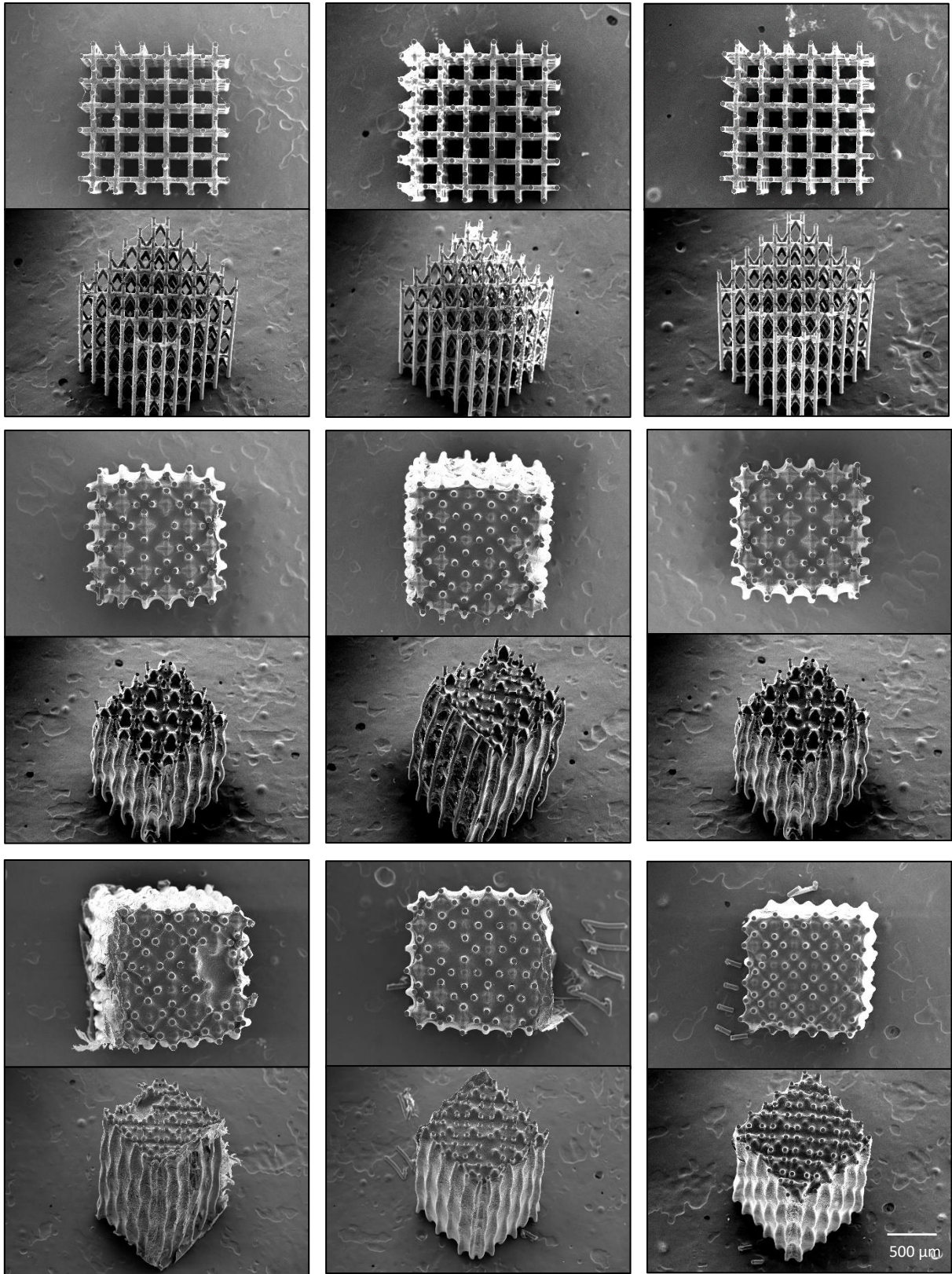
Figure 39. H$_p$ after 3, 14 and 21 days of cell culture.

7.5 Reliability presto blue

The data of day 11 only consisted out of data obtained at one point in time and could, therefore, not be checked on its reliability. The data of the control group could not be tested with the statistical analysis because the sample sizes of 2 were too small. The data of the C_p on days 3, 7 and 14, A_p on days 1, 3 and 7 and H_p on days 1, 3, and 14 are normally distributed, as assessed by the Shapiro-Wilk's test (p > 0.05), whereas the data of the C_p on days 1, A_p at day 14 and H_p on day 7 are non-normally distributed (p < 0.05). The assumption of homogeneity of variance was met for C_p on days 1, 3, 7, and 14, A_p on days 1, 3, 7, and 14 and H_p on days 1, 3, and 14, as assessed by Levene's test (p > 0.05), whereas the data of the H_p on day 7 showed heterogeneity of variance (p < 0.05). The data of H_p on day 7 did not meet the requirements of a normal distribution nor homogeneity of variance and did not have equal sample sizes or the ratio of the largest group variance to the smallest group variance is higher than 3, and therefore the non-parametric Mann-Whitney test was performed. For the rest of the data, the independent t-test was performed. All results are presented in table 11 and show that there is no significant difference found, therefore, the results of the presto blue staining at different time points are combined including the results of day 11 and the control group.

Table 11. Results of reliability analysis of presto blue results.

Day	C_p		A_p		H_p	
1	t(6) = 0.419, p > 0.05		t(6) = 0.585, p > 0.05		t(6) = 0.764, p > 0.05	
3	t(5) = 0.246, p > 0.05		t(6) = 0.435, p > 0.05		t(6) = 0.134, p > 0.05	
7	t(5) = 0.101, p > 0.05		t(6) = 1.633, p > 0.05		U = 10, p > 0.05	
14	t(6) = 2.501, p > 0.05		t(5) = 0.090, p > 0.05		t(6) = 1.965, p > 0.05	

7.6 Statistical analysis presto blue

The data of days 3 and 11 are normally distributed, as assessed by the Shapiro-Wilk's test (p > 0.05), whereas the data of days 1, 7 and 14 are non-normally distributed (p < 0.05). The assumption of homogeneity of variance was met on days 1, 7, 11 and 14, as assessed by Levene's test (p > 0.05), whereas the data of day 3 showed heterogeneity of variance (p < 0.05). Days 1, 3, 7 and 14 did not meet the requirements of a normal distribution nor homogeneity of variance and did not have equal sample sizes or the ratio of the largest group variance to the smallest group variance is higher than 3, and therefore the non-parametric Kruskal-Wallis test was performed.

The data of day 11 showed, with a one-way ANOVA including Bonferroni correction, that the control group was significantly different from C_p, A_p and H_p ($F_{(3,10)} = 56.473$, $p < 0.05$, $n = 4$). The mean and standard deviation of statistical analysis of presto blue staining are shown in table 12.

The data of days 1, 3, 7 and 14 showed that there were significant differences ($H_{(3)} = 22.034$, $p < 0.05$; $H_{(3)} = 16.677$, $p < 0.05$; $H_{(3)} = 12.666$, $p < 0.05$; $H_{(3)} = 15.241$, $p < 0.05$, respectively). To obtain where these differences are, the Mann-Whitney test with Bonferroni correction was performed. It showed that the control group was always significantly different from C_p, A_p and H_p. The test also showed that, on days 1 and 3 C_p was significantly different from A_p and, on day 14, A_p was significantly different from H_p.

Table 12. Results of statistical analysis from presto blue; mean and standard deviation.

Bone-mimicking scaffold		Day 1	Day 3	Day 7	Day 11	Day 14
Control group		857 ± 169	1957 ± 1284	3334 ± 126	2747 ± 310	3250 ± 386
C_p		3038 ± 155	3252 ± 71	4452 ± 566	4290 ± 76	4564 ± 155
A_p		3598 ± 165	4275 ± 435	5007 ± 232	4414 ± 159	4652 ± 102
H_p		3258 ± 167	3741 ± 509	4968 ± 395	4272 ± 148	4445 ± 124

7.7 ARS staining
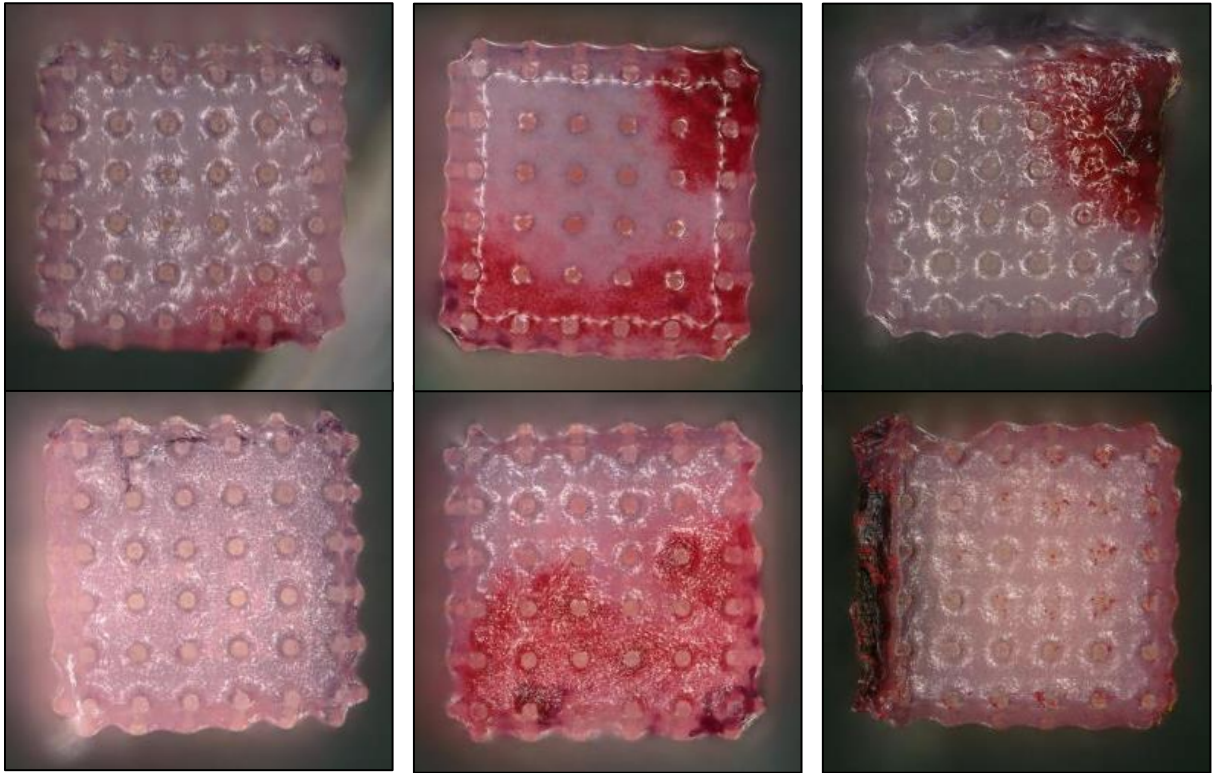
Figure 40. Alizarin Red S staining of C_p top and bottom.
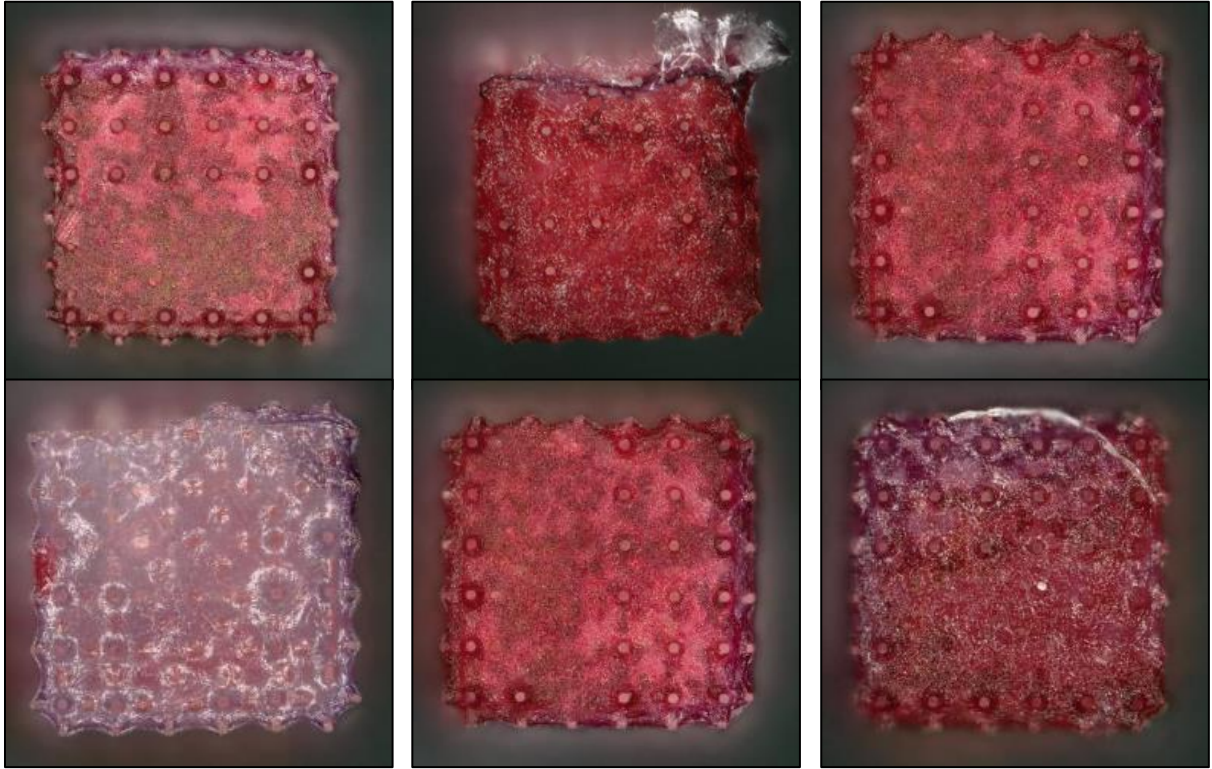
Figure 41. Alizarin Red S staining of A_p top and bottom.
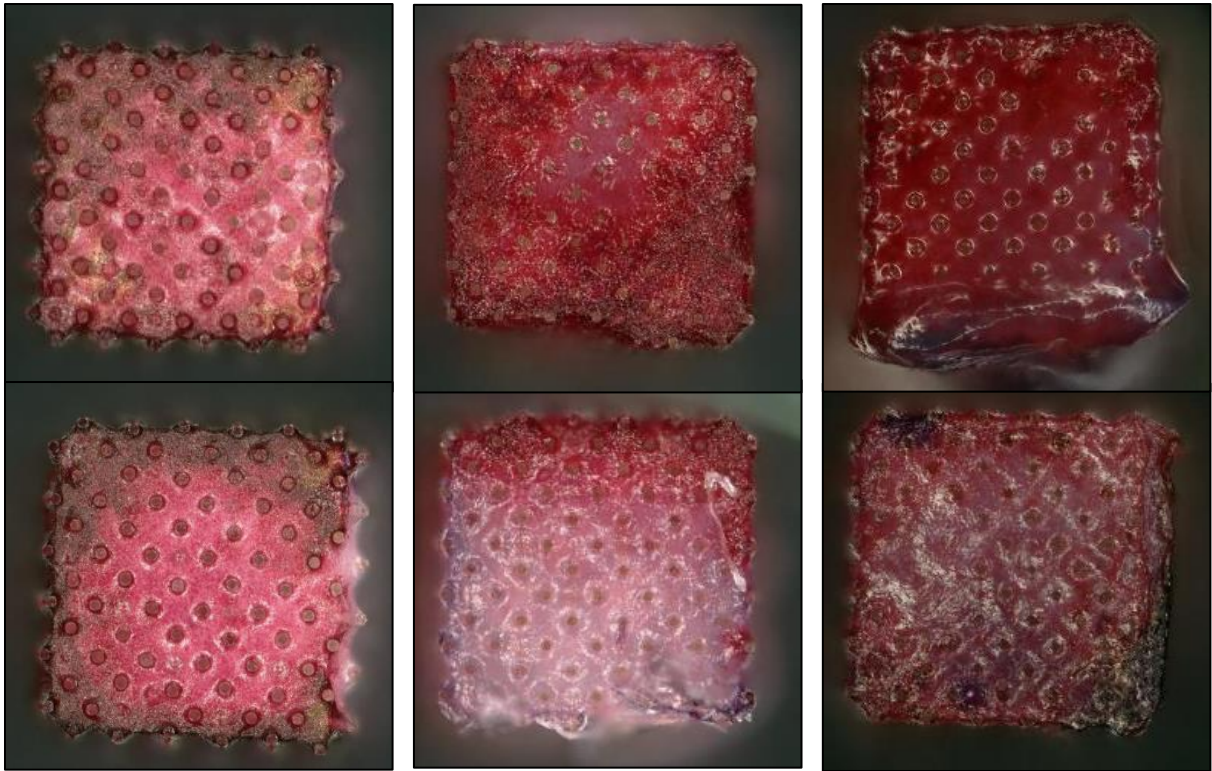
Figure 42. Alizarin Red S staining of H_p top and bottom.

7.8 Reliability ARS staining

The data of C_p, A_p and H_p are normally distributed, as assessed by the Shapiro-Wilk's test ($p > 0.05$) and the assumption of homogeneity of variance was met for C_p, A_p and H_p as assessed by Levene's test ($p > 0.05$). Therefore, the independent t-test was performed from which the results are presented in table 13. A significant difference was found between the results of A_p at different time points, whereas the results of C_p and H_p showed no significant differences between different time points. The experiments of meta-biomaterials C_p, A_p and H_p were performed exactly the same way, therefore, it was chosen to combine all results of the ARS staining at different time points.

Table 13. Results of reliability analysis of ARS staining results.

C_p		A_p		H_p	
t(6) = 0.401, p > 0.05		t(6) = -3.965, p < 0.05		t(6) = 0.147, p > 0.05	

7.9 Statistical analysis ARS staining

The data showed a normal distribution, as assessed by the Shapiro-Wilk's test, and Levene's test showed heterogeneity of variance. Even though the sample sizes were equal, the Kruskal-Wallis test was performed because the ratio of the largest group variance to the smallest group variance was higher than 3.

The data showed that there are significant differences ($H(2) = 10.960$, $p < 0.05$, $n = 3$), and therefore the Mann-Whitney test with Bonferroni correction was performed. This test showed that C_p (M = 690, SD = 122) was significantly different from A_p (M = 1289, SD = 423) and H_p (M = 1250, SD = 395).

7.10 VHX-6000 - Micro-scale scaffolds
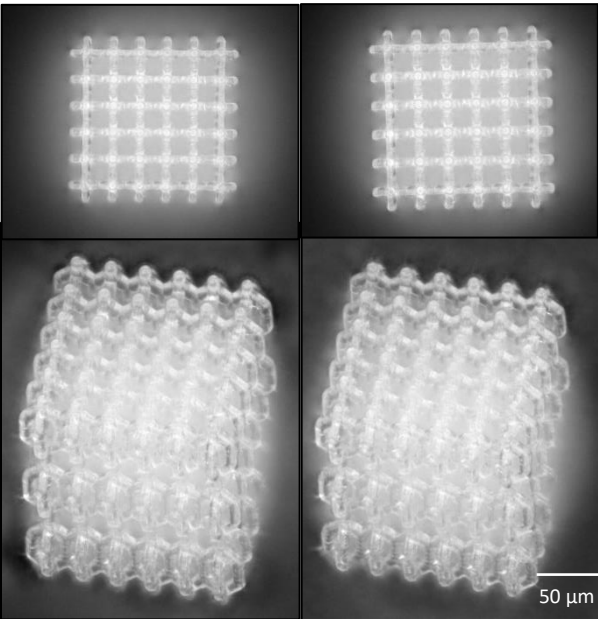
Figure 43. Manufactured C_p.
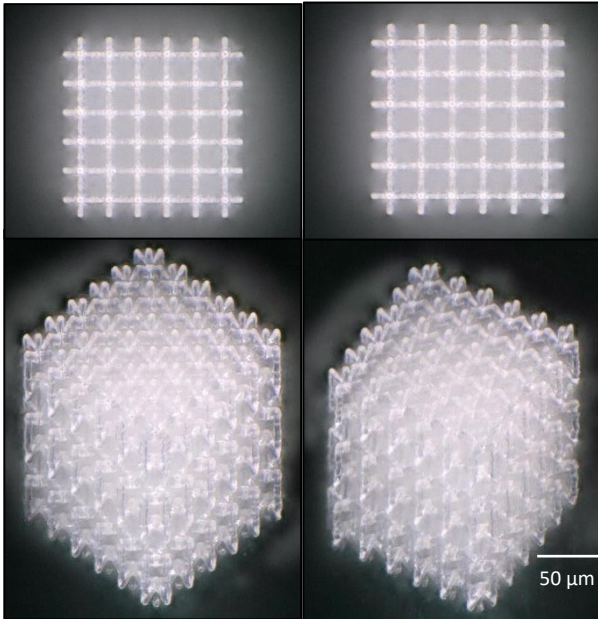
Figure 44. Manufactured A_p.
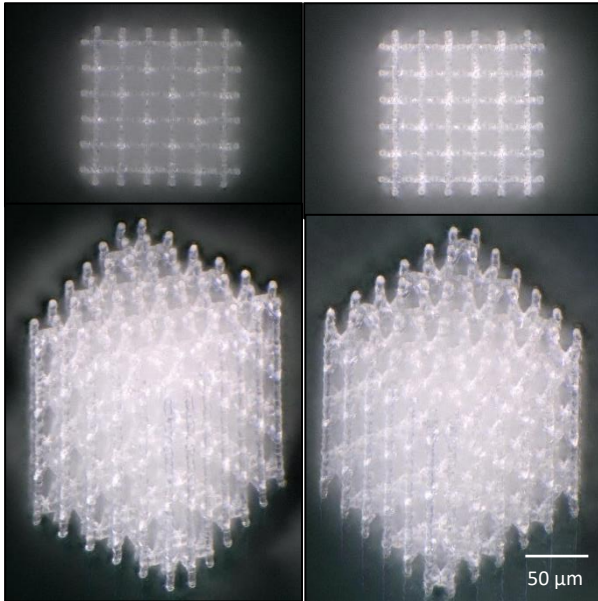
Figure 45. Manufactured H_p/H_s.
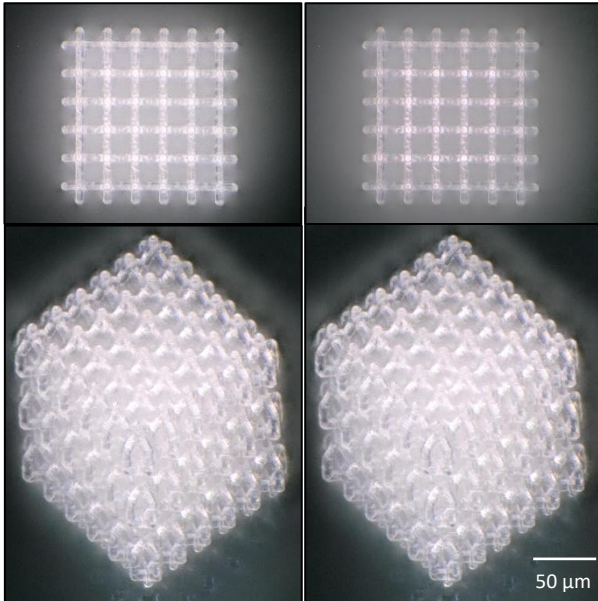
Figure 46. Manufactured C_s.
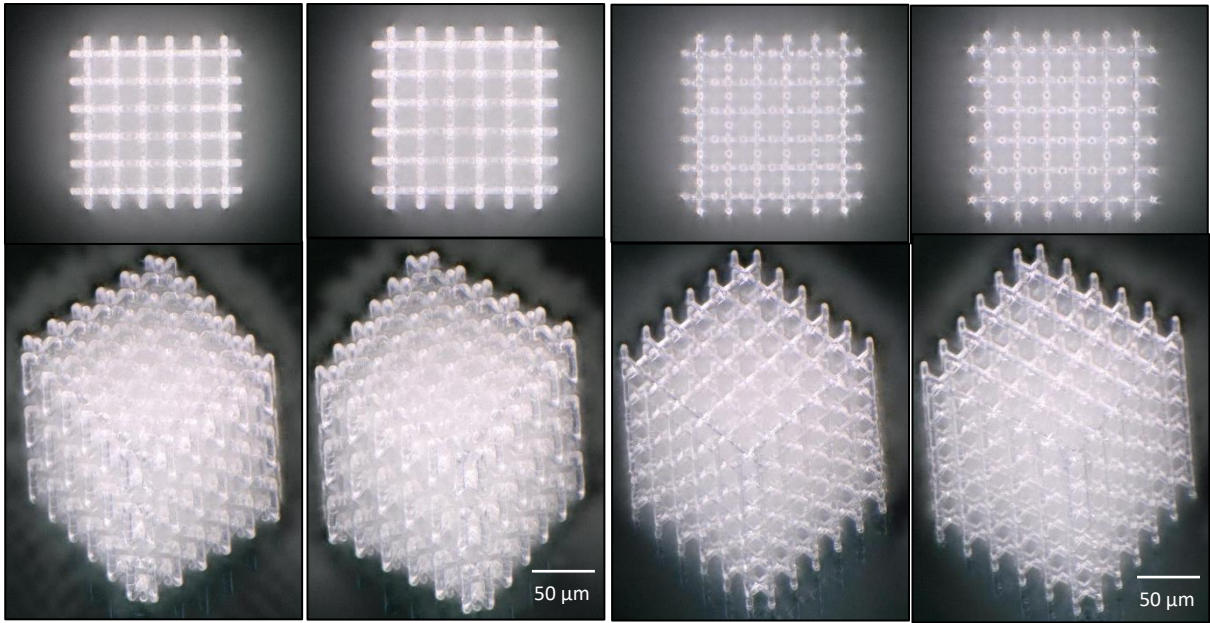
Figure 47. Manufactured A_s.

Figure 48. Manufactured CB_s.

7.11 SEM - Micro-scale scaffolds
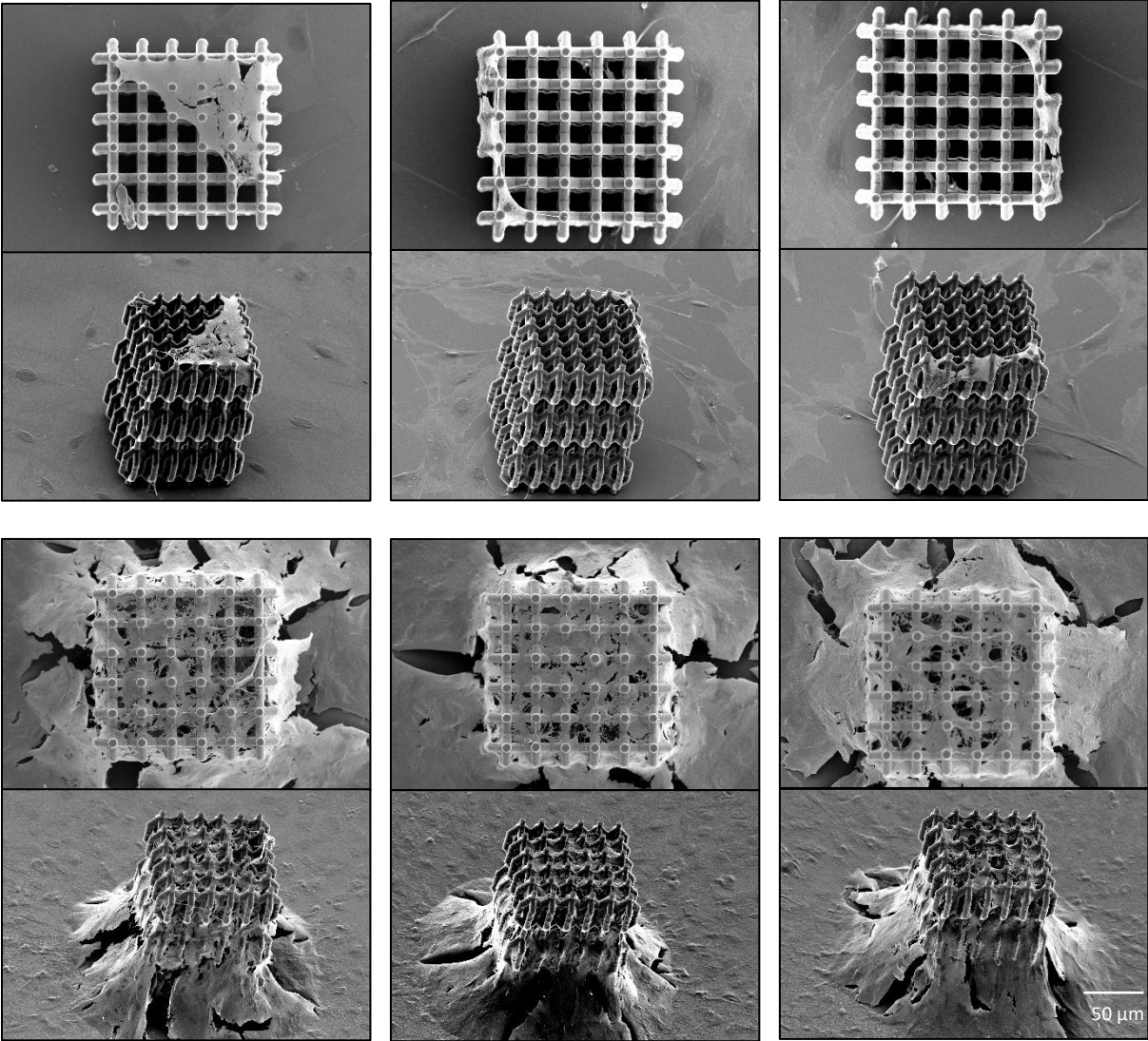
Figure 49. C_p after 3 and 7 days of cell culture.
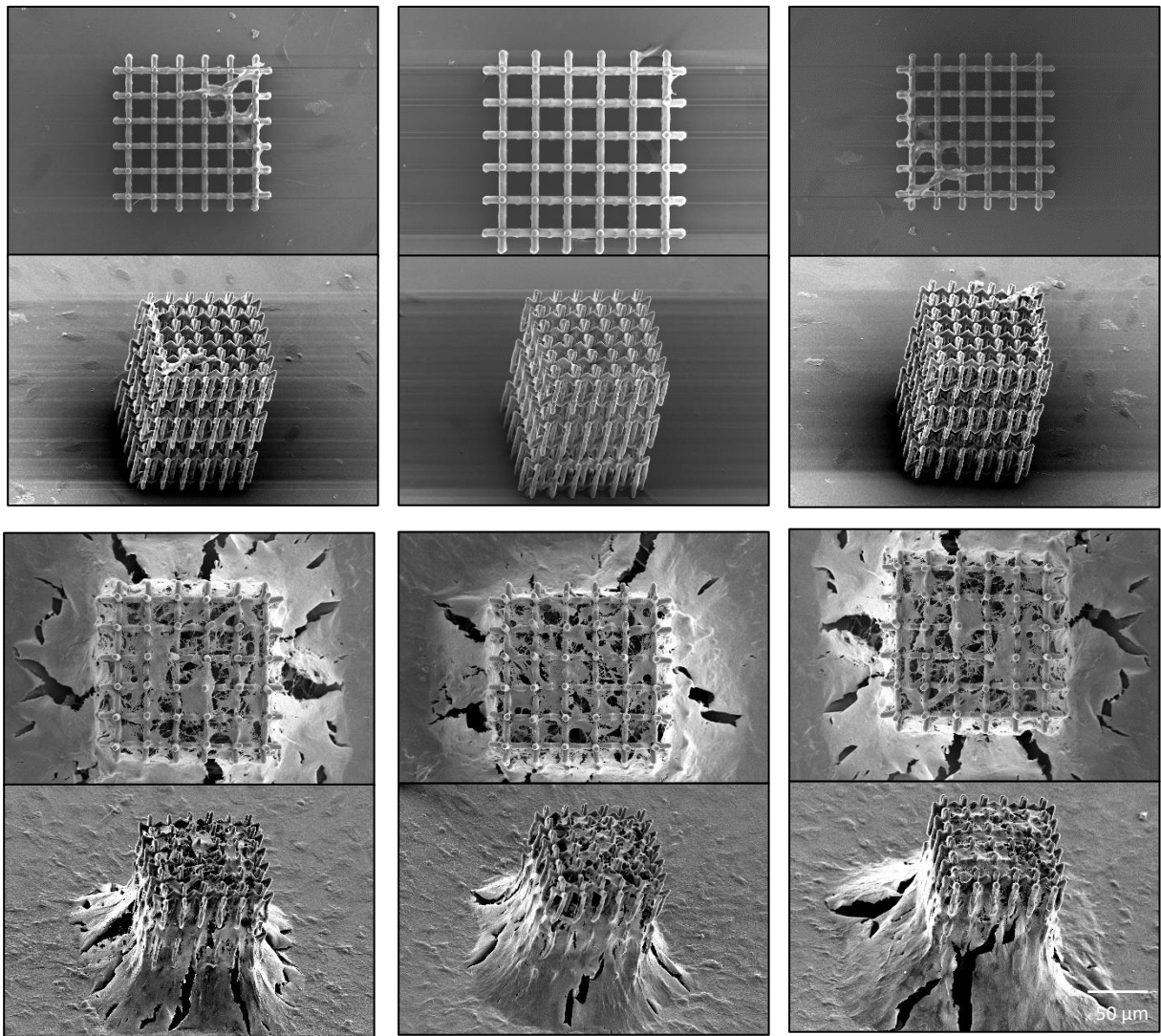
Figure 50. A$_p$ after 3 and 7 days of cell culture.
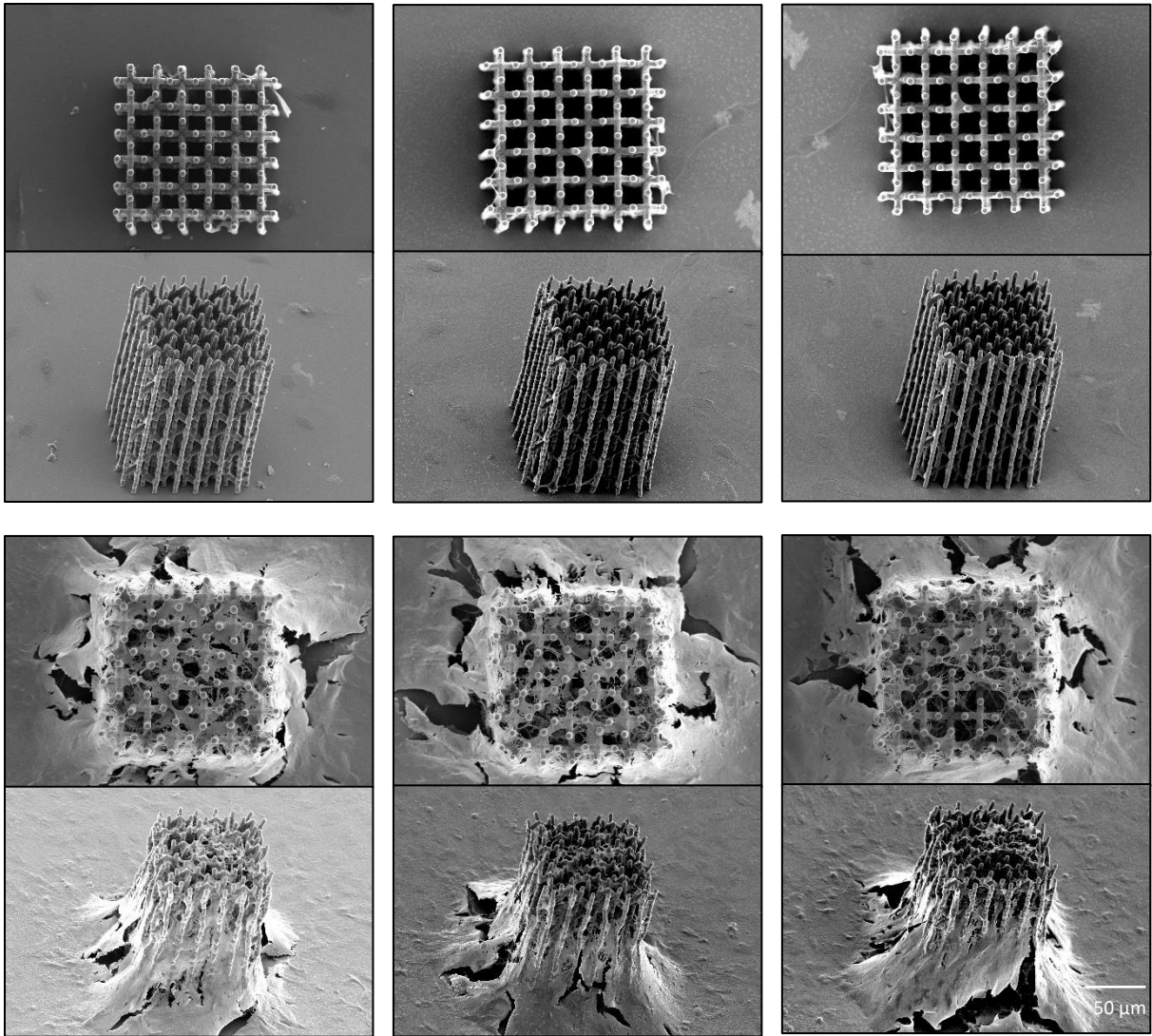
Figure 51. H_p/H_s after 3 and 7 days of cell culture.
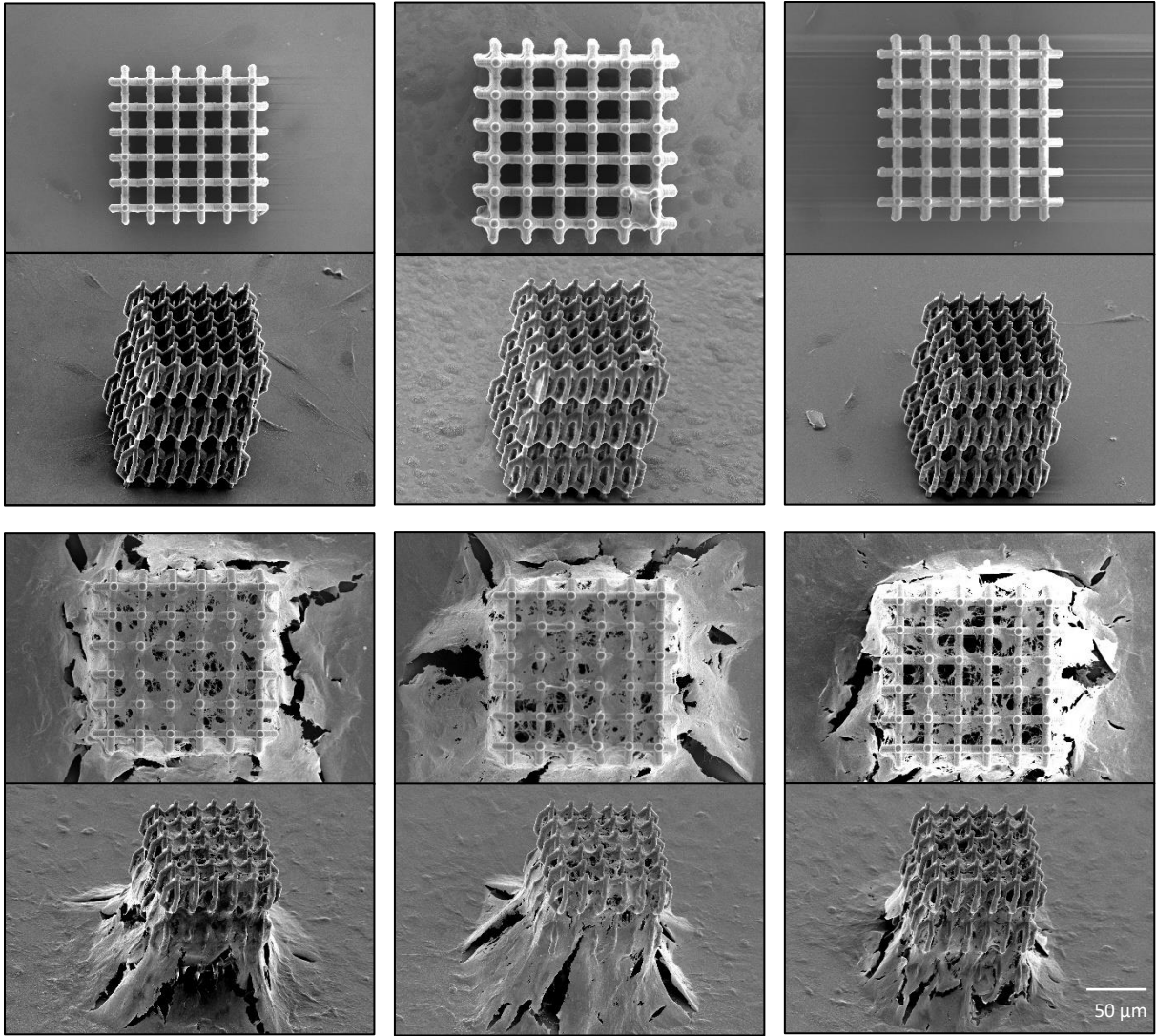
Figure 52. C$_S$ after 3 and 7 days of cell culture.
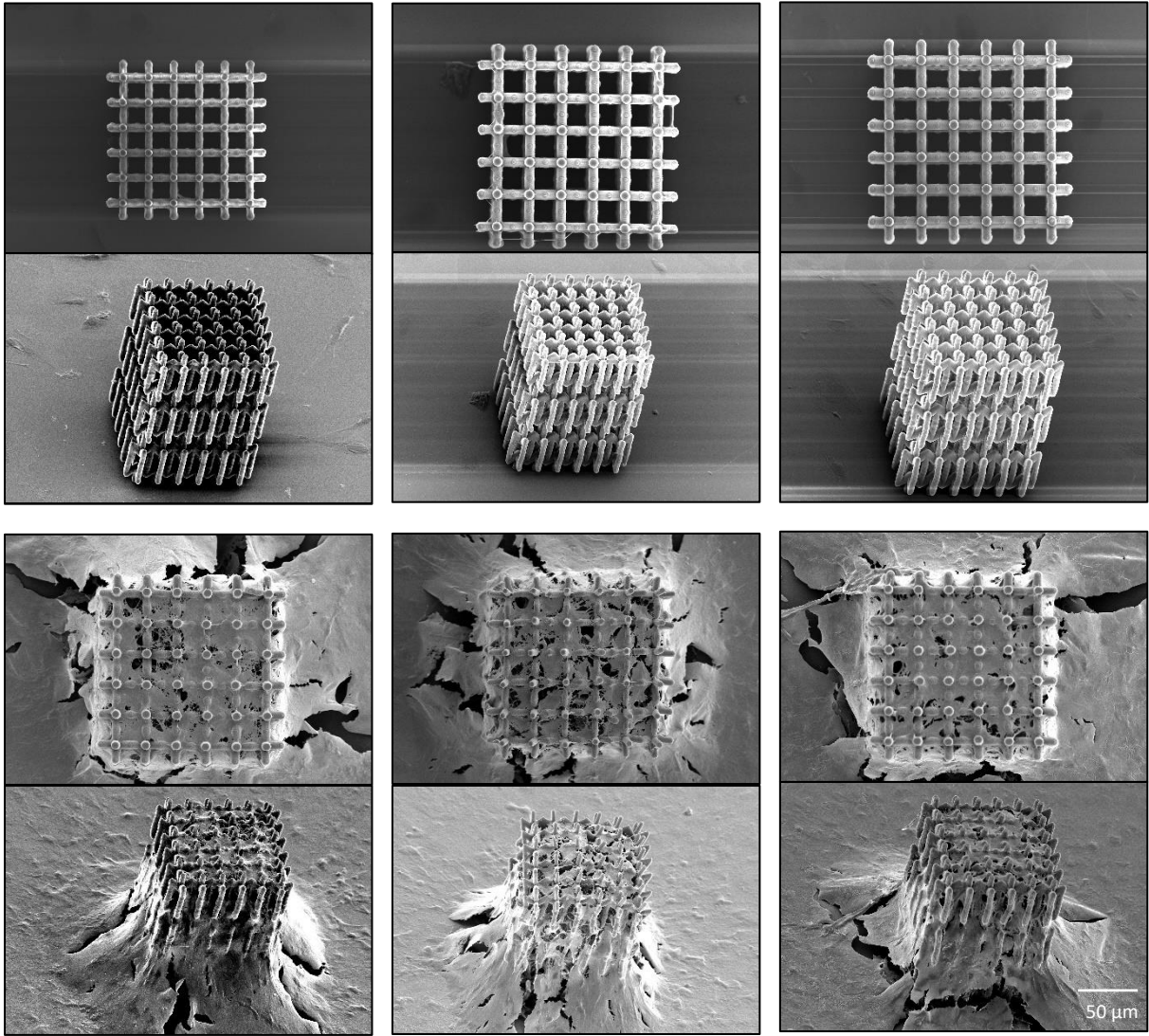
Figure 53. A_S after 3 and 7 days of cell culture.
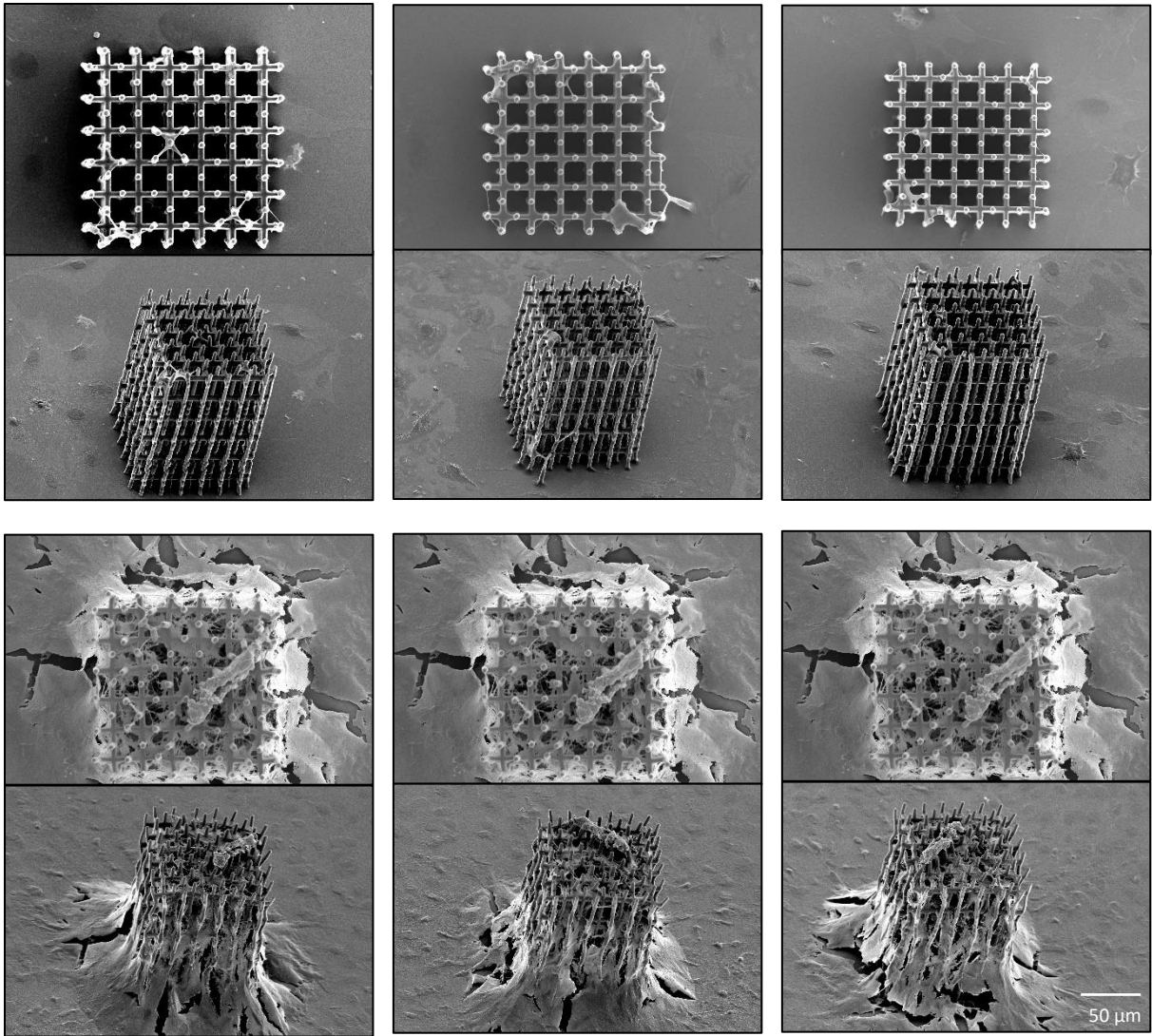
Figure 54. CB$_s$ after 3 and 7 days of cell culture.

7.12 Actin staining
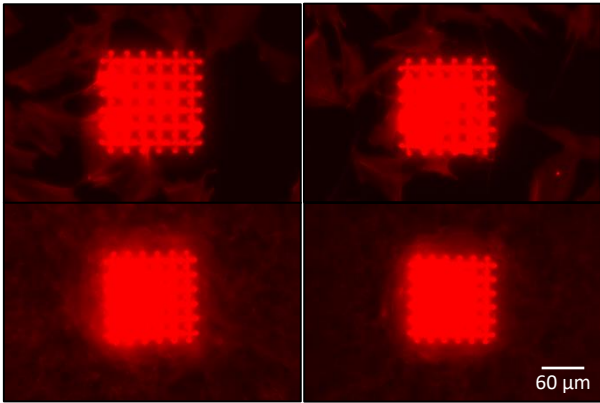
Figure 55. Actin staining of C_p after 3 and 7 days.
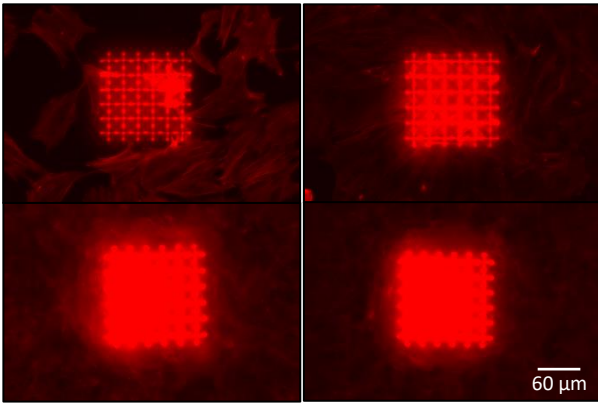
Figure 56. Actin staining of A_p after 3 and 7 days.
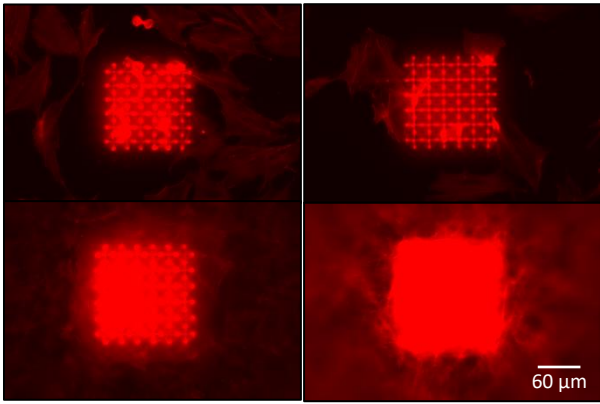
Figure 57. Actin staining of H_p/H_s after 3 and 7 days.
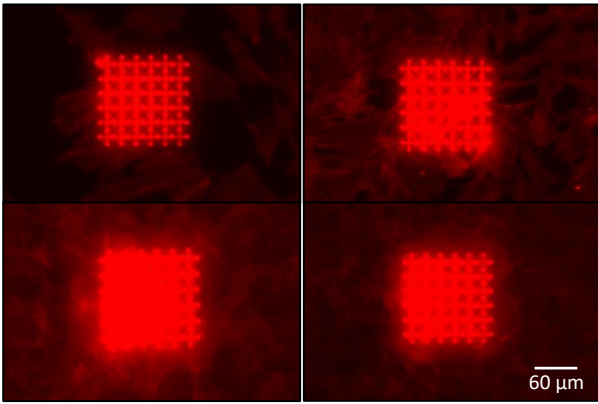
Figure 58. Actin staining of C_s after 3 and 7 days.
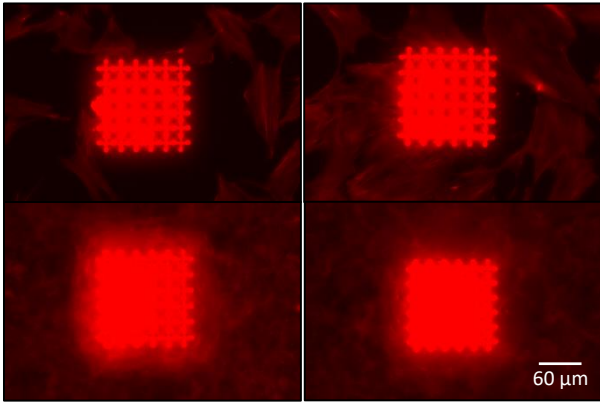
Figure 59. Actin staining of A_s after 3 and 7 days.
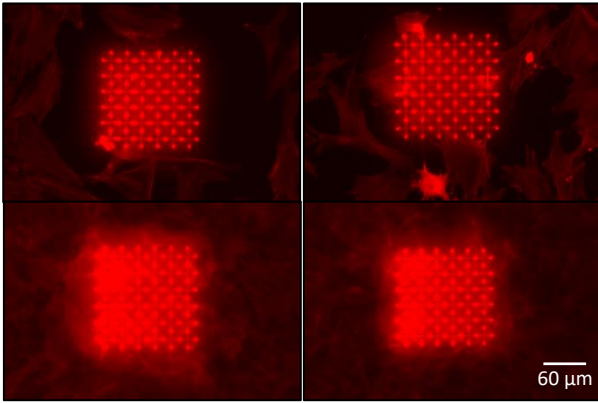
Figure 60. Actin staining of CB_s after 3 and 7 days.

7.13 Reliability actin staining

Most of the data at different points in time had a sample size of two, therefore, this data could not be checked on their normal distribution and homogeneity of variance. The data that had a sample size of three or four, was tested to have a normal distribution, as assessed by the Shapiro-Wilk's test ($p > 0.05$) and homogeneity of variance, as assessed by Levene's test ($p > 0.05$). The one-way ANOVA test was performed and the results are presented in table 14 and show that significant differences are found between the results at different time points. However, this included two of the specimens at each evaluation day, and the experiment of each specimen was performed exactly the same way, so we decided to label the results of the actin staining reliable and combine the results of the different time points.

Table 14. Results of reliability analysis of actin staining results after 3 days.

C_p		A_p		H_p/H_s		C_s		A_s		CB_s	
$F_{(2,7)} = 4.026$, $p > 0.05$		$F_{(2,3)} = 4.886$, $p > 0.05$		$F_{(2,3)} = 1.975$, $p > 0.05$		$F_{(2,4)} = 1.819$, $p > 0.05$		$F_{(2,4)} = 15.496$, $p < 0.05$		$F_{(2,6)} = 23.147$, $p < 0.05$	

7.14 Statistical analysis actin staining

The data showed a normal distribution, as assessed by the Shapiro-Wilk's test, and Levene's test showed homogeneity of variance. A one-way ANOVA test and a regression analysis were performed.

The one-way ANOVA test showed that there are significant differences ($F_{(5,39)}$ = 22.975, $p < 0.05$), therefore the Bonferroni post hoc test was performed. This test showed that, for the micro-p-scale scaffolds, C_p was significantly different from A_p and H_p and that A_p was significantly different from H_p (mean and standard deviation of statistical analysis of actin staining after 3 days are shown in table 15). The test also showed that, for the micro-s-scale scaffolds, C_s was significantly different from H_s and CB_s and that A_s was significantly different from H_s and CB_s.

Table 15. Results of statistical analysis from actin staining on day 3.

Micro-scale scaffold		Mean (M)	Standard deviation (SD)	# specimen (n)
C_p		$1.54 * 10^{14}$	$7.43 * 10^{12}$	10
A_p		$2.11 * 10^{14}$	$2.43 * 10^{13}$	6
H_p/ H_s		$1.94 * 10^{14}$	$2.64 * 10^{13}$	6
C_s		$1.65 * 10^{14}$	$9.45 * 10^{12}$	7
A_s		$1.52 * 10^{14}$	$9.54 * 10^{13}$	7
CB_s		$2.15 * 10^{14}$	$1.86 * 10^{13}$	9

A multiple regression analysis was performed for day 3, to identify how much of the variance in grey value can be explained by the variance in Poisson's ratio, Young's modulus and porosity. The linear regression explains 40.2% of the variance in the data ($F_{(3,41)}$ = 9.184, $p < 0.05$, R^2 = 0.402), and shows that this was a good estimation ($p < 0.05$). All three variables significantly contributed to the prediction. The Poisson's ratio appears to have the highest impact, followed by the porosity and the Young's modulus (beta = 0.422, beta = 0.420, and beta = -0.396, respectively).

7.15 Runx2 staining
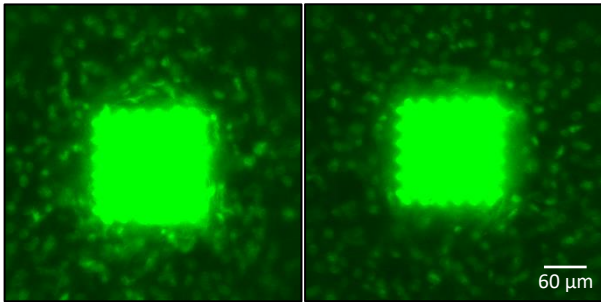
Figure 61. Runx2 staining of C_p.
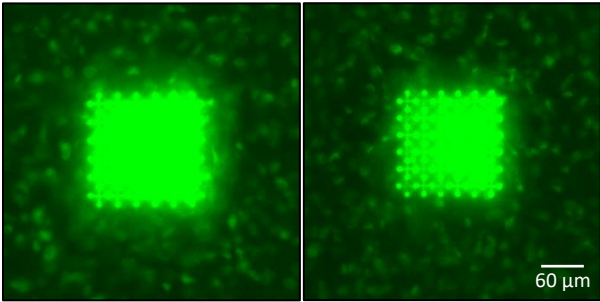
Figure 62. Runx2 staining of A_p.
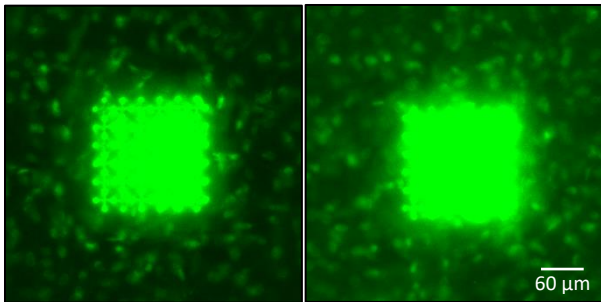
Figure 63. Runx2 staining of H_p/H_s.
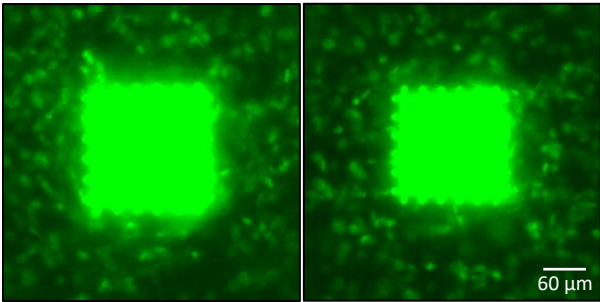
Figure 64. Runx2 staining of C_s.
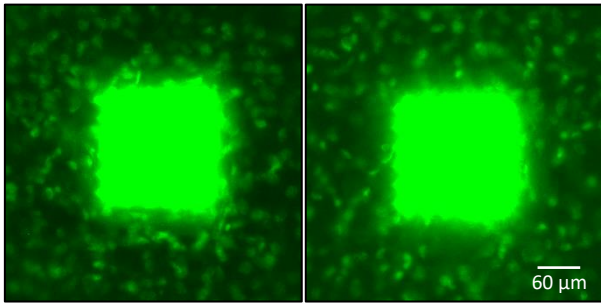
Figure 65. Runx2 staining of A_s.
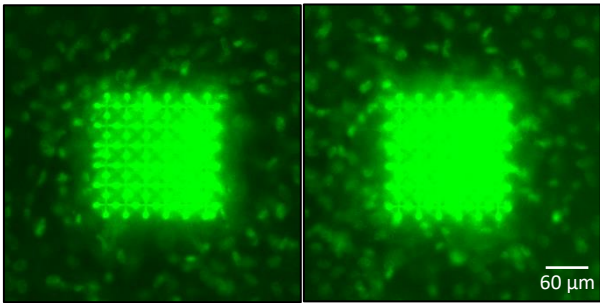
Figure 66. Runx2 staining of CB_s.